Investigating the effects of applying a high voltage DC electric field in a flame using a point to plane electrode arrangement

Matthew S. F. Li

University College London

A Thesis submitted for the degree of Doctor of Philosophy

January 2014

I, Matthew S. F. Li confirm that the work presented in this thesis is my own. Where information has been derived from other sources, I confirm that this has been indicated in the thesis.

Abstract

A high voltage DC electric field was applied to methane and hydrogen flames using electrodes in a point to plane configuration. In a methane flame the Townsend mechanisms were observed along with the streamer, glow and spark corona discharge and were characterised using electrical, visual, audio and mass spectrometry data. A Pt point electrode was used to explore the region where the Townsend mechanisms took place by taking full mass spectrums from 10 – 50 amu for various voltages, varying oxygen concentration and using different inert gases. Large decreases in H_2O and CO_2 was observed in the ratio of 2:1 while an increase of N_2 and O_2 was also seen. These changes were attributed to transport effects moving the H_2O and CO_2 molecules away from the sample inlet. As the H_2O and CO_2 molecules were displaced, air was drawn in which caused the appearance of an increase in N_2 and O_2. One possible explanation for the transport effect is the electric field ionized O_2 while the positive electrode repelled the ions. It is this movement that then pushes the H_2O and CO_2 molecules away from the sample inlet. The effect of a spark corona discharge on SO_2 and CO_2 in a hydrogen flame was also explored. Both were observed to decrease upon the creation of the discharge. Again transport effects could be used to explain these findings. The thesis also documents the design and creation of an automated experimental system used to obtain the results. This included hardware design, controlling software and scripts to analyse the large volume of data. The platform enabled an experimenter to control the gas flow, electrode placement, voltage and current applied automatically, while taking synchronised voltage, current, audio, visual and mass spectrometry data.

Dedicated to my parents for giving me the opportunities of a lifetime.

Acknowledgements

Of the many lessons I learnt during my PhD learning when to ask for help was probably the most important. I ended up relying on more people than I could ever imagine and this work would not have been possible if countless people had not given up their time.

I have to first thank my supervisor Dr Daren Caruana for having invested so much in me. Having changed my view of things from day one, I wouldn't be the scientist I am today. From a theorist I became an experimentalist and all my experimental skills were taught by him. His optimism he showed me every day as we tackled the impossible was only overshadowed by the patience he had with me, which I am genuinely surprised has not run out. I was fortunate to have two more supervisors in the form of Prof Julian Evans and Prof Asterios Gavriilidis. Their fresh perceptive was vital and enlightening when I was down a dead end.

I would like to thank Dr Toks Fowowe, Dr Dimitris Sarantaridis, Dr Emina Hadzifejzovic, Dr Jason Butler, Atif Elahi and Maria Calleja the members of the gas phase electrochemistry group who I shared many happy memories and fruitful discussions. I would also like to thank Dr Katherine Holt and her entire electrochemistry group including Mohammed Haque and Meetal Hirani for teaching me about liquid phase electrochemistry and their projects.

The assistance I received from both the technical and admin staff of the chemistry department has been invaluable, especially when I needed something for the next day. I must thank Jim Stevenson in particular for his excellent workmanship in everything he made for me. As I made sure to always consult him for his input whenever I needed something made, most of the designs that were used was a team effort. I would also like to thank Dave Knapp, Joe Nolan and Dr Michael Parks who managed to help keep a vacuum system scavenged from the unknown working for over 5 years. My thanks also goes out the Dr Steve Firth for Raman advice, Len Parrish for electrical expertise and John Hill for mass spectrometry guidance.

I must also thank University College London. Although my research was in the chemistry department I went to numerous departments asking for help and received all I needed even though no one knew who I was, and all I had to show them was my ID. I never felt there was any department I could not approach.

I would like to thank the EPSRC, chemistry and chemical engineering department for funding this project and thus giving me this opportunity.

I have to also thank all the companies I've spoken too. The free samples that I asked for before my "bulk order" have always arrived faster than placing an order. In particular I must thank Hiden analytical for answering every question I have thrown at them.

I made many friends along this journey and even though I invoke a no science over coffee or lunch, without their emotional support this work would not have materialised.

Finally I would like to thank my family for supporting me without question on all my journeys that I have taken.

Table of contents

List of figures

List of tables

1 Introduction

1.1 Aim

This thesis documents the attempt to turn gaseous environmental pollutants produced by a flame into less harmful products. This was attempted by creating a plasma (an electrical discharge) and applying an electric field in the mentioned flame. While there are many techniques that can combat environmental pollutants such as catalytic convertors[1], there are two key differences that makes this work novel. The first is that the process used is an active one. This means the reaction can be driven (by electricity), as oppose to changing the surroundings to optimize the reaction. The second is that this solution aims to tackle the pollutants directly during their creation (in the flame). To date all established technologies to make combustion more clean can be broken down to three categories.

1) Pre-treat the reactants such as removing sulphur and nitrogen from the mix.
2) Changing combustion parameters such as gas ratios so they burn cleaner.
3) Clean up the harmful products downstream.

By placing electrodes in the flame we explore a fourth way which is to tackle the problem at the source. It is hoped that this offers a new angle of attack into combatting today's global warming problem.

1.2 Physical processes in plasmas

Plasmas are often referred to as the fourth state of matter and are the most energetic state. They are created when the electrons in a gas are stripped from their atoms to leave a mixture of positive ions and electrons. This mixture is electrically conducting but remains on average electrically neutral. Plasmas can take various forms and many are naturally occurring. The Aurora Borealis[2], solar winds[3] and lightning[4] are all examples of plasmas found in nature. Man-made plasmas are also made frequently and range from small sparks[5], flames[6], fluorescent light bulbs and in fusion containment

vessels[7]. Their applications include facilitating chemical reactions[8] that can't normally take place and surface modification[9].

With such a wide range of different forms, plasmas are typically characterised by their electron temperature and density (Figure 1-1). Plasmas can further be classified as "hot" or "cold" whereby in hot plasmas, the temperature of the electrons is equal to the temperature of the ions. This is opposed to cold plasmas were the electron temperature is typically magnitudes larger than the ion temperature. The work in this thesis makes use of flames which are hot plasmas and corona discharges which are cold.

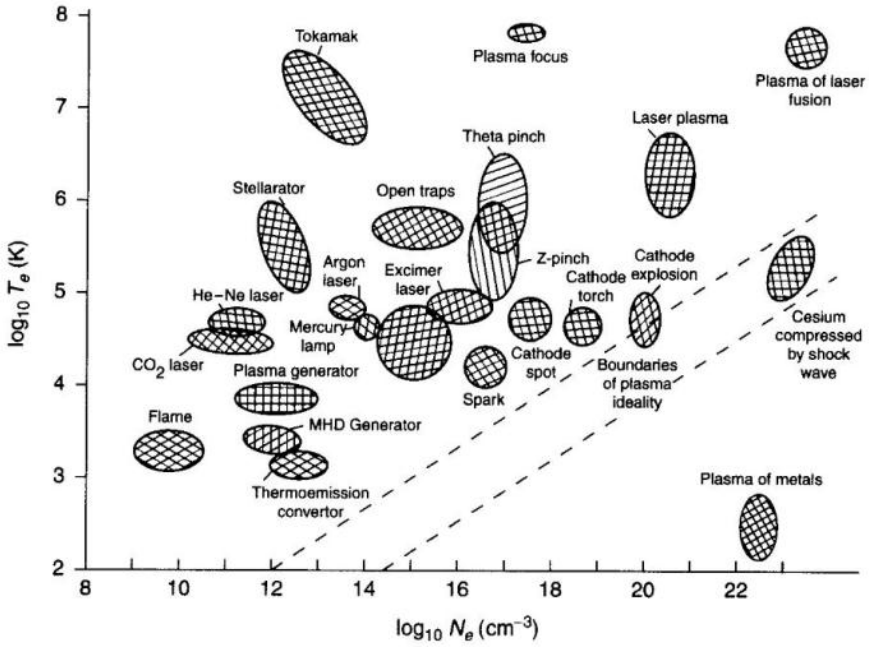

Figure 1-1: Graph showing different plasmas and their electron temperature and density[10].

As a plasma is a mixture of freely moving positive ions and electrons, the processes that are involved can largely be categorised into three areas: creation of the positive ions and electrons; their interaction with each other; and their movement. The process of their creation is treated in section 1.3 for direct current discharges and section 1.5.1 for flames.

An important parameter needed to understand plasma processes is the collision cross section. It is a value that expresses how likely a collision is going to occur. It takes into account both the probability a reaction will occur due to movement and size, and is

scaled relative to how many collisions it takes for a reaction to happen. Positive ions and electrons interaction can be understood by collisions, while their movements are governed by their mobility and sheaths formed.

1.2.1 Collision processes of electrons

Electrons play an important role in the chemical and physical processes that occur in plasmas due to being a charged species and having low mass. It is this combination of properties that allows them to react first to electric fields, and then to transmit this energy to other species in the plasma by collision. They can react with other atoms or molecules in a variety of ways as shown in Table 1-1.

Process	Reaction		Comment
Elastic collision of electrons with atoms and molecules	$e + A \rightarrow e + A$	**Reaction 1-1**	1
Inelastic collision of electrons with atoms and molecules	$e + A \leftrightarrow e + A^*$	**Reaction 1-2**	2
Ionization of atoms or molecules by electron impact	$e + A \rightarrow 2e + A^+$	**Reaction 1-3**	3
Dissociative attachment of an electron to a molecule	$e + AB \rightarrow A + B^-$	**Reaction 1-4**	4
Dissociative recombination	$e + AB^+ \rightarrow A + B^*$	**Reaction 1-5**	5
Dissociation of a molecule by electron impact	$e + AB \rightarrow e + A + B$	**Reaction 1-6**	6
Electron attachment to an atom	$e + A \rightarrow A^-$	**Reaction 1-7**	7
Electron attachment to an atom in three-body collisions	$e + A + B \rightarrow A + B^-$	**Reaction 1-8**	8
Electron-ion attachment in three-body collisions	$2e + A^+ \rightarrow e + A$ $e + A^+ + B \rightarrow A^* + B$	**Reaction 1-9**	9

Table 1-1: Collision processes of electrons with atoms and molecules[11]

1. One of the most basic ways two particles can interact with each other is by colliding. Collisions can be categorised as either elastic or inelastic. Elastic collisions are defined as when the total kinetic energy before the collision is equal to the total kinetic energy after the collision, the processes is simply a scattering one. They occur when the electron has insufficient energy to excite any of the energy levels of an atom or molecule.
2. When a molecule or atom undergoes excitation by electron impact, typically the electron furthest from the nucleus is excited to a higher energy level. However it is necessary for the impact electron to have significantly more

energy than the energy difference between the two levels (transition energy). This is due to conservation of angular momentum and the cross section increase with higher energies. The maximum cross section can be obtained at several electron volts higher for heavy atoms and several tens of electron volts for lighter atom (the electron energy should be greater than the transition energy by at least a factor of two).

3. This process is fundamental to the creation of the discharge and is discussed in section 1.5.1 for flames and section 1.3 for direct current discharges.
4. During dissociative attachment by an electron, the electron is first captured by a molecule in an autodetachment state (a negative ion that can decay to produce a free electron as in Reaction 1-10) to produce the intermediate $(AB^-)^*$.

$$A^- \rightarrow A + e + KE$$

Reaction 1-10

This excited intermediate is unstable and either decays to its original reactants or dissociates. The initial transition from the ground state to the autodetachment state is governed by the Frank-Condon principle.

5. In dissociative recombination the energy involved at the start is rather large as it is equal to the ionization energy of the molecule (AB). The process begins by an electron being captured which places the molecule in an intermediate repulsive autoionizing state $(AB)^*$. The atoms then move apart till energetically the system cannot revert back to the autoionizing state and the molecule splits apart. The resulting atoms can either be excited or non-excited.
6. Dissociation of a molecule by direct electron impact can take place by forming either a vibrational or electronic excited state first. Vibrational excitation leading to dissociation only occurs for a selected group of gasses such as N_2, CO_2, H_2 and CO. This is a non-direct and multistep process which requires energy to be exchanged between multiple molecules to obtain enough vibrational energy for dissociation. Electronic excitation on the other hand is often induced by a single collision. In this process the excitation state can be repulsive or attractive state. For the repulsive state, the energy of the fragments separated by infinity is the lowest energy thus will break apart.

However for the attractive state, the initial electron impact will need to provide enough energy so that the excited state they are in will have a higher energy than the fragments.

7. The simplest electron attachment mechanism is of a neutral capturing an electron to for an anion. This is most likely to occur when the other shell of the neutral is nearly full (chlorine, fluorine and oxygen) and is measured by the electron affinity of the gas. The probability of this process happening is very low given the number of levels which the electron can attach to is typically one, thus an exact energy is needed for this process.
8. When collisions occur and one particle becomes bound, unless the exact energy is given a third body is needed to dissipate the extra energy. In the case of electron attachment in a three body collision, the electron is being bound and two particles are used to dissipate the extra energy. The three body attachment process can be the dominant process when at high pressures (atmosphere) and if the electrons don't have enough energy to undergo dissociative attachment (Reaction 1-4). In this process the electron temperature is less important and instead the particle is the responsible for the absorbing the energy released.
9. In high density plasmas it is the three body electron-ion attachment reaction that is important. The recombination starts with an electron capture to the excited state. This excited state can then lose its energy by another electron capture till it reaches the ground state. This process is known as step by step deactivation.

1.2.2 Collision processes of ions

While the electrons are fast moving and will facilitate most of the reaction in a plasma, ions can also undergo reactions as shown in Table 1-2.

Process	Reaction		Comment
Mutual neutralization of ions	$A^+ + B^- \rightarrow A + B$	**Reaction 1-11**	1
Decay of negative ions in atomic collisions	$A + B^- \rightarrow AB + e$	**Reaction 1-12**	2
Ion-molecular reactions	$A^+ + BC \rightarrow AB^+ + C(AB + C^+)$	**Reaction 1-13**	3
Conversion of atomic ions to molecular ions in three-body collisions	$A^+ + B + C \rightarrow AB^+ + C$	**Reaction 1-14**	4
Ion-ion recombination in three-body collisions	$A^+ + B^- + C \rightarrow A + B + C$	**Reaction 1-15**	5

Table 1-2: Collision processes involving ions[11]

1. When the plasma is made of eletro-negative gases, negative ions can form. These can recombine with the positive ions through collision. During the mutual neutralization of ions the process has second-order kinetics and is the dominate process in low pressures.
2. The decay of a negative ion proceeds similarly to the process of associative ionization. The difference being that the energies involved are slightly higher thus the intermediate $(AB)^*$ is autodetaching, thus releasing an electron.
3. The process of converting atomic ions to molecular ions in a three-body collision starts with the ion inducing a dipole moment in the neutral molecular as it travels towards it. This creates an attractive force that aids in the collision. This attractive potential can be expressed in terms of the dipole moment in equation 1-1 where α is the polarizability of the neutral atom or molecule. If the energy between the induced dipole and ion becomes of the order of the kinetic energy, the paths of the ion and molecule can be placed in a collision course.

$$p_m = \alpha \varepsilon_o E = \alpha \frac{e}{4\pi r^2} \qquad \textbf{1-1}$$

4. In a three body collision process where atomic ions are converted to molecular ions the polarization interaction between the initial ion and atom is important similar to ion-molecule reactions (Table 1-2 comment 3). When dealing with

identical ions and atoms the ion-atom exchange interaction may also need to be considered. As the process is a three body reaction the Thomson theory also needs to be taken into consideration as in ion-ion recombination by three body collision (Table 1-2 comment 6).

5. In high pressure plasmas (p > 10-30 Torr) the ion-ion recombination by three-body collision is one of the dominant processes. The process is governed by the Thomson theory and at high pressures or higher neutral species concentration, the Langevin model. One of the assumptions of the Thomson theory is that the ion pair will only combine if the total relative energy is negative (the combined product is more favourable than the pair separated at an infinite distance). If only the two ions are involved, this reaction is impossible as there is no way to dissipate energy to make the total relative energy negative, this imposes there to be a third body. If however there is a third body and their Coulomb energy is near the thermal energy (temperature of the gas or heaviest particle), a recombination can take place. Physically this represents the energy needed to capture each other is greater than the random motion that will split them apart.

   Another assumption of the Thomson model requires the capture distance be less than the ion mean free path and thus doesn't consider collisions with other neutrals. The Langevin model accounts for this using mobilities and accurately predicts recombination is less likely at very high pressures or neutral concentrations.

1.2.3 Mobility and ambipolar diffusion

In plasmas the positive ions and electron are free to diffuse or more commonly when an electric field is present, migrate. This movement is described by the Einstein relation which relates diffusion (D) and mobility (μ) with thermal energy (T) and charge (q) as show in equation 1-2.

$$\frac{D}{\mu} = \frac{T}{q} \quad \textbf{1-2}$$

The mobility of electrons (μ_e) can also be determined using the collision frequency between electrons and neutrals (υ_{en}) as shown in equation 1-3, where e is the charge of an electron and m_e the mass of an electron.

$$\mu_e = \frac{e}{m_e}\frac{1}{\upsilon_{en}} \quad \textbf{1-3}$$

By considering electrons as the only charge carriers, a reasonable assumption due to their high mobility, we are able to determine the mobility of the electron using the current density and electron density. Current density (*j*) is related to the conductivity (σ) and electric field (*E*) as in equation 1-4, and conductivity is a function of the electron density (n_e) and collision frequency of between electrons and neutrals (υ_{en}) as shown in equation 1-5. Solving for the collision frequency and using the value in equation 1-3 will give the electron mobility.

$$j = \sigma E \quad \textbf{1-4}$$

$$\sigma = \frac{n_e e^2}{m\upsilon_{en}} \quad \textbf{1-5}$$

In plasmas where the density of electrons and positive ions are high, a phenomenon known as ambipolar diffusion occurs. This slows down electron diffusion, but speeds up ion diffusion and causes the charged particles to act together. To understand this effect consider an equal and large concentration of electrons and positive ions are placed together at the centre of an empty large box. Due to the large difference in mass

between positive ions and electrons, their mobility and hence diffusion rates as described in equation 1-2 will be vastly different. At the start this will allow the electrons to spread towards the outer edges of the box rapidly while most of the slow positive ions will remain at the centre, only slowly diffusing outwards. Once this has happened an electric field will be created radiating from the positive ions at the centre towards where the electrons are. This field arises as the area in the centre has a net number of positive ions at the centre due to the starting electro-neutrality condition and the electrons being spread out. As the electrons travel further from the large number of remaining positive ions at the centre, they are slowed down due to the electric field drawing them back, corollary the positive ions are drawn towards the outer electrons. This effect causes both the positive ions and electrons to move together with the ambipolar diffusion coefficient (D_a). The ambipolar diffusion coefficient described in equation 1-6[12] is a function of the diffusion coefficients of ion (D_i) and electron (D_e) and mobility of ion (μ_i) and electron (μ_e).

$$D_a = \frac{D_i\mu_e + D_e\mu_i}{\mu_e + \mu_i} \quad \textbf{1-6}$$

Given that typically $\mu_e \gg \mu_i$ and $D_e \gg D_i$ and using equation 1-2, we can reduce equation 1-6 to equation 1-7.

$$D_a \approx D_i + \frac{\mu_i}{e}T_e \quad \textbf{1-7}$$

From equation 1-7 it can be seen where $T_e = T_i$ (“hot” plasmas) $D_a = 2D_i$ however when $T_e \gg T_i$ (“cold” plasmas) we get equation 1-8[13].

$$D_a = \frac{\mu_i}{e}T_e \quad \textbf{1-8}$$

1.2.4 Debye shielding

One of the characteristic properties of plasmas is their ability to shield the bulk from electric potentials. The concept of shielding was made by Debye and Huckel in 1923[14] when they studied strong electrolytes. To understand this effect, imagine placing a large positively charged sphere in a plasma, which does not recombine with the electrons in the plasma to produce a neutral. As electrons are free to move, they will be attracted by the positive electric field from the positive sphere and migrate to surround it. As more electrons migrate they will shield the positive electric field from the electrons further away, and thus the electric field decreases as a function of distance from the positive sphere. If the electrons had very little thermal energy we can imagine at some distance away from the positive sphere the electric field will be zero due to the field being full screened. At this point the charge from the electrons surrounding the positive sphere will equal the charge of the positive sphere and the only electric field present will be within this cloud of electrons shielding the positive sphere. However if the electrons have high thermal energy those electrons that are near the point where the electric field is near zero will be able to escape the weak electric field due to their large velocities. In this case the distance up to where the positive sphere has an effect is when the screened electric potential field is equal to the thermal energy of the electrons, kT_e. Thus potentials of the order of $\frac{kT}{e}$ will not be screened and can form electric fields.

In order to calculate an approximate thickness of the cloud of electrons that may form we will make several assumptions. The first is that the Boltzmann distribution can be used to describe the electron distribution function as described in equation 1-9 where n_e is the density of electrons, and n_∞ is the density far away, e is the charge of the electron, ϕ is the electric field, K is the Boltzmann constant and T_e the electron temperature.

$$n_e = n_\infty \exp\left(\frac{e\phi}{KT_e}\right) \qquad \textbf{1-9}$$

By using the Poisson equation as shown in equation 1-10 where ε_0 is the dielectric constant of vacuum we can derive a function for the electric field ϕ.

$$\varepsilon_0 \nabla^2 \phi = -e(n_i - n_e) \quad \textbf{1-10}$$

As mentioned before in order for an electric field to form, the energy of the electrons (kT_e) needs to be greater than the electric field ($e\phi$), using this we can simplify the exponential in equation 1-9 by expanding it and taking for first term. Using the assumption that the density of ions is constant and thus equal to the density far away ($n_i = n_\infty$), and the simplified form of equation 1-9 we get equation 1-11.

$$\varepsilon_0 \nabla^2 \phi = -e\left(n_\infty - \left(n_\infty \left[1 + \frac{e\phi}{KT_e}\right]\right)\right) = \frac{n_\infty e^2}{KT_e}\phi \quad \textbf{1-11}$$

Finally solving equation 1-11 we get equation 1-12, where λ_D also known as the Debye radius is shown in equation 1-13[15].

$$\phi = \phi_0 \exp\left(\frac{-|x|}{\lambda_D}\right) \quad \textbf{1-12}$$

$$\lambda_D = \sqrt{\frac{\varepsilon_0 KT_e}{n_\infty e^2}} \quad \textbf{1-13}$$

The Debye radius is an important parameter for plasmas as it indicates the distance where the plasma behaves as one.

1.3 Discharge creation

A discharge is a body of ionized gas created by applying a voltage between two electrodes and a dielectric (the gas). The creation of a discharge is dependent on properties such as pressure and type of gas, along with electrode geometry. By manipulating the applied voltage various discharges can be created[16] as shown in Figure 1-2. This thesis focuses on the Townsend and corona discharges. It is important to note a corona discharge is only formed when the two electrodes are highly asymmetric, which causes high electric fields to form around one electrode compared to the other.

Each discharge also has a typical current – voltage characteristic that can be seen in Figure 1-2. For example the corona discharge forms at high potentials but can only transfer low currents, whereas arcs can transfer large amounts of current at low voltages. The first discharge that will be discussed is the Townsend discharge followed by the corona.

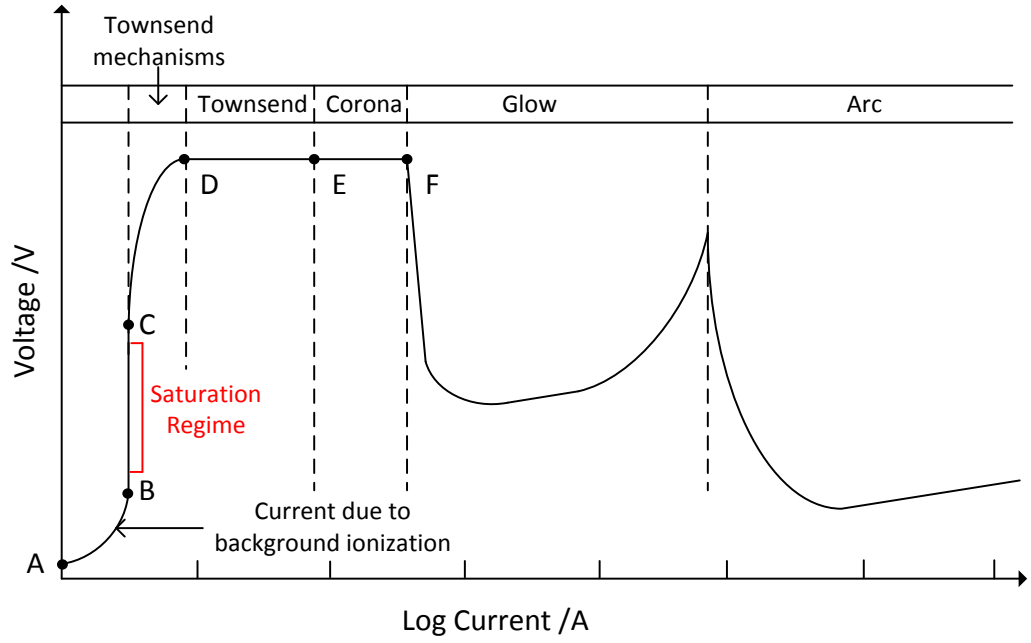

Figure 1-2: Current – voltage graph of different discharges formed when applying a voltage between two electrodes and a gas.

1.3.1 Townsend discharge

The Townsend discharge is the first discharge that is formed as shown in Figure 1-2 and is between point D and E. It is dark to the eye, silent and is used in gas phototubes. The formation of the Townsend discharge is important in understanding other discharges such as corona, glow and some arcs, as it must be created first before it can be transformed into the discharges mentioned. The Townsend discharge is governed by an avalanche process of electrons.

1.3.1.1 Ionization mechanism

Before point C, the only free electrons around are those created by photoionization, cosmic rays, or other natural sources. These free electrons are what enables a current to be passed between points A and B. As it can be seen between points B and C, a saturation region appears and this is caused when all of the free electrons have been collected, thus the additional electric field has no effect. This current will be defined as i_0 which represents the current due to the primary or free electrons.

From point C to point D, the electric field applied accelerates the free electrons until their kinetic energy is able to ionize the neutral atoms and the increase in current illustrates this[17]. At high enough electric fields the electrons that have just been produced, are also able to ionize other neutrals, and the initial electron able to ionize another neutral, this mechanism is described by the Townsend coefficient α. Specifically the coefficient relates the number of electrons an electron is able to produce, (by ionizing other atoms) in a path length of 1 cm[18]. By considering a path length of dx, dn number of electrons will be produced as shown in equation 1-14 and solving to obtain equation 1-15.

$$dn = \alpha n dx \quad \textbf{1-14}$$

$$n = n_0 e^{\alpha x} \quad \textbf{1-15}$$

Or

$$i = i_0 e^{\alpha x} \quad \textbf{1-16}$$

Where n and n_0 are the number of electrons and initial number of electrons respectively. By using Faraday's constant these values can be thought of in terms of current and the two (current and number of electrons) will be used interchangeably. The initial electron concentration n_0 can be found by the saturation current in Figure 1-2.

It is helpful to introduce the reduced electric field before going further which shows the close relationship (linear) between electric field and pressure. Increasing the applied electric field can have the same effect as lowering the pressure. This is expressed as

$\left(\frac{E}{N}\right)$ where E is the electric field and N the neutral gas number density, and uses the Townsend units of Td (1 Td = 10^{-17} V cm^2).

1.3.1.2 Cathode emission

While the α coefficient explains the behaviour ionization in the body of the gas, another coefficient known as the Townsend coefficient γ is used to express the mechanism at the cathode. This γ coefficient relates to how many electrons the positive ions create at the cathode, and is dependent on the cathode material, surface, gas and reduced electric field. First we will assume that one electron will go on to produce $(e^{\alpha x} - 1)$ electrons, obtained from equation 1-16 and subtracting the initial electron. We will then assume that there are an equal number of positive ions that will reach the cathode. At some high enough electric field, these positive ions can impact the cathode with enough energy to free electrons. These electrons can then ionize other atoms, thus producing more positive ions. This process is given by equation 1-17 where i_0 are the free electrons and can be rearranged to give equation 1-18[13].

$$i_{cath} = i_0 + \gamma[i_{cath}(e^{\alpha x} - 1)] \quad \textbf{1-17}$$

$$i_{cath} = \frac{i_0}{(1 - [\gamma(e^{\alpha x} - 1)])} \quad \textbf{1-18}$$

1.3.1.3 Townsend breakdown and critical breakdown condition

Finally to obtain the total current from the external circuit at the anode we will make the assumption that electrons are the sole charge carriers. Combining the equation expressing the number of electrons a single electron can produce (1-16), and the equation relating the number of electrons produced at the cathode (1-18), we obtain equation 1-19. It is important to mention these are the two processes that govern the Townsend breakdown mechanism.

$$i = i_{cath}e^{\alpha x} = \frac{i_0}{(1 - [\gamma(e^{\alpha x} - 1)])}e^{\alpha x} \quad \textbf{1-19}$$

By considering the denominator of equation 1-19 we are able to infer some properties about the current in the gap. At positive values the current is non-self-sustaining, meaning the number of electrons produced by ionization is not enough to continue producing more electrons to reach the other side. However, as the denominator goes to zero the current propagating between the gap becomes self-sustaining and breakdown occurs. This is shown in equation 1-20 and rearrange in equation 1-21.

$$[\gamma(e^{\alpha x} - 1)] = 1 \quad \textbf{1-20}$$

$$\alpha x = \ln\left(\frac{1}{\gamma} + 1\right) \quad \textbf{1-21}$$

With an expression to describe breakdown now formulated we can use the reduced electric field $\left(\frac{E}{n_0}\right)$, and the similarity parameter $\left(\frac{\alpha}{n_0}\right)$ to find the breakdown voltage. Von Engel and Steenbeck[19] developed an expression empirically shown in equation 1-22 where parameters A and B can be found experimentally.

$$\left(\frac{\alpha}{n_0}\right) = A\exp\left(\frac{B}{\left(\frac{E}{n_0}\right)}\right) \quad \textbf{1-22}$$

By combining equation 1-21 and equation 1-22 we are able to determine the breakdown voltage as a function of pressure, distance, α (by parameters A and B) and γ. This is done by taking logs of both sides from equation 1-22 and rearranging for $\left(\frac{E}{p}\right)$, then substituting α using equation 1-21 to give equation 1-23.

$$\frac{E}{p} = \frac{\ln A\,(B)}{\ln\left[\left(\frac{\ln\left(\frac{1}{\gamma} + 1\right)}{x}\right)\frac{1}{p}\right]} \quad \textbf{1-23}$$

To simplify the expression we will substitute $C = \ln A - \ln\ln\left(\frac{1}{\gamma} + 1\right)$ then finally using the relationship between electric field and voltage we obtain equation 1-24.

$$V = \frac{B(px)}{C + \ln(px)} \quad \textbf{1-24}$$

Plotting equation 1-24 can give an insight into breakdown as a function of the similarity parameter px. The plots formed are known as Paschen curves and an example is shown in Figure 1-3.

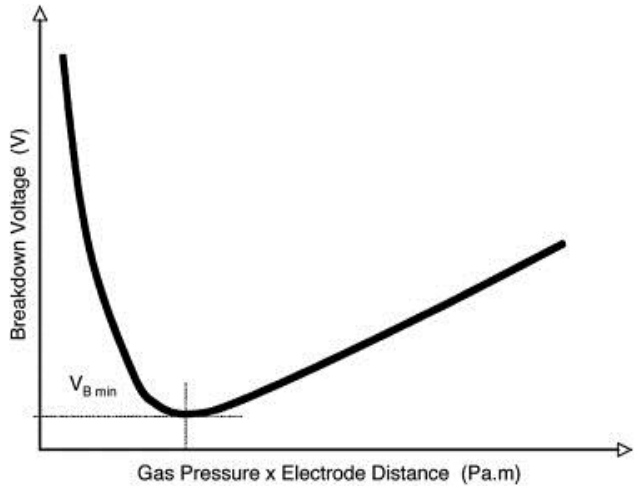

Figure 1-3: Characteristic shape of a Paschen curve where V_B is the DC breakdown voltage[20].

The curves show the competing factors of too few neutrals (pressure is to low) to the left of the minima and too many neutrals (to the right of the minima). Typically the curve minimum is where the mean free path of the electron is equal to the electrode separation[21].

1.3.1.4 Role of electron attachment

So far we have only considered the ionization rate of the neutrals and electron emission of the cathode by the Townsend coefficient α and λ respectively. This is adequate when the distance between the electrodes are small or the pressure involved is low. At higher pressures or longer distances the ability of the gas to reduce the number of electrons by electron attachment must be considered and will be done so using the Townsend coefficient β[22]. The processes of electron attachment can be thought of as decreasing the amount of available electrons over distance. It is important to remember that although electron attachment creates anions, the Townsend coefficient α and λ are only concerned with electrons. As the β coefficient describes the effect of electron attachment, it also accounts for the electronegativity property of gasses. When comparing the Townsend coefficients β and α, the α

coefficient dominates at low $\left(\frac{E}{N}\right)$ values and β can be neglected. However at high values (large gaps) and electronegative gases, the breakdown is limited by the attachment processes[13]. As expected higher values of the reduced electric field are required in the breakdown of electronegative gases. Modifying equation 1-14 which gives the number of electrons produced by ionization with the β coefficient yields equation 1-25 where n_e is the number of electrons, and solved to give equation 1-26.

$$dn_e = (\alpha - \beta) n_e dx \quad \textbf{1-25}$$

$$n_e = n_{e0} e^{(\alpha-\beta)x} \quad \textbf{1-26}$$

Or

$$i = i_0 e^{(\alpha-\beta)x} \quad \textbf{1-27}$$

1.3.1.5 Streamer mechanism

So far the breakdown mechanisms that have been discussed are quasi-homogeneous and occur only at low reduced electric fields. For higher reduced pressures instead of the Townsend mechanisms taking place, streamer mechanisms[23–25] do. While the Townsend breakdown is quasi-homogeneous, the streamer breakdown does so in a very narrow primary channel with an avalanche head. Both discharges are based on electron cascades; however it is the mechanism governing the production of the secondary electrons that makes them different. While the secondary electrons in the Townsend discharges comes from the cathode as described in section 1.3.1.2, they come from within the gas for the streamer.

Once an electron cascade starts to form (section 1.3.1.1) a large number of positive ions and electrons are produced, concentrated in the cascade. As mentioned at low pressures the density of each allows electron attachment (section 1.3.1.4) to be largely ignored and only considered at long path lengths. In high pressures however, not only does electron attachment take effect, collisions of electrons as described in section 1.2.1 also do. In particular it is the inelastic collision of electrons with atoms and molecules (Reaction 1-2) and Electron-ion attachment in three-body collisions (Reaction 1-9) that start to play a role. These reactions create atoms or molecules in an

excited state within the electron cascade. These excited particles decay by photo-emission as shown in Reaction 1-16 where h is planks constant and f the frequency of the emitted photon.

$$A^* \rightarrow \mathrm{A} + \mathrm{h}f$$

Reaction 1-16

These highly energetic photons travel out of the electron cascade and into the area in front of the plasma and photo-ionize the neutrals in this region. It is this process that creates the secondary electrons. These electrons are able to either feedback into the main ionization region or cause additional avalanches. The avalanches created are known as streamers and the electrons created within them are again able to feedback into the main ionization region or go on to create more avalanches. This mechanism of creating additional avalanches to propagate the plasma is known as the streamer mechanism.

One important criteria for when a streamer forms was introduced by Meek. They found that the electric field generated due to space charges from the ions at the avalanche head, is equal to the external electric field in streamer discharges[26]. This is shown in equation 1-28[27] where E_a is the electric field generated by space charge effects, r_A the radius of the avalanche head and E_0 is the external electric field.

$$E_a = \frac{e}{4\pi\varepsilon_0 r_A^2} \exp\left[\alpha\left(\frac{E_0}{p}\right)x\right] \approx E_0 \qquad \textbf{1-28}$$

1.3.2 Corona discharges

After a Townsend discharge is formed, a corona discharge maybe formed by applying higher voltages to the same system. Coronas can be found in a wide range places from ozone production to photocopying machines. Coronas only form with some electrode geometries and if created occurs from points E to F in Figure 1-2.

In coronas it is the difference in electric field between bulk and near the electrodes that allows the streamer mechanism to occur. More specifically the electrode geometry

configurations must support electric fields that are stronger around one or both of the electrodes compared to the gap between. Typical examples of this are highly asymmetric electrodes, like a point opposite a plane, and a wire through a cylinder. In these cases the electric field is highly concentrated near the point or around the wire. Creating coronas can be a challenge as a balance must be found between the size of the electrode which causes high electric fields and the spacing between the two electrodes. Using a point that is too small can make it difficult to create a corona discharge as smaller points reduce the voltage range a corona can be formed. Applying a voltage to low will result in no formation of discharge while to high a spark discharge will form instead. As different mechanisms can take place depending on the polarity of the point electrode, it is common convention to name the polarity of the corona after the electrode with high electric field. For example a corona formed using a point to plane configuration is negative if the point is negative.

1.3.2.1 Negative corona

The negative corona is similar to the Townsend discharge as the secondary electron generation in both come from the cathode. The negative corona uses photons and the photoelectric effect as well as bombardment of positive ions to generate secondary electrons. Negative coronas can only form in electronegative gases such as O_2 as these molecules are needed to capture the free electrons to form negative ions. Without these an arc will form instead. When they are made negative coronas can form different types of discharges as shown in Figure 1-4.

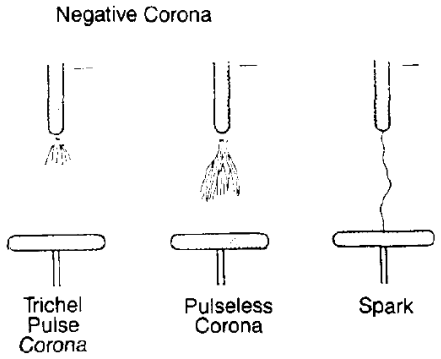

Figure 1-4: Diagram illustrating different types of negative corona that can form[28].

When applying a negative voltage between two electrodes and increasing the potential applied, the first type of corona to form is the Trichel pulse corona[29]. When measured, it displays a current waveform of regular pulses. Each pulse has a fast rise time of short duration but a long period of low current between each pulse. The fast current rise times have been attributed to rapid ionization and subsequent drop due to a dense plasma forming near the cathode which causes a cathodic drop. This drop reduces the electric field and thus current measured[30].

After a Trichel corona is formed applying higher voltages allows a pulseless corona to form. This discharge visually has been described to be similar to a glow discharge[31,32] found in low pressures. The transformation from Trichel to glow can be explained by the higher voltages applied to the system. At some applied voltage the electric field generated between the two electrodes allows ionization to happen anywhere in the gas[33].

Finally at high enough voltages when the ionization region reaches the other electrode the discharge transforms into a spark discharge. This discharge is similar to an arc in that high amounts of current can be carried through a narrow channel and the electrons come from the electrode.

1.3.2.2 Positive corona

The positive corona is generated using the same streamer mechanisms. The secondary electrons come from within the gas and are produced by photoionization. Similarly to the negative discharge different types of positive discharges can form as shown in Figure 1-5.

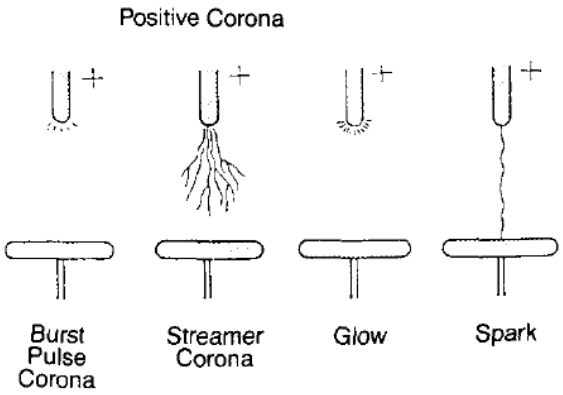

Figure 1-5: Diagram illustrating the types of corona discharges that can form[28].

When applying a positive voltage between two electrodes and increasing the potential the first discharge to form is the burst pulse corona. During this phase, the electric field is high enough such that electrons can create avalanches (section 1.3.1.1) but are externally sustained[16]. At higher electric fields the streamer corona is formed due to photoionization of the gas. In this phase the electric field produces electrons as described in the streamer mechanism (section 1.3.1.5). In both phases space charge effects slowly build up at the positive electrode and eventually quench the discharge over time.

The next discharge to form is the glow corona discharge which actually pulses very rapidly ~ 0.1 - 1 MHz[34,35] and is sometimes known as the Hermstein glow. Morrow 1997[36] explains the mechanism using successive shells of positive ions to carry the current, while seed electrons produced from negative ions such as metastable oxygen molecules trigger the release of each shell.

Finally after applying a high enough electric field the ionization region reaches the other side and a spark forms in the same way the negative spark occurs.

1.4 Discharges for environmental usage

Discharges can have various applications depending on the processes that undergo within them. One application is for environmental purposes. As electrical discharges can be created in numerous ways Table 1-3 shows some of the literature dealing with understanding the chemical processes that occur in various discharges. The environmental application and the author's method of generating their discharge is also listed.

Discharge types	Geometry	Application	Comments	Reference
Corona discharge in atmospheric flames	-	-	Theoretical investigation into the properties of plasmas generated by discharges in flames.	[37]
DC and AC Positive and Negative Coronas in low pressure flames	Point to point	Spark ignition	Investigates the effect different discharges have on spatial distribution of N_2, CO, OH.	[38]
DC and AC Corona discharges in atmospheric flames	Point to point x3 in circular arrangement around flame	Soot control using discharges	Investigates the use of corona discharges in the formation of soot.	[39]
Positive and negative Corona discharge Glow discharge	Various	CO_2 reduction in coronas in air	Investigation of the reaction mechanisms of CO_2 and O_3 in air with Ar.	[28]
Corona discharge Glow discharge	Various	CO_2 utilization in non-thermal plasmas	Investigates various CO_2 reaction mechanisms to CO or higher organics.	[40]
Positive and negative Coronas at low pressure	Wire to plane	CO_2 and CO reduction in CO_2 – air and CO – air mixtures	Investigates the effect of different wire (Mo, Mo, Cu) and plates (SS, Brass, Brass) on CO_2 reduction.	[41]
Coronas at atmospheric pressure	Wire to plane	Decomposition of pure CO_2 in to CO and O_2	Investigation into the reaction mechanism of CO_2 reduction	[42]
Positive and negative Corona discharge at atmospheric pressure	Point to plane (plane is a MS orifice)	Corona discharges in N_2O with < %0.1 H_2O	Investigates clustering of NO_x ions with H_2O to form clusters.	[43]
Positive Coronas at atmospheric pressure	Multi needle to plane	Reduction of NO, NO_2, N_2O in N_2:O_2:CO_2 and N_2:O_2:CO_2:NO_2 mixtures	Investigates reduction of NO_x as a function of different O_2 concentrations.	[44]
Negative Coronas at atmospheric pressure	Hollow needle to plane	Reduction of NO_x from simulated flue gases (N_2:O_2:CO_2:NO)	Investigates the use of injecting methane radicals through a hollow needle into a formed corona and the effect of NO_x chemistry.	[45]

Positive Streamer corona at low pressure	Wire to cylinder	NO reduction in N_2:NO:CO_2:O_2 mixture	Investigates the effect of CO_2 on NO_x removal and effect on N_2O, O_3 and CO in streamer plasmas.	[46]
Positive Streamer corona at low pressure	Wire to cylinder	NO reduction in N_2:NO:CO_2:O_2 mixture	Investigates spatial and surface removal of NO_x as a function of wire material (Mo, Cu, Brass, SS) against brass plane.	[47]
Glow discharge at low pressures	Plate to plate	Decomposition of NO_2 in NO_2 – air mixtures	Investigates electron impact ionization and attachment coefficients of NO_2.	[48]

Table 1-3: Table showing literature dealing with chemical processes in the discharge with their environmental applications. Table is separated into flame discharge hybrids followed by townsend and corona discharges. Discharge creation and comments on regarding their investigations are presented.

1.5 Flames

A flame is a hot body of gas produced by a chemical reaction between an oxidant and fuel. Depending on how the two are mixed will result in different structures. When the fuel is not mixed with the oxidant, a diffusion flame is produced. These flames are much larger than their counterparts and are governed by the rate of diffusion of the oxidant; a candle is a typical example of this type of flame. In contrast, premixed flames are produced when the fuel and oxidant are mixed before combustion. They are smaller, more stable, have well defined zones and structures, and are the type of flames used in this thesis. Both flames can also be controlled by adding a third gas which is inert. The gas cools the flame and can also change their structure.

As mentioned, premixed flames have well defined zones and are typically split into three zones, a transport zone, followed by two reaction zones[49]. The transport zone is where the oxidant and fuel are governed by diffusion and thermal processes from interacting with the much hotter zones above it. Just above is the primary reaction zone where combustion takes place which produces ions and radicals, and is also the hottest part of the flame and most luminous. The zone above it is where the excess radicals recombine to achieve equilibrium.

1.5.1 Ionisation processes

Due to the primary reaction zone describe in section 1.5, a flame can be thought of as a plasma where the electrons and ions (produced by combustion) can move freely. Because of this they are considered as a “hot” plasma. Comparing flames to typical plasmas in Figure 1-1 we see flames having an electron density between 10^9 – 10^{11} per cm^{-3}. While ionization can take place by collision, electron transfer, excited states, the most common is chemi-ionization in flames.

Ionization by collision

With flames typically having high temperatures (>1500K) it would seem that the ions are produced by thermal ionisation as in Reaction 1-17 and Reaction 1-18[50]. However

although flames have a high temperature, they are actually not hot enough to be the dominant process.

$$A + B \rightarrow A^{+} + B + e^{-}$$

Reaction 1-17

$$A + e^{-} \rightarrow A^{+} + e^{-} + e^{-}$$

Reaction 1-18

Reaction 1-17 represents a reaction between two neutral molecules and by using the conservation of momentum, kinetic energy and assuming an elastic collision we get equation 1-29.

$$U_{max} = \frac{1}{2}\frac{AB}{(A+B)}\left[\frac{(Av_r - Av_1)}{B}\right]^2 \qquad \textbf{1-29}$$

From equation 1-29 we see that only half the relative kinetic energy can be converted into ionization potential energy when the masses and velocity are near equal ($A \cong B$). It is therefore much more likely that ionization would take place by Reaction 1-18 given that the temperature (velocity) of both ions and electrons are the same, however the mass of the electron is much smaller ($B \ll A$). The temperature range for the electron are typically between 0.1 eV and 1.0 eV for combustion systems, and comparing this value with Table 1-4 we can conclude collisional ionization doesn't take place often.

Species	Ionization potential in eV
H	13.595
N	14.53
O	13.614
H_2	15.427
OH	13.18
H_2O	12.6
CO	14.05
Cl	13.01
Br	11.84

Species	Ionization potential in eV
O_2	12.2
CO_2	13.84
NO	9.25
CH	11.13
CH_2	11.82
CH_3	9.905
CH_4	13.06
CHO	9.88

Table 1-4: Table showing ionization potentials of commonly found neutrals in a flame

Electron transfer

When ionization takes place by electron transfer, it takes place as in Reaction 1-19. Energetically this means a lower potential energy is required for the reaction. An example of this is the reaction $K + Cl \rightarrow K^+ + Cl^-$ which can occur when doping a flame requiring only 0.6 eV[50]. Comparing this to the mentioned 0.1 – 1.0 eV typically found in combustion systems this reaction is likely to happen.

$$A + B \rightarrow A^+ + B^-$$

Reaction 1-19

Ionization by transfer of excitation energy

Ionization can also take place by the transfer of excitation energy as shown in Reaction 1-20(also known as Penning ionization). In this reaction excess energy can be transferred by the electron and kinetic energy of the initial reactants used when there is a deficit.

$$A + B^* \rightarrow A^+ + B + e^-$$

Reaction 1-20

Chemi-ionization

Finally there is chemi-ionization which is believed to be the dominant producer of ions. This takes place when two neutral species react chemically to produce ions either with an electron as in Reaction 1-21 or just ions as in Reaction 1-22.

$$A + B \rightarrow C^+ + D + e^-$$

Reaction 1-21

$$A + B \rightarrow C^+ + D^-$$

Reaction 1-22

$$CH + O \rightarrow CHO^+ + e^- \qquad \Delta H \cong 1 \text{ eV}$$

Reaction 1-23

It is believed that the chemical rearrangement of the molecule is where the potential energy originates from. An example of this is Reaction 1-23[51] with a reaction rate constant of 3 x 10^{-12} cm^3 s^{-1} and it can be seen the energy required is near the electron temperature range of 0.1 – 1.0 eV.

1.5.2 Electrical aspects of flames

Work was first carried out by Thomson studying the conduction of electricity through different gaseous environments such as air and oxygen[52]. It was then shown that when using coal or natural gasses as fuel for a flame, the resistivity was found to be in the million ohms per cm[53]. From ion profiles it was found that maximum conductivity occurred in the luminous reaction zone[54]. Wilson and others[55–57] expanded on this by studying the electrical properties of flames. For example it was shown that at small distances around 3 mm a sheath is formed[56].

There have been various attempts to increase the conductivity of flames. The most common method used dissolved alkaline salt vapour solutions. It was found that they could increase the ion concentration to more than 10^{17} ions m^{-3} when alkali salts were sprayed [53,58].

The electrical aspects of flames was studied in more depth by the use of the electrostatic (Langmuir) probe to determine the ion concentration[59–64]. Various authors have attempted this study theoretically[65,66] and experimentally report a range of values from as high as 4x10^{17} ions m^{-3} [(67)] to a lower value of 4x10^{16} ions m^{-3} [(59,61,68)]. Recently Goodings has used both electrical and mass spectrometric analysis to probe ions in flames. This was done by using a burner top as one electrode and a mass spectrometer inlet as another[6,69,70].

Lawton and Weinberg[71] also explored the maximum current that can be passed through a flame. They found that when two electrodes were separated by 0.5 cm apart (this was the minimum distance they could achieve) the maximum current density was 250 μA cm^{-3} before breakdown of the gas at the electrodes occurs.

Finally, although it was established that a potential difference can arise when two metals are placed in the flame, various different theories describing the origin of these

potentials has been suggested. The calorelectric effect suggests that the potential arises due to temperature differences[72] which can produce 1 to 10 volts when the temperature differs by about 500°C[73]. Others have suggested it is the diffusion of positive ions and electrons that gives rise to the potential measured[74–76]. In particular Caruana, has shown using a system where two flames of different ionic concentration are in contact with each other, that when the ionic concentration are equal, the potential difference between two metals is zero. However varying the ionic concentration of one flame has shown that the potential generated follows the Nernst equation[77]. Work also done by Caruana indicates that a potential is generated when the electrodes used are not of the same metal[78] and could be due to redox reactions taking place[79]. It is likely that the potential difference generated from two metals placed in a flame is the result of the combination of the various proposed theories.

1.6 Review of augmenting flames using electric fields

Modification of flames by electric fields can be traced back to Brande in 1814[80] where he placed a flame between two electrodes and described the flame leaning towards the negatively charged electrode. Since then electric fields have been used to reduce combustion velocity[81], increase the flame blow-off velocity[82], regulate gas flows[83], control the formation of carbon particles[84] and more. In 1910 Thomson[85] put forward the idea that electrons played a role in combustion. While we now know electrons are predominately produced by chemi-ionization, since then the role of the electron and electric fields on flames has been debated in the literature.

The debate centres around whether the effects observed when an electric field is applied to the flame are solely due to movement of ions (ionic wind) or if the electric field is altering the flame chemistry which is responsible for the effects observed. In 1971 Jagger[86] investigated the effects of the electric field on the burning velocity of various flames. In his system Jagger operates below the breakdown voltage and passed 0.5 mA which translates to < 1 W being applied. Compared to the 10^4 W output by the flame this would mean an increase of temperature of around 1 K which could not account for the large increase in burning velocity (~65 to 78 cm s^{-1} in methane when applying 440 V cm^{-1} at 5 MHz). Instead he argues that the increase is due to electrons acquiring energy from an applied electric field which then promotes molecules and

radicals from their lowest state to their highest vibrational state. It is these species that cause an increase in reaction rate as their reaction cross section increases rapidly[87,88] with vibrational energy and thus increases the burning velocity. In 2005 Starikovskii[89] investigates the same phenomenon of burning velocities but with more detail. He reports the same increase in burning velocities (more than twice) when applying a positive voltage of 25 kV in a pulsed manner but it is important to note when applied in a direct current fashion, only slight affects are noticed. Similar to Jagger's system the applied power of the discharge is less than 1% of the burner's power and he reaches the same conclusion that electrons interact with the electric field which helps promote molecules and radicals to their highest vibrational state which in turn increases the reaction rate. Starikovskii extends this by proposing that the electric field along with free electrons, specifically excites nitrogen molecules to higher vibrational states. The excited nitrogen molecules readily transfer their vibrational energy to O_2 and as mentioned this increases its cross section leading to higher reactions rates. This is particularly important as in hydrogen and hydrocarbon flames the most important reaction is the production of the OH and O radicals as shown in Reaction 1-24[90,91].

$$H\bullet + O_2 \rightarrow OH\bullet + O\bullet$$

Reaction 1-24

Starikovskii supports this by using spectroscopic techniques to show a marked increase in OH production when a discharge is applied.

Opposing the view that electric fields are able to affect the chemistry in combustion is that the ionic wind is responsible for the observed effects. As mentioned in section 1.5 flames have an electron density between $10^9 – 10^{11}$ per cm^{-3} which corollary means an equal number of positive ions. It is these ions that experience a force when an electric field is applied and will eventually collide with neutrals as given by their mean free path. In a response to Starikovskii, Calcote attributes the effects due to the electric field bringing the flame closer to the grounded burner top.

More recently flames have been augmented by using electric discharges to create hybrid plasma jets[92–94]. Chen[95] used voltages of 180-210 V while others used high voltages up to 1 kV [96]. Bradley[38] noticed a corona forming at applied potentials of over 400 V by a current increase from µA to mA and a bright glow around the electrode.

Amplification by alternating currents have also been explored[38,97,98] and a novel way using a third electrode to act as a filament was also studied[99]. Although not used for current enhancement, flames have also been modified by pretreatment of the fuel and oxidant using plasma discharges[100,101].

In each case only one type of discharge is examined and they typically treat the system as a single unit thus do not look at the effect of the discharge on the flame. The consequence of this is that no current against voltage trace have been done in flames with the goal of producing various discharges.

1.7 Summary

This chapter has presented the fundamental principles of plasmas and flames along with the processes that occur during the creation of a Townsend or corona discharge. More importantly it has shown that these plasmas have been used and are an established field for tackling environmental pollutants. It has also shown that electric fields may be able to influence the combustion chemistry of a flame. It is hoped that by combining the two, creating a corona discharge and applying an electric field, either one or both will make a flame burn more cleanly.

1.8 Thesis outline

Chapter 2 contains a description of a platform that can sustain a flame and place electrodes accurately in the flame. Experimental automation and processing of the data obtain is also present. Chapter 3 focuses on the variety of electrodes geometries placed in a flame including a point to plane design which produces a corona. Chapter 4 examines the corona discharges produced in more detail while chapter 5 investigates the Townsend regime using mass spectrometry. Chapter 6 documents the findings when using a hydrogen flame instead.

2 Experimental platform, techniques and procedures

2.1 Introduction

This chapter contains a description of the basic experimental setup and procedures used in the following chapters. First the support platform will be described followed by the experimental techniques used. The support platform had two tasks, creating and maintaining a stable flame and a method for accurately placing electrodes in them. These electrodes then created the discharges in the flame. The primary diagnostic technique was mass spectrometry and will be discussed. Finally the procedures which included the manual operation, automation of the platform and data processing scripts will be described.

2.2 Gas supply and safety

In order to create a flame an oxidant and a fuel are needed. Oxygen (99.9% purity) acted as the oxidant and methane (99.9% purity) or hydrogen (99.9% purity) was used as a fuel. For fine control of the flame temperature and shape, an inert gas nitrogen (99.9% purity), was also used. 200 ppm and 5% sulphur dioxide balanced in nitrogen along with 5% carbon dioxide balanced in nitrogen was also available and used to calibrate the mass spectrometer. In some experiments these gases were the target to be reduced. All gas cylinders were provided by BOC.

Four Brooks digital mass flow controllers (Brooks SLA5850) were used to control each of the different gases with the inlet pressure set to one bar as required by the controllers. A pre-mixed homogenous gas mixture was created by combining all gases at a mixing chamber as illustrated in Figure 2-1.

The mixing chamber also doubled as a safety device which could vent the gases in case a high pressure built up, for example in a blow back. This was achieved by using a thin membrane plastic which would break when the system was pressurised. Other safety features were manual valves placed after the mass flow controllers which allowed the gases to be quickly shut off if necessary.

Each section was joined using compression joints and quarter inch tubing of various materials. Copper was used when an easy to work with material was needed while stainless steel was used for its resistance to corrosion and structural support. Finally polytetrafluoroethylene (PTFE) was used as a flexible but corrosion resistant material that would join parts that may need to move.

A schematic of the gas flow is shown in Figure 2-1. All joints were leak tested by applying soapy water and observing for bubbles.

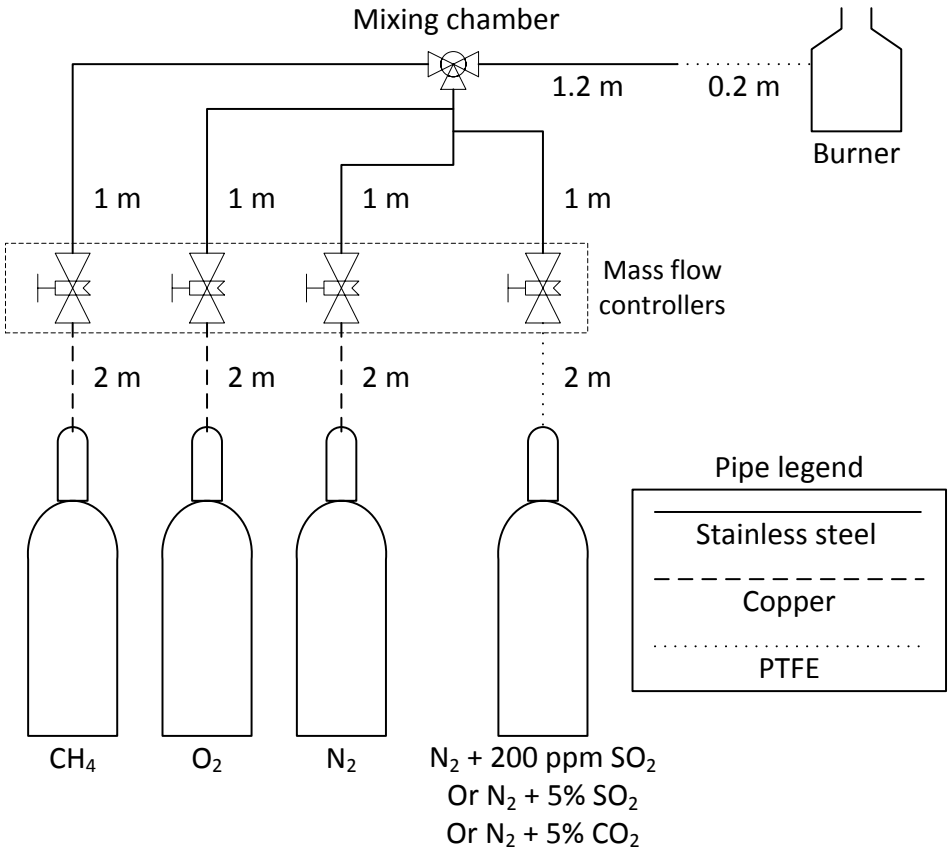

Figure 2-1: Diagram showing flow of gas used to create a premixed flame

2.3 Burner design

The work carried out required the shape of the flame to be accurately controlled. This was done by using a brass part (referred to as the brass top later) with holes that would allow premixed gases as described in section 2.2 to exit. Depending on the size, number, and orientation of the holes the shape of the flame could be controlled.

The brass top consisted of seven 0.5 mm holes arranged in a line spaced 0.5 mm apart drilled in to a 50 mm diameter, 10 mm thick brass disk. Using this top produced a flat flame. Four holes were also drilled to allow small ceramic cylindrical pillars to be placed in them. These pillars allowed electrodes to be accurately and repeatability placed on the brass top and will be explained in section 2.4.1. Figure 2-2 (a) shows a photo of the brass top.

The brass top was joined to a stainless steel support using a copper seal and 6 fixing screws. The stainless steel support was initially water cooled by a Grant (GD120) water bath (passively cooled) with deionized water for low voltage experiments. For high voltage experiments it was found that even though the water was deionized the water could act as a path way to ground through the water bath. To solve this, the stainless steel burner was water cooled by a gravity feed system. The stainless steel burner was placed on top of a piece of rubber thus fully insulating the burner top from ground.

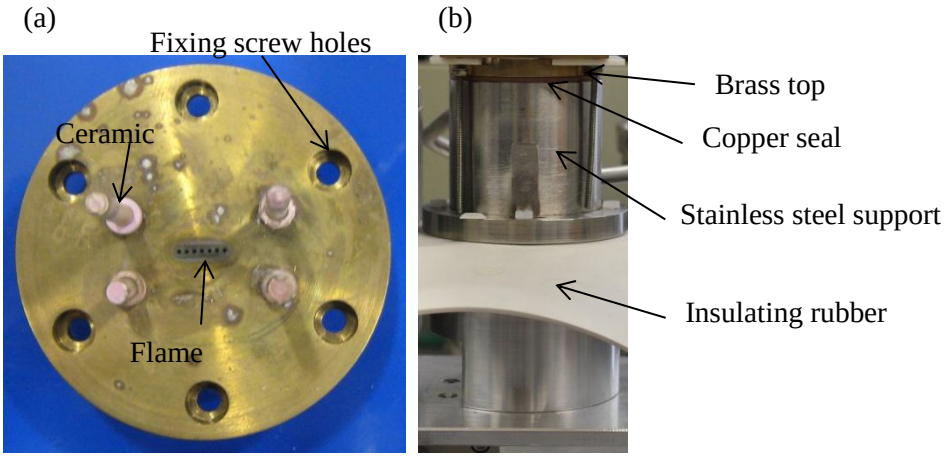

Figure 2-2: Photos showing (a) burner top design and (b) attachment to support.

2.4 Electrode placement

The next important role for the support system was the accurate placement of electrodes. For experiments using low voltages a support comprising of four ceramic pillars was used. Experiments using high voltages used a fixed plate as one electrode with a movable sharp point as another.

2.4.1 Ceramic support pillars

During the creation of the brass top as described in section 2.3 four holes were drilled as shown in Figure 2-2. The holes were 5 mm deep and allowed ceramic pillars which were typically around 30 mm tall to be placed in them. These pillars held the electrodes described in section 3.3 and 3.5 in place. This was achieved by having holes drilled in the electrodes were the pillars would fit securely. An illustration of this is shown in Figure 2-3. With this setup, electrodes that are 5 mm thick when placed using the pillars will be 3 mm apart from each other. In order to insulate the electrodes from the brass top, ceramic washers of thickness 2.8 mm were placed through the pillars. This setup allowed the electrodes to be accurately placed repeatedly without the need for positioners.

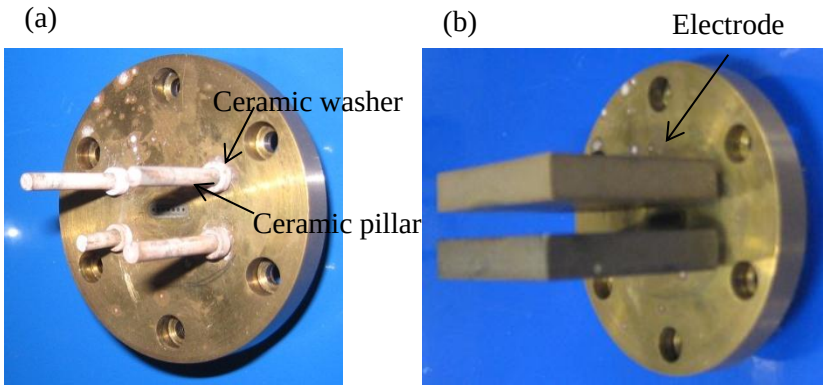

Figure 2-3: Photos showing burner top with (a) ceramic washer and pillar support for electrode placement and (b) with example electrodes placed.

2.4.2 Point and plane electrodes

While the low voltage experiments used electrodes that could be supported by ceramic pins, the high voltage experiments conducted used a configuration typically known as point to plane. In these experiments the point electrode was a sharpened platinum 1 mm wire and will be described in section 3.6, while the plane electrode a large brass electrode. In this configuration it was found that the position of the point electrode needed to be movable and placed to a high degree of accuracy, typically 10's of microns. With this in mind the point electrode was mounted and controlled by a two axis motorized micro positioner platform (Physik Instrumente M105.20P). This was done by first joining the Pt point electrode to a stainless steel rod using a copper screw

junction. This allowed the positioners to be placed further back. The stainless steel rod was then held in place by two ceramic blocks, sandwiched between two aluminium enclosures. The entire system is shown in Figure 2-4.

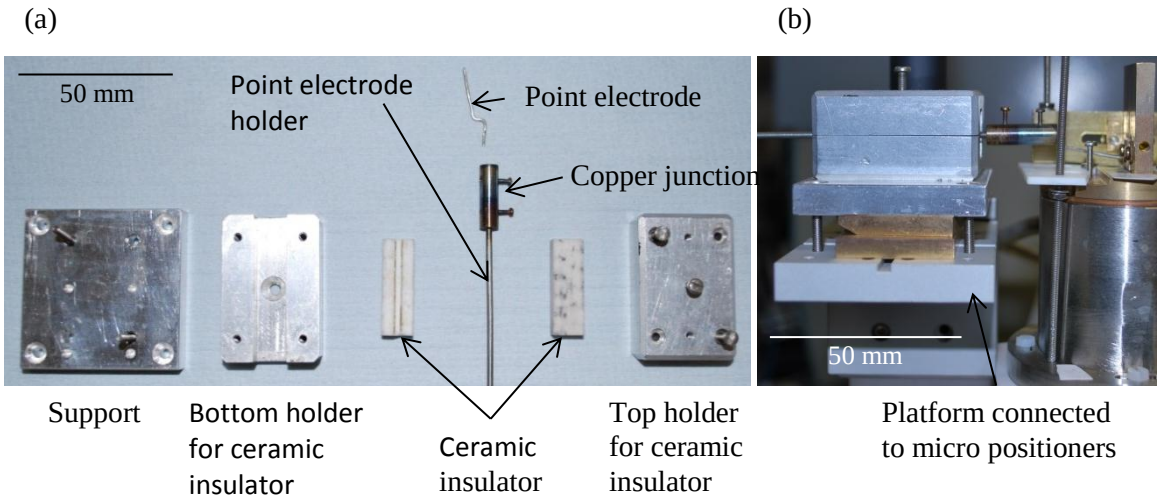

Figure 2-4: Photos showing assembly of the platinum point electrode holding mechanisms. (a) Showing a breakdown of parts. (b) Showing the assembled part.

The placement of the plane electrode on the other hand was designed such that it could be easily placed back in the same position after being taken out. To do this, a brass top as described in section 2.3 had sections recessed as shown in Figure 2-5 (a) to allow two rectangular ceramic pieces to be placed over certain parts of the brass top as seen in Figure 2-5 (b). This prevented unwanted discharges forming due to the high voltage applied. Two supporting brass blocks were then attached to these ceramic pieces that acted as support for the plane electrode as is shown in Figure 2-5 (c).

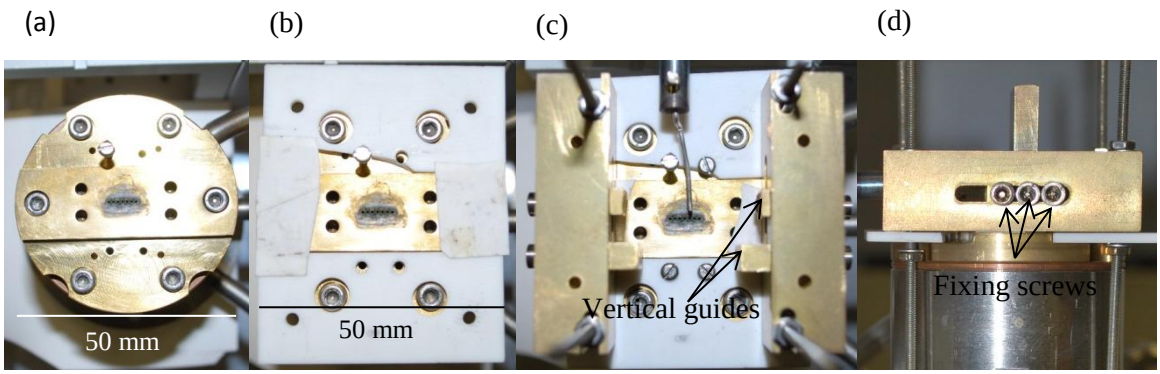

Figure 2-5: Photos showing attachment of plane electrode. (a) Showing modified brass burner top. (b) Showing ceramic pieces used to electrically insulate parts. (c) Showing brass blocks used for plane electrode positioning and support. (d) Showing fixing screws used to lock all parts in place. Outer two screws used for the vertical guides, inner for the plane electrode.

As shown in Figure 2-5(c) the brass blocks on either side have vertical guides which meant the plane electrode could only be inserted at a specific position and was unable to move. These guides were movable but had screw holes that allowed it to be locked into place. As the blocks were fastened to the ceramic pieces, which in turn were fastened to the brass top, this meant the plane electrode would always be in the same position. As an extra precaution, a screw hole was placed in the plane electrode such that the plane electrode could also be fastened to the supporting blocks as shown in Figure 2-5(d).

As the platform as shown in Figure 2-4 (b) is connected to a micro positioner (Physik Instrumente M105.20P), this allowed the point electrode to be moved to micrometre precision. In order to maintain accuracy between experiments, the distance between the point electrode and plane electrode was checked at the beginning of each experiment. This was done by moving the point electrode towards the plane electrode slowly until they were barely touching. A continuity circuit was used to determine when the two electrodes were touching and could do so to an accuracy of 1 micrometre. After this process was done the electrode would be placed at the desired distance. Using this system requires that the plane electrode can be placed repeatability to a high degree of confidence and is explained in section 3.6.1. With this system and procedure the point electrode was found to be reproducibly placed within 10 micrometres.

2.5 Mass spectrometer

The mass spectrometry system used a Hiden mass spectrometer (HAL 201). The vacuum system consisted of commercial parts and a custom built sample introduction system.

2.5.1 Vacuum system and sample inlet

The vacuum system for the mass spectrometer is shown in Figure 2-6. The rig used KF40 fittings throughout with Viton o-rings aside from connections to the rotary which used KF25 fittings.

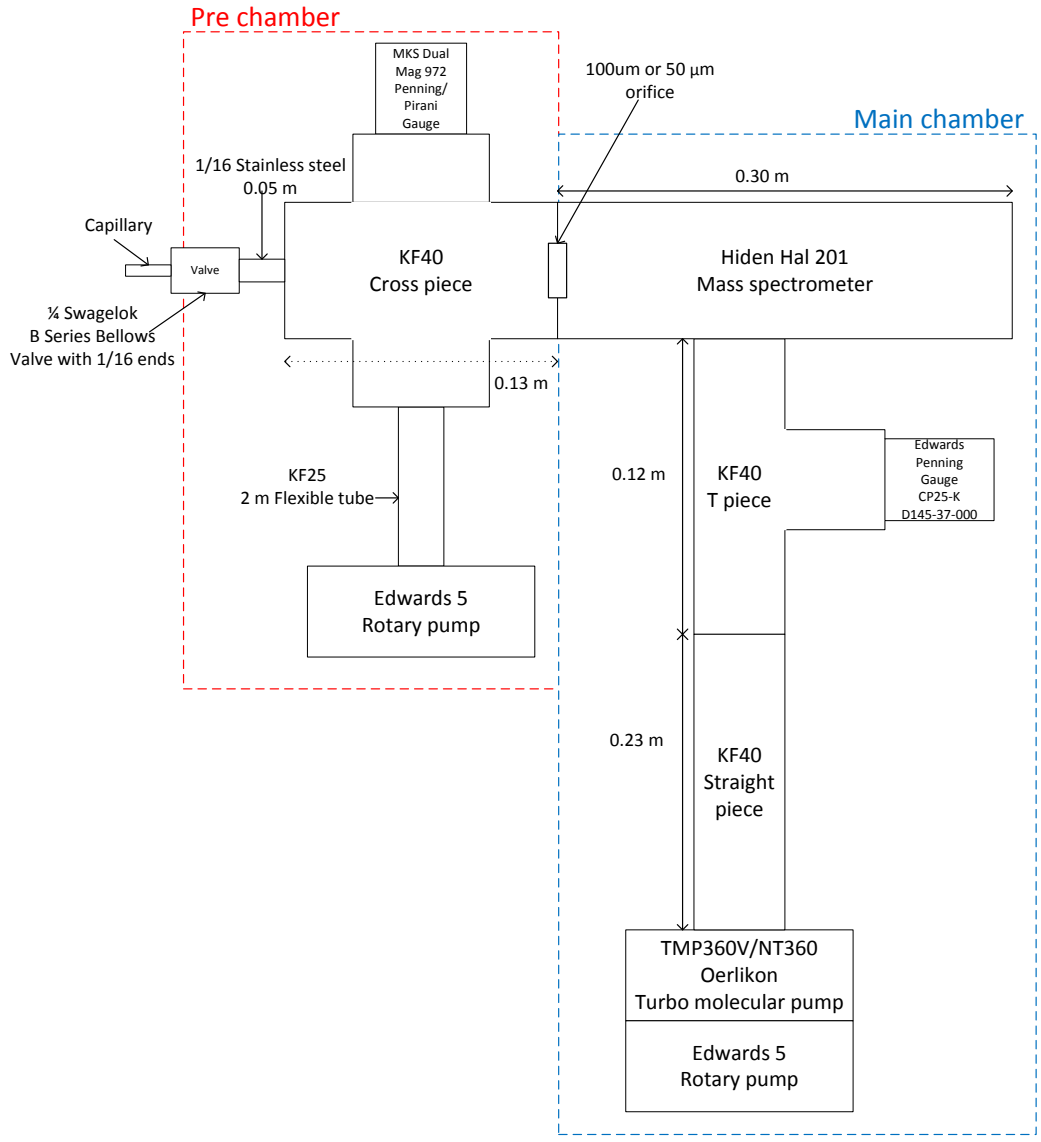

Figure 2-6: Diagram of the vacuum system used for the mass spectrometer

From Figure 2-6 it can be seen there are two main sections to the vacuum system, a pre-chamber and the main chamber. The main chamber was evacuated by a turbo molecule pump (TMP360V/NT360 Oerlikon) and backed by a rotary pump (Edwards 5). When fully sealed was able to reach pressures in the range from 2 to $4x10^{-7}$ mbar as measured by the Edwards Penning gauge. For Viton o-ring seals this is near the lowest pressures of ~10^{-8} mbar that they can seal. These low pressures were obtained by heating the main chamber to 80°C for 12 hours to ensure any residual gases on the inside surface would evaporate and be pumped out.

Although the main chamber could reach pressures in the 10^{-7} mbar range, when exposed to atmosphere through a capillary of 100 µm diameter, the pressure would reach above $8x10^{-5}$ mbar, far above operating pressure for the detectors. The pre-chamber was built to solve this by pumping away some of the sample before it reached the main chamber. An orifice separates the two chambers and was made from a brass disk 5 mm thick and 20 mm diameter. Two orifices were made, one with a hole diameter of 50 µm another with 100 µm. The holes were placed in the centre of their respective brass disk. The brass orifice used an o-ring seal against a stainless steel support which provided a good seal. When the system was sealed, the pre-chamber typically pumped down to around $5x10^{-3}$ mbar which is typical for a rotary pump. Using this setup when exposed to atmosphere through the capillary, the main chamber reached pressures of around $1x10^{-5}$ mbar, which is at the high end for the detectors. An additional ball valve was also placed before the pre-chamber to allow the sampling inlet to be changed.

The sampling inlet used to draw atmospheric pressure gas into the pre-chamber had to be chosen carefully to prevent condensation of water. The material, inner diameter, and length of the inlet were the variables that could be changed. The material chosen for the inlet was fused silica as it was inert. The length was made as short as possible to minimize the time water vapour to condense. The inner diameter however, had to be carefully balanced. An inlet too large would cause pressure in the main chamber to rise so measurements couldn't be taken, however too small would make it very easy for water to condense. Another effect of having a smaller inner diameter was that the pre-chamber would be able to reach lower pressures, thus would apply more force on the

gas which helped clear blockages. Ultimately trial and error was used to find the optimum parameters and shown in Table 2-1.

Orifice diameter in µm	Inner diameter in mm	Main chamber pressure in mbar	Pre-chamber pressure in mbar
50	0.18	$1x10^{-5}$ ± 30%	1.00 ± 2%
50	0.15	$3x10^{-6}$ ± 30%	0.42 ± 2%
50	0.10	$2x10^{-6}$ ± 30%	0.21 ± 2%
50	0.05*	$1x10^{-6}$ ± 30%	0.03 ± 2%
100	0.32	$2x10^{-4}$ ± 30%	1.33 ± 2%
100	0.28	$8x10^{-5}$ ± 30%	1.05 ± 2%
100	0.10	$2x10^{-5}$ ± 30%	0.34 ± 2%
100	0.05*	$7x10^{-6}$ ± 30%	0.06 ± 2%

Table 2-1: Showing pressures reached using 50 mm silica inlets with different diameters when exposed to air. A pirani gauge was used for the pre-chamber while a cold cathode for the main chamber as described in Figure 2-6.

By taking the ratio of the main chamber to the pre-chamber we find only around 10^{-3} % makes it through to the main chamber the rest pumped away by the pre-chamber. Using equation 2-1 a variation of the ideal gas law, we can estimate the volume intake by the system.

$$P_1V_1 = P_2V_2 \qquad \textbf{2-1}$$

$$\frac{P_1V_1}{P_2} = V_2$$

Using the values for the system above where P_1 is 50 Pa, the pressure inside the pre-chamber, V_1 is $1.3x10^{-3}$ m^3, the total volume of the pre-chamber and P_2 is 100 kPa which is atmosphere, we obtain $6x10^{-7}$ m^3 as the flow into the system. The assumptions made in this calculation are that the pumps are able to achieve steady state, the sealed chamber pressure is negligible (0.005 mbar) and the expansion is adiabatic.

2.5.2 Theory

Mass spectrometry is a technique that is able to identify unknown molecules or atoms and their relative concentrations from a sample of solid, liquid or gas. This is done by using the relationship between electric fields and charge particles. Below we will discuss the processes that take place in the Hiden Hal 201 qudrupole that was used.

Mass spectrometers can be typically divided into four parts, the sample inlet, ionizer, mass analyser and finally the detector. This project was only concerned with analysing gases which made the sample inlet simple. All that was needed was a hole and in this case a capillary was used as described in section 2.5.1.

The next section of the spectrometer is the ionizer where the sample which is typically neutral gets ionized. There are a variety of methods to create ions, however the method used by the Hal 201 is electron impact. The process of electron impact starts with a wire in this case iridium, acting as a filament which emits electrons by thermionic emission. These electrons are then accelerated using an electric field to a plate opposite the filament. This electric field can be controlled, thus enabling the amount of energy the free electrons have to be set. The sample gas flows perpendicular to the electrons flowing from the filament to plate, and as they do so they may get ionized. Ionization happens if the energy of the free electrons is greater than the ionization energy of the gas. With this in mind in principle it should be possible to selectively ionize a certain range of molecules but not others by tuning the electric field of the ionizer (also known as appearance potential mass spectrometry). For the molecules and atoms being analysed in this work, the resolution for tuning the energy of the electrons is too course. For this reason it was safer to set the energy to 70 eV thus making sure the entire sample is ionized. It is important to note that double ionization can also occur.

The next section after the ionizer is the mass analyser. As the charged molecules or atoms leave the ionizer section they each have their distinct charge to mass ratio. For example if argon with an atomic mass unit of 39.95 amu is doubly charged it will have a mass to charge ratio of 19.98 amu C^{-1}. The analyser is made of four parallel rods placed as shown in Figure 2-7 and between each of the pair, they emit a radio frequency pulse. The emitted radio frequency will cause all ions not having the mass to charge ratio it was tuned for to collide with the poles. While qudrupoles benefit from compact size they typically only have a resolution of 1 amu as is the case with the Hal 201. Higher resolution requires longer and thicker rods.

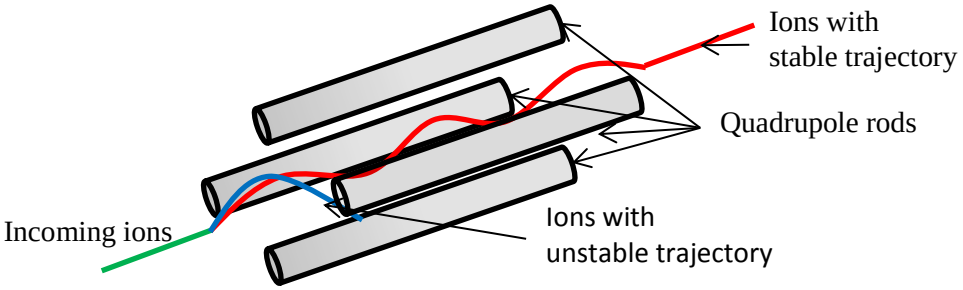

Figure 2-7: Showing an incoming beam of ions with some ions having a stable trajectory for the applied rf field and some having and unstable trajectory.

As the molecule or atom with the specified mass to charge ratio leaves the mass analyser, their trajectory is straight for the detector section. In the Hal 201 there are two detectors, a Faraday cup and a secondary electron multiplier (SEM). The Faraday cup is used to measure large partial pressures typically from 10^{-4} mbar down to 10^{-6} mbar. The detector works by allowing the charged molecules or atoms to hit a metallic surface. This transfers a small charge from the impacting particle as the particle gets neutralised. By measuring this electrical current the amount of ions impacting the surface can be calculated using equation 2-2, where N is the number of ions observed in a time t, I the current measured and e the charge of an electron.

$$\frac{N}{t} = \frac{I}{e} \qquad \textbf{2-2}$$

As it can be seen from equation 2-2 as the number of ions observed gets smaller so does the current measured. To compensate for this when the Faraday detector needs to observe very low partial pressures of incoming particles (<10^{-6} mbar), the detector must wait for some time till a current becomes large enough. This is what sets the usable limit of Faraday detectors as although they can be used at partial pressures less than 10^{-6} mbar the time per measurement (dwell time) may be unfeasible. For the Hal 201 the faraday detector can take readings at a rate of one every 15 ms for partial pressure from 10^{-6} mbar upwards, however at 10^{-7} mbar the time taken jumps to 100 ms and for 10^{-8} mbar it takes 300 ms.

The second detector, the SEM, allows the qudrupole to take partial pressure readings from the ranges of 10^{-7} mbar down to 10^{-13} mbar with reasonable sample rates. The SEM works by using a special material designed to generate electrons on impact from an electron. The geometry of the SEM is designed such that each electron generated is

aimed at another surface of the multiplier. This continues causing a cascading effect which allows the initial signal of a small number electrons to be amplified greatly. The electrons are accelerated by an electric field which can be used to control the amplification with gains as high as 10^3. Like the faraday, the SEM has partial pressure ranges that can be taken quickly. For the Hal 201 this was 15 - 31 ms for pressures from 10^{-7} - 10^{-9} mbar, but for pressure at 10^{-10} and 10^{-11} mbar was 310 and 1850 ms respectively.

One disadvantage of using the SEM is the surface is consumed during measurements and is relatively expensive to replace. The higher the partial pressure of the species being measured the faster the detector is consumed. In order to preserve the detector, partial pressures greater than 10^{-6} mbar will cause the spectrometer to stop taking measurements on the SEM. Another side effect of the surface being consumed is a decrease in sensitivity over time which must be compensated by applying higher electric fields. Because of these factors obtaining absolute partial pressures can be tricky as calibration needs to be done over time. If measurements are taken at the upper limit of the SEM, care must be taken to insure the spectrometer does not stop. Due to using two detectors for different ranges, the quadrupole is incapable of sampling a species whose concentration changes over the range of 10^{-6} to 10^{-7} mbar optimally.

2.5.3 Background mass spectrum of sealed vacuum chamber

A mass spectrum of the empty chamber is shown in Figure 2-8 (experimental data points) to demonstrate the baseline partial pressures that would typically be present in any experiment. The detection range was typically set to 10^{-9} Torr range though the spectrometer does return values for pressures below this range. This can be seen in Figure 2-8 as the range was set to 10^{-9} Torr and there are many masses at around $2x10^{-10}$ Torr with large error bars. In communication with Hiden, they explain the reason for these masses showing is that data processing is used to extract a signal from the background noise produced by the analogue detectors. In particular a value is given for this noise value and even if there are no species, due to random error a signal can be generated. The effect of this is the spectrometer will respond with values that can sometimes be negative. This is what produces the large error bars. The result of this is

that masses with a partial pressure below $1x10^{-9}$ Torr will be ignored although in theory masses with pressure of $5\text{-}9x10^{-10}$ Torr could be used.

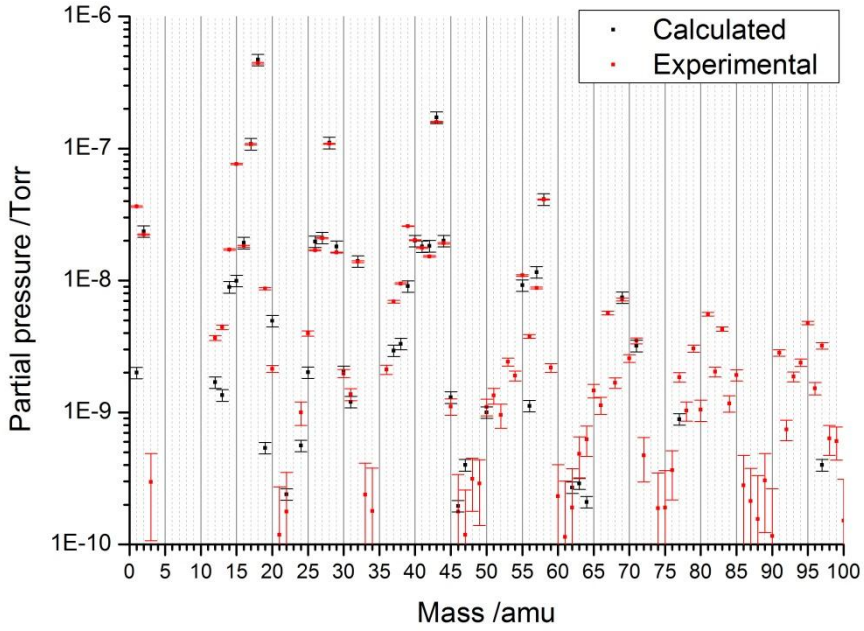

Figure 2-8: Experimental mass spectrum from 1 – 100 amu of the vacuum system when sealed off and calculated spectrum using multiplier from Table 2-2, and fragmentation patterns from Table A-1 (a). Each experimental point is an average of 50 scans and error bars shown as 1 standard deviation. The scans were taken on the faraday detector set to auto range to 10^{-9} Torr. Experimental error bars are ±10% of calculated value.

While it is possible to analyse Figure 2-8 by looking at each individual peak and understanding them, the spectrum will be taken as a whole and used to deduce what species are present and in what amounts. To do this we will first make an assumption about what species are present and their concentrations. Then using linear combination along with their fragmentation pattern a theoretical mass spectrum can be created. This spectrum can be compared to the experimental data to determine if our initial assumption about what species and their concentration are present is correct, Table 2-2 shows the result of this analysis.

Species	Multiplier x10^{-9} ±10%	Calibrated multiplier	Percentage of total gas measured
H_2O	4.7	5.22	65±7
CO_2	0.2	0.14	1.8±0.2
N_2	1	1.00	12±1
O_2	0.14	0.16	2.0±0.2
NO	0.02	0.02	0.21±0.02
Ar	0.2	0.17	2.1±0.2
CH_4	0.1	0.06	0.78±0.08
C_3H_6O	1.4	0.39	4.9±0.5
H_2	0.2	0.45	5.7±0.6
C_4H_{10}	0.25	0.05	0.64±0.06
C_2H_2	0.1	0.10	1.3±0.1
C_2H_6O	0.008	0.00	0.03±0.003
C_3H_7OH	0.007	0.01	0.09±0.09
DP oil Fomblin	0.05	0.05	0.63±0.06
DP oil ppe	0.01	0.01	0.13±0.01
MP oil	0.03	0.03	0.38±0.04
Rotary pump oil	0.05	0.05	0.63±0.06
Turbo pump oil	0.05	0.05	0.63±0.06

Table 2-2 Multiplier used along with Table A-1 to produce calculated values in Figure 2-8. The respective calibrated amounts using Table A-2 are also shown. The error shown was calculated using an assumption of ±10% in the relative sensitivity in Table A-2.

It is important to note the mass spectrometer was not calibrated and thus the fragmentation pattern, intensity and relative sensitivity have an associated error. Hiden suggests the fragmentation intensity could have an error around ±10% and this can also apply to the pattern observed. For example in Table A-1 the fragmentation pattern for acetone reported by NIST contains many more fragments than the Hiden library and these extra fragments may or may not actually appear during experiments. For consistency Figure 2-8 was generated only using the fragmentation pattern given by the Hiden library. The relative sensitivity values from Table A-2 used to produce Table 2-2 were also from the same library and Hiden suggested a 10% error on these values as well.

From Figure 2-8 it is clear the fit using Table 2-2 is good however there are several masses where the experimental values differ by a large amount from the calculated values even factoring the errors. The first mass that shows this is mass 1. The experimental value is far higher than the calculated value and can be attributed to the tail end of a large transmission peak. Masses 13 – 15 and 36 - 39 can be explained due to acetone. From Table A-1 it can be seen several fragments appear on the NIST library but not the Hiden library and for the masses that show a lower calculated value, the

Nist shows the intensity of these fragments to be much higher. Hiden suggests mass 19 could be fluorine being out gassed from the stainless steel metal the source is made from. Another explanation is although the mass spectrometer has a 1 amu resolution, mass 18 has a very high intensity and part of the intensity of mass 19 could be due to the tail end of this large peak. Mass 20 shows a higher calculated pressure and the reason for this is currently unknown. This leaves masses 12, 24, 25 and many above 50 amu. For the masses above 50 amu, these are most likely due to large hydrocarbons from the variety of oils in the turbo and rotary pumps. Table 2-2 already shows 5 different types of oils. One source of these oils can be explained by Figure 2-6 describing the vacuum system. It can be seen the pre-chamber is attached to the main chamber by a small orifice. As the main chamber is at a much lower pressure (10^{-7} Torr) compared to the pre-chamber (10^{-3} Torr), oil from the rotary pump backing the pre-chamber can be pumped into the main chamber. Another indication is the partial pressures for these masses are small, which would give <1% of the total gas and their masses are typical for large hydrocarbons. From this it is possible masses 12, 24 and 25 are fragments of these large hydrocarbons.

From Table 2-2 it can be seen the chamber atmosphere consist mostly of water (65%) and is as expected. Water is hard to pump away as it sticks to the surface of the vacuum system. Nitrogen is the next largest gas measured and is likely due to air being drawn in from outside. It is important to note that the percentage of water is much larger than nitrogen and this indicates the system is sealed well. Hydrogen is an unexpected gas to be detected in a sealed chamber however can be explained as it was used in previous experiments. Due to its size hydrogen can be absorbed into metals, and it is likely the filament in the mass spectrometer is heating the metal the source is made from causing trapped hydrogen to be out gassed. Acetone is also observed in the same amounts and can be expected as it was the solvent used to clean the vacuum parts when being taken apart. Carbon dioxide, oxygen and argon are all present in about the same quantities. One possible source for this is the air however the ratio of nitrogen to them doesn't support this. Finally there are many small organic molecules such as methane, butane, acetylene, Isopropyl alcohol and ethanol which total <3%. While it is possible they are all present in the chamber, another explanation is that these are fragments from larger organic molecules present such as pump oil. Lastly pump oils are also present with <3% of the volume.

For the range from 1 – 50 amu, each mass can be modelled reasonably well. Species which give a response above 10^{-8} Torr can be easily distinguished and identified with good confidence using this analysis. When exposed to atmospheric pressure the main chamber typically reaches 10^{-6} Torr. This means species that change ~0.1% of the total volume can be expected to be detected and identified. Systematic drift of the background over time is accounted for as control spectrums are taken for every change in variable and is discussed in section 2.8 and 2.9.

2.6 Electrical devices

Most of the experiments conducted required fine control over either the voltage or current being applied. To do this various power supplies were used. For lower voltages a potentiostat Eco stat 101 was used or the analogue output from a National instruments PXI-6259. For high voltages an ETPS Limited, 0-5 kV, 0-12 mA, negatively polarised to ground (Part number EPN 50 126 24 5) power supply was used. Powering this high voltage power supply was a Mason EP 613 set at 24 V. Control of the high voltage power supply was done using the analogue output from a PXI-6259.

2.6.1 High voltage polarity switcher

To help automate the experiments being conducted a custom high voltage polarity switcher was built. This was needed as the high voltage power supply as mentioned in section 2.6 was only capable of outputting a negative voltage with respect to ground. As the systems being used only contained two floating electrodes, the polarity could be reversed by swapping the wires. For example “polarising” an electrode positively could be achieved by polarising the other electrode negative, while keeping the electrode being investigated grounded. It should be noted, that the electrode wasn’t actually polarised positive but because the system is floating, would act like it was.

The polarity switching device was made using two Pickering Electronics 66-1-C5/1 dry reed relay units (rated to 7.5 kV, 50 W), each contained two relays each. Each unit operated with a 3-4 ms delay between switching both relays. This action mimics a form C type relay (connected, disconnected, reconnect) which is essential when dealing with high voltages. The two units were held and soldered on to a large veroboard. To ensure

no arcing occurred, any track that could have a high voltage signal running through them were isolated. This was done by stripping the copper from the nearest two tracks around the high voltage track. The relays were controlled by a digital output from the PXI-6259 as mentioned in section 2.6. A schematic of the device is shown in Figure 2-9.

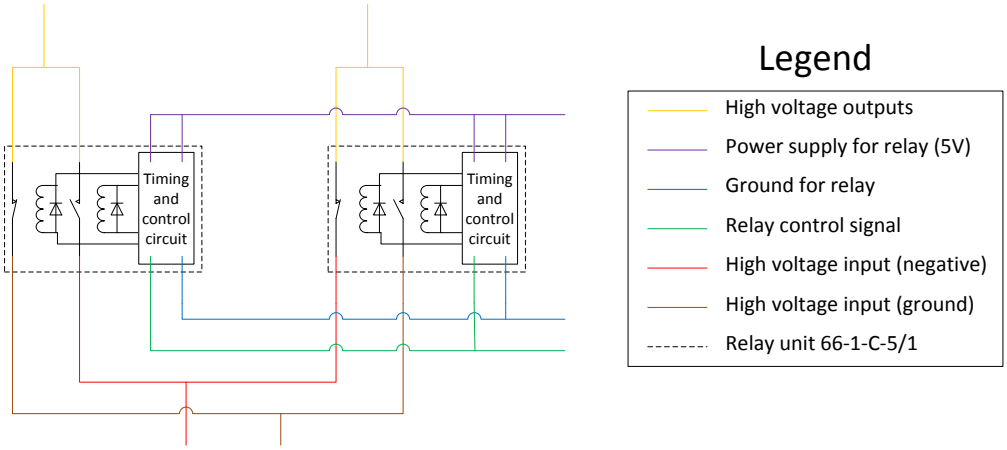

Figure 2-9: Circuit diagram for high voltage polarity switcher using Pickering Electronics relay 66-1-C-5/1.

2.7 General procedures for turning on and off the flame

In order to obtain a flame at a desired flame ratio often a number of steps must be taken before reaching the desired ratio. This is particularly true for near stoichiometric ratios which have the highest flame velocity. When lighting a premix gas containing a fuel and oxidant there is a risk of a flash back. This happens when the velocity of the flame going in the direction opposite of the un-burnt gas is greater than the flow of premixed gas coming out of the burner. The flame front then has a chance to go into the pipes where a large pressure can build up due to combustion and a flashback is created. There is a chance that a flashback won't occur even if the velocity of the flame is greater than the flow, if the holes of the burner are small enough to cause the flame to quench. This occurs as the hole constricts the flow enough such that the velocity of the flame is slowed enough. With the systems used, flash backs can occur and with this in mind several safety rules have been devised. It is advised to always light the flame with the safest mixture. This will mean starting with either a very fuel rich or very oxygen rich mixture and keeping the inert gas as low as possible. As the ratio is adjusted towards more hazardous ratios (stoichiometric) the inert gas should be added

as this will increase the flow of the premixed gas coming out the burner. A good rule is the total flow should always increase when changing from one mixture to another.

While there is always a risk of a flash back which would extinguish the flame, changing ratios to quickly can also extinguish the flame. For the experimental setup used, the flame is much smaller compared to the electrodes that surround. The electrodes are excellent heat conductors and changing the ratios to quickly can quench the flame. This occurs as the electrode can absorb a lot of the heat causing the flame to be unstable and blow out. The procedure used for lighting a flame to the desired flow rates of 150/300/350 ml.min^{-1} for $CH_4/O_2/N_2$ respectively is as follows:

- For each step wait at least 10 seconds before changing to the next
- Light the gas mixture with flow of 300/100 ml min^{-1} for CH_4/N_2
- Change flow to 300/150/100 ml min^{-1} for $CH_4/O_2/N_2$
- Change flow to 250/200/100 ml min^{-1} for $CH_4/O_2/N_2$
- Change flow to 200/250/150 ml min^{-1} for $CH_4/O_2/N_2$
- Change flow to 200/250/200 ml min^{-1} for $CH_4/O_2/N_2$
- Change flow to 150/300/300 ml min^{-1} for $CH_4/O_2/N_2$
- Change flow to 150/300/350 ml min^{-1} for $CH_4/O_2/N_2$

While turning on the flame can be problematic, turning off the flame is much simpler. A large gust of air is all that is required to blow out the small flame. It is important to quickly turn off the flow of premixed gases after the flame has been extinguished.

2.8 Automation control

From the previous sections a computer was necessary to interact with various parts of the support platform. These were four outputs which corresponded to controlling the mass flow controller using Brooks software, motorized positioners using PI's motion control, the mass spectrometer using MASoft and the high voltage power supply using national instrument signal express. With this in mind code was written to integrate all these devices into a single program. The aim of this program would be to be as flexible as possible while allowing the experiment to be conducted through automation.

One of the outputs was a National Instruments data acquisition card (PXI-6259) which controlled all of the electronics. These included a power supply and polarity switching

unity as described in section 2.6 which allowed the amount of current and voltage applied between the electrodes to be controlled and recorded. The data acquisition card also controlled an LED which was used to synchronise a video camera while the data was being collected at the computer. This was done by flashing the LED which was in focused by the camera at specific steps. When watching the video footage after, this was used to work out which step each frame corresponded to. Controlling the power supply, polarity switching unit and LED required three digital out and two analogue out ports. The data produced by the power supply required two analogue input ports.

The next output controlled were the electrode positioners as explored in section 2.4.2 and was done using PI's provided drivers. The mass flow controller in section 2.2 was controlled by using Brooks software and manipulating the values of the software through the system clipboard (Brooks suggested this implementation). Finally the mass spectrometer was also integrated into the program. The mass spectrometer was more involved than the other devices as it contained two detectors which needed to be used for different mass ranges. For example when scanning masses 18, 28, 32 and 44, typical the faraday detector should be used as explained in section 2.5. As the mass spectrometer sample rate was the slowest out of all the devices care needed to be taken to ensure enough samples were taken.

Labview was chosen as the programming language as it provided the minimum coding time. This was primarily due to available drivers for all the devices that needed to be operated. The method for implementing all the devices was to write a program that would take input from a comma separated file, and at each line the program would translate what the various devices connected to the computer needed to do, while simultaneously recording all the data obtained. At each step in the file the experimenter specifies the value each device should be outputting. As mentioned the mass spectrometer sample rate was the slowest and ensuring enough samples were taken per step had to be programmed in. However not all steps needed this feature, for example moving an electrode. To solve this at each step the experimenter can choose how many samples the mass spectrometer must take before continuing to the next step or choose how long each step must last for. These two options allowed enough flexibility to run most experiments. Table 2-3 is an example of a comma separated control file used and Table 2-4 explains the use for each column.

Step	Label	Filename	Time or scan	Time in sec	Masses	Cycles	Detector	Current %of 12mA	Voltage % of 5kV	HV On	…
0	0.1	0	0	0	04:04	0	Faraday	0	0	0	…
1	0.1	0	1	0	01:20	10	Faraday	0	0	0	…
2	0.1	0	0	3	04:04	10	Faraday	0	0	0	…
3	1.1	1	1	0	28:28;44:44	50	Faraday	0	0	0	…
4	1.1	1	0	5	28:28;44:44	10	Faraday	4.17	2.5	1	…
5	1.1	1	1	0	28:28;44:44	50	Faraday	4.17	2.5	1	…
6	1.1	1	0	5	28:28;44:44	10	Faraday	0	0	0	…
7	1.1	1	1	0	28:28;44:44	50	Faraday	0	0	0	…

…	Polarity	O2	CH4	N2	H2	Leak	x	z	Digital out	Caption
…	0	6.2	2.8	2	*	25	1.9	2.4	0	zero step
…	0	6.2	2.8	2	*	25	1.9	2.4	0	warm up the detector
…	0	6.2	2.8	2	*	25	1.9	2.4	0	wait 3 sec
…	0	6.2	2.8	2	*	25	1.9	2.4	0	take faraday data when power supply is off
…	1	6.2	2.8	2	*	25	1.9	2.4	1	turn power supply on, turn on LED and wait 3 sec
…	1	6.2	2.8	2	*	25	1.9	2.4	0	take faraday data when power supply is on and turn off LED
…	0	6.2	2.8	2	*	25	1.9	2.4	0	turn power supply off and wait 3 sec
…	0	6.2	2.8	2	*	25	1.9	2.4	0	take faraday data when power supply is off

Table 2-3: Showing an example CSV file used to conduct an experiment.

Column label	Description
Step	Used to quickly know which step the experiment is at.
Label	Used to label data
Filename	Used to specify what the filename the data obtained from the step will be.
Time or scan	Used to choose whether steps are controlled by time, value of 0 or number of samples taken by the mass spectrometer, value of 1.
Time in sec	Time in seconds for each step if Time or scan column value is 0.
Masses	Masses that will be scanned. Masses range are separated by a colon (:) and ranges are separated by a semi colon (;). For example 1:27;29:31 will scan masses 1 amu to 27 amu and will also scan masses 29 amu to 31 amu.
Cycles	Number of samples mass spectrometer needs to take before moving to the next step if Time or scan column value is 1.
Detector	Detector the mass spectrometer will use. Values are Faraday or SEM.
Current %of 12mA	Current that will be applied. Value of 5 means 12 mA will be applied.
Voltage % of 5kV	Voltage that will be applied. Value of 5 means 5 kV will be applied.
HV On	Safety value so power supply is only turned on when this value is 1.
Polarity	Setting a value of 1 makes the output positive, a value of 0 negative.
O2	Flow rate of gases that will be set as a percentage of 5000 $ml.min^{-1}$ for oxygen, methane and nitrogen, 1000 $ml.min^{-1}$ for leak. For example a value of 50 will output 2500 $ml.min^{-1}$ for oxygen, methane or nitrogen. The leak gas was either 200 ppm SO_2 or 5% CO_2 balanced in N_2. A value of * will disable the flow controller.
CH4	
N2	
H2	
Leak	
x	Used for positioning x axis
z	Used for positioning z axis
Digital Out	Used to turn on LED used for camera synchronisation.
Caption	Used for conveniences to know what the steps' function is.

Table 2-4: Explaining column titles used in Table 2-3.

It should be noted that while the feature for selecting whether to set the mass spectrometer to scan a certain number of samples or scan for a number of seconds before going to the next step was programmed in, the feature was not used. Due to being over cautious and turning the mass spectrometer filament on only when readings were being taken caused large systematic errors. This arose due to the main chamber heating up and cooling down which caused pressure changes to be observed. Instead the mass spectrometer was left continually scanning.

With the control file and the support platform, experiments can be conducted mostly automatically. The experimenter only needs to create the comma separated control file, place the electrodes and position the sampling inlet and the rest of the experiment will take place automatically. Figure 2-10 shows a flow diagram with all the devices that are controlled and the steps an experimenter does when running an experiment. It should be noted that while the flame could be automatically ignited by controlling the gases and creating a spark with the power supply, for safety reasons both the lighting and extinguishing of the flame was done manually.

Automation of the experimental procedure along with the flexibility of using a control file had several key advantages. Primarily it allowed for complex experiments involving multiple variables to be explored during one experiment, such as different voltages and currents applied while sampling the entire range of the mass spectrometer. Although these experiments in theory could have been done manually, the time taken would be much longer due to the human interaction and more importantly the risk of making a mistake increases over time. Automation also helped improve confidence in the data by allowing repeats to be done at the end of every experiment therefore proving time effects such as materials heating up were not the cause of the changes observed. An example of a simple experiment would be applying a voltage ramp of around 10 – 20 different voltages while taking a baseline (control) between each applied voltage. More complex experiments involved changing the gas composition while also preforming a voltage ramp, all while taking mass spectrometry measurements.

One of the objectives for using automation was to take advantage of the statistical field of experimental design. In particular this would include full randomization to further remove experimental bias, selective replication to reduce experimental uncertainty and the factorial experimental paradigm to rapidly explore different factors. An example of such an experiment would be to test the factors, spatial dependence (both x and z), current and voltage applied on the change in gas partial pressures for masses 1 to 200 amu as observed by a mass spectrometer. Such an experiment done randomly with selective repeats would be nearly impossible for a human to do without mistakes. Although in the end the project didn't use all the tools from experimental design, the automation platform was capable of carrying out such experiments.

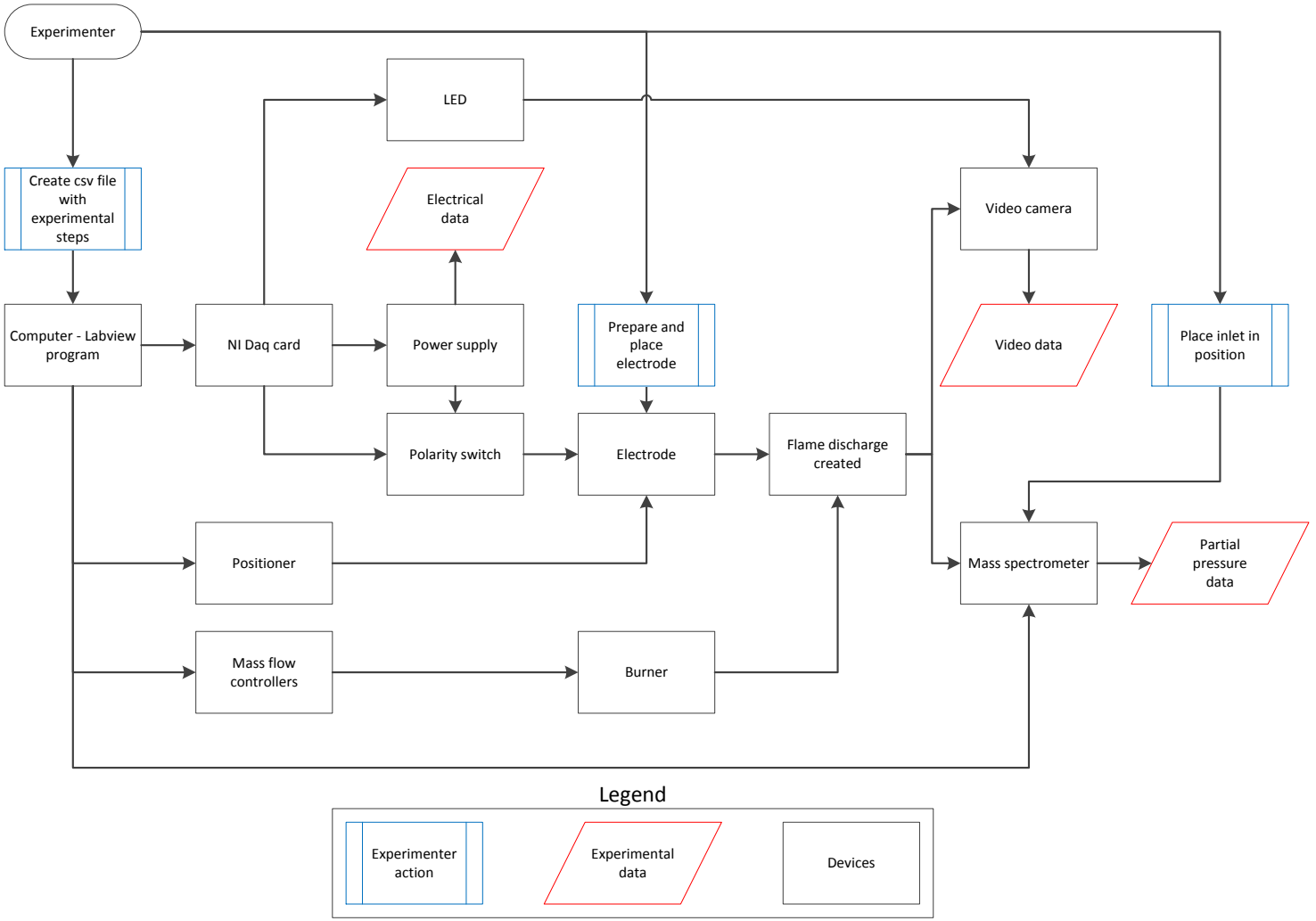

Figure 2-10: Flow chart showing the equipment used to conduct an experiment and how they were controlled.

2.9 Processing raw data

While automation played a large role in the experimental procedure, it was not useful by itself. In order to take full advantage of the large quantity of data produced by the automated procedures, processing of raw data had to be automated as well. It was important that the data from one experiment should not take such a long time to analyse as although one experiment could answer several questions at a time, there was no way of knowing if this was the case or if the experiment was flawed, for example a device not being turned on.

The processing was done in the statistical programming language R. R provided the flexibility of a fully fledge programming language while having graphing capabilities and a large number of packages to allow for rapid development. Several attempts were made at creating a general purpose script that could handle all experimental output however as the complexities quickly rose, processing scripts were created by using a base template followed by tweaks for the particular experiment. While this was not ideal it proved to be the most time efficient. Processing of the raw data could be broken down to the following steps:

1. Synchronise all the devices (cameras, mass spectrometer, etc) to a common time source.
2. For each of the different conditions, find the mean and standard deviation of all the data points for that condition from all devices. For example if one of the conditions was applying 100 V, find all the data obtained during when 100 V was applied and calculate the means and standard deviations.
3. In order to compensate for systematic errors a control also known as a baseline was often taken. An equation would then be fitted to this baseline so points could be interpolated where needed.
4. The raw data was divided by the equation found in step 3 to find a normalised ratio. Error propagation for this step was also carried out.
5. Another value that was calculated was done by subtracting the baseline from the raw data to find an absolute value; again error propagation was also carried out for this step.

6. Steps 3 to 5 was carried out for each variable such as voltage, current, partial pressure readings for masses sampled, as each variable had its own associated systematic error.
7. Graphs were plotted for all variables (voltage, current, partial pressure readings).
8. Finally a single table with all the averages and errors were outputted.

The graphs from a typical script for a small experiment using the above steps will be shown. The following example will follow an experiment that examined 12 different conditions, for comparison some experiments conducted contained 81 different conditions. In this example three different gas ratios where used while applying four different voltages (the base line of zero applied volts was considered as one) for a total of the 12 different conditions. Partial pressure of masses with 10 amu through to 50 amu where taken along with current and voltage measurements. Only one mass (44 amu) will be shown from the range of 40 masses taken.

Figure 2-11 shows the raw data obtained for the experiment described above. Figure 2-12 shows the result of step 2 and step 3. The result of step 4 is shown in Figure 2-13 and step 5 in Figure 2-14. Graphs of partial pressures for masses with 10 – 50 amu were also produced and finally Table 2-5 was produced for the normalised data and a similar one for the absolute data. It was important to graph each step of the script as it allowed the steps to be checked visually to ensure changes were real and not from poor systematic error modelling from step 3.

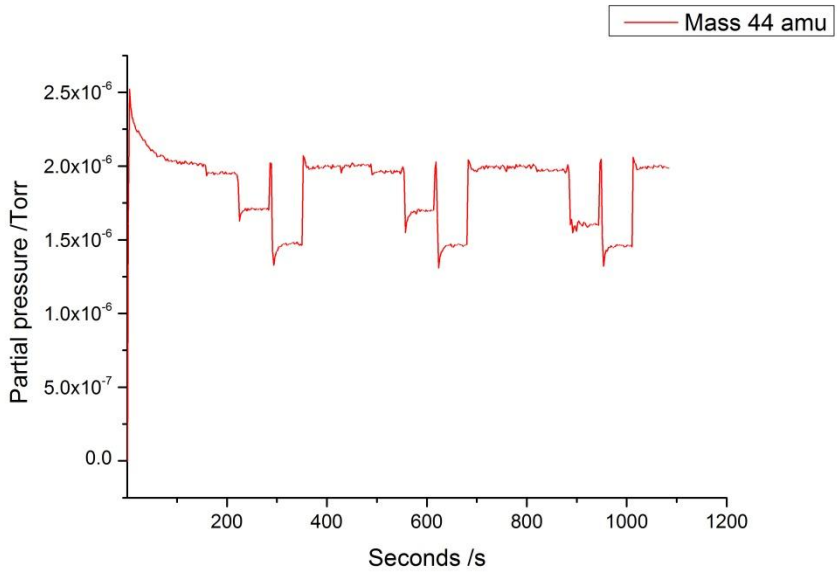

Figure 2-11: Graph showing raw data of a single mass (44 amu) direct from mass spectrometer from the start of the experiment.

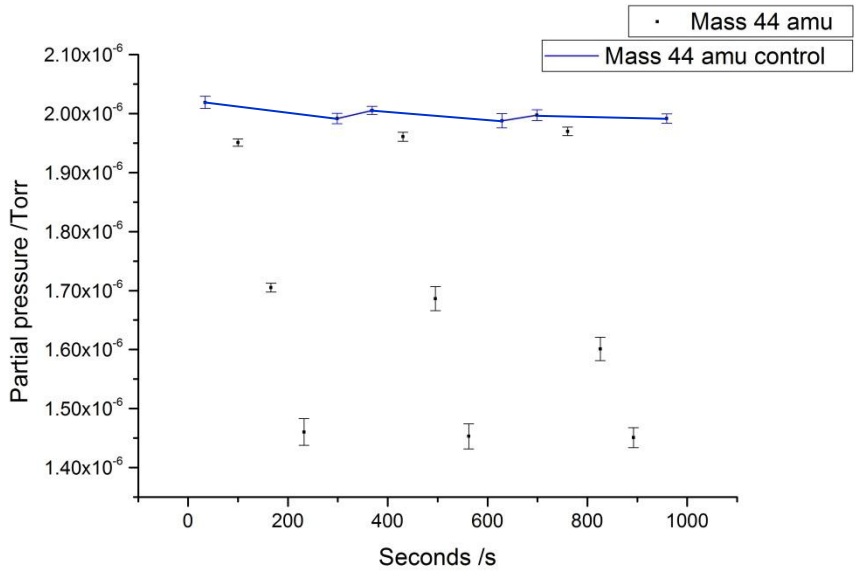

Figure 2-12: Graph showing the result from applying steps 1 and 2 to obtain processed raw data. First data from Figure 2-11 is synchronised with other devices and re-zeroed accordingly, then averages and error bars are calculated. The blue line indicates the control value.

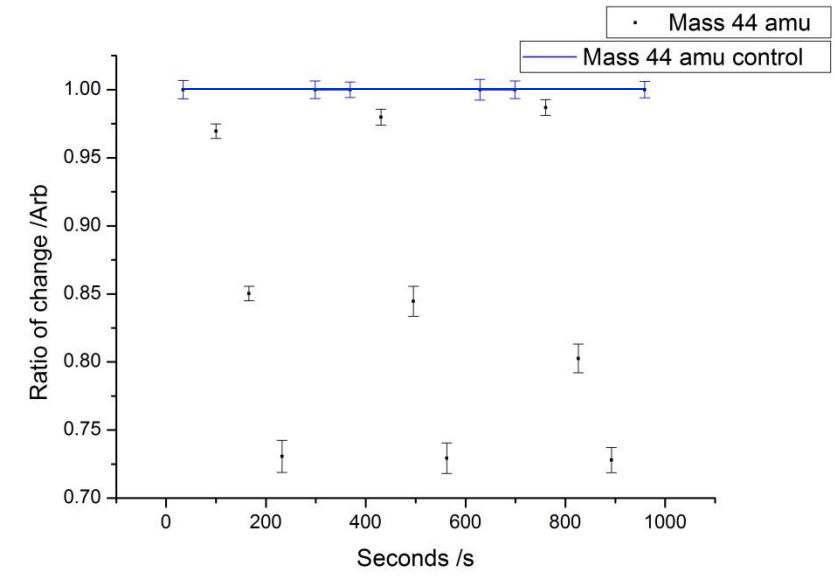

Figure 2-13: Graph showing normalised data by applying step 4. This was done by taking values from Figure 2-12 and dividing by the blue control line and propagating errors.

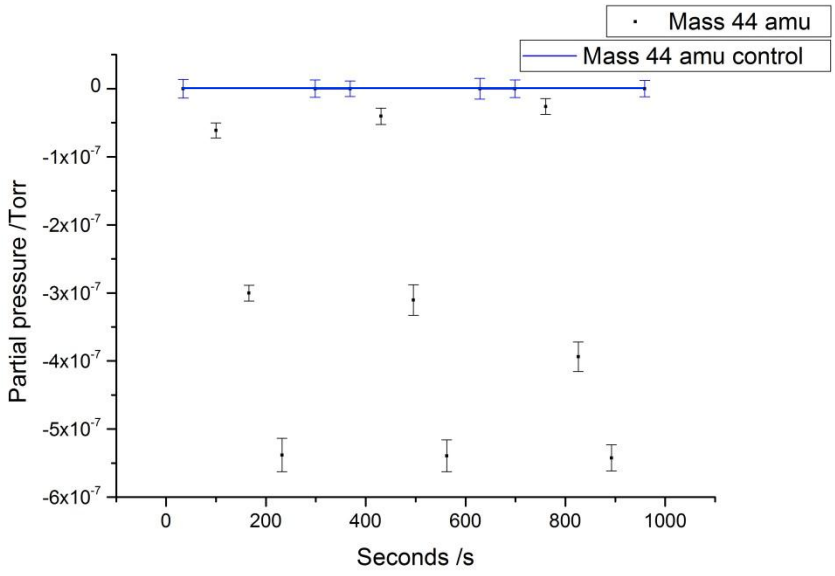

Figure 2-14: Graph showing the absolute difference between control line and data points as in step 5. This was done by taking values from Figure 2-12 and subtracting them from the blue control line and propagating errors.

Caption	Time	Current	Cur SD	Voltage	Volt SD	Mean10	…	Mean44	…
0	34.18	0.00	0	0.00	0	1.00	…	1.00	…
1500	100.00	0.01	0	1.50	0	0.64	…	0.97	…
2000	166.00	0.01	0	2.00	0	0.43	…	0.85	…
2500	232.32	0.02	0	2.50	0	1.28	…	0.73	…
…	…	…	…	…	…	…	…	…	…

…	Mean50	SD10	…	SD44	…	SD50
…	1.00	2.11	…	0.01	…	0.15
…	0.94	2.23	…	0.01	…	0.15
…	0.97	2.10	…	0.01	…	0.08
…	0.99	3.41	…	0.01	…	0.08
…	…	…	…	…	…	…

Table 2-5: Subsection of table for normalised data

As mentioned it was hoped that the automation system would take advantage of the field of experimental design, so the processing was also design to accommodate this. Two of the key features, randomization and selective repeats would have proven difficult to analyse manually. To tackle this, the database concept of a primary key was used. In the system developed the control file acted as both a file to control the experiment and a table that showed what conditions had been applied. Within the control file was a column called label. This column along with the date and time the experiment was conducted, had the purpose of being a primary key. As long as only one experiment was started per second, the labelling provided a unique identifier.

Using this identifier and the control file would have allowed randomized data to be untangled and repeats treated properly. Although not all the tools from experimental design were used, it was important that these concerns were addressed at the time of creation as it would have been prohibitively time consuming to analyse the data if they were used.

2.10 Summary

With the setup documented in this chapter a stable premixed flame can be created with electrodes that can be placed with micrometre accuracy. A quadrupole mass spectrometry system that will be used has also been documented. Finally a method for conducting automated experiments along with a procedure to processes the data obtained has been shown.

3 Development of electrode geometries

3.1 Introduction

Numerous electrode designs were tried in an attempt to manipulate the exhaust gases of a flame. Four different designs are described, three of which were used in combination with low voltages (<200 V) in an attempt to drive redox reactions using electrochemistry. These three designs were 1) an arrangement of two flat blocks, 2) using layers of meshes to increase surface area, 3) interdigitating tungsten pins to maximise surface area. The last design was a platinum shaped point(<1 mm diameter) that mimicked the standard point to plane electrode configuration of corona plasmas and the design that will be used in later chapters.

3.2 Minimum electrolysis current needed for detection

By using Faraday's law of electrolysis, and the detection limit of the mass spectrometer, a rough estimation of the amount of current needed to be applied so detection can occur. From section 2.5.2 regarding the detectors of the mass spectrometer, we found that the optimal range is from 10^{-6} to 10^{-9} Torr which is 3 orders of magnitude. By using $6x10^{-7}$ m^3 s^{-1} as calculated in section 2.5.1 entering the pre-chamber we find at least $6x10^{-10}$ m^3 s^{-1} needs to be converted to be detected. Using the molar volume of an ideal gas this is $3x10^{-8}$ mol s^{-1}. By using Faraday's law described in equation 3-1 we can calculate the minimum current needed assuming a one electron transfer using $9.6x10^4$ s A mol^{-1} for F .

$$m = \left(\frac{Q}{F}\right)\left(\frac{M}{z}\right) \qquad \textbf{3-1}$$

This gives a value of $3x10^{-3}$ A, however it is important to note this assumes all the products reach the capillary inlet. Given that all the electrodes used have a spatial component and the inlet is a point source this is a very conservative number.

Another more realistic way to look at the minimum current needed is to calibrate gas and experimental values. In the following calculations we will assume the reaction is selective to SO_2 and is a single electron transfer. We will use the flow rate of 200 ml

min^{-1} which is typically used for nitrogen in experiments which had 200 ppm of SO_2 added to it. With these values we obtain $1.4x10^{-4}$ mols s^{-1} of SO_2. This value doesn't take into consideration the effect of dilution from the other gases produced and higher temperature. To make sense of this value, under experimental conditions this gave a response of around $4x10^{-11}$ Torr against a background of $1x10^{-10}$ Torr. This was at the extreme range for the detector and was only obtained by increasing dwell time. In order to take a readable measurement a change of at least 10% would be needed, which yields $1.4x10^{-5}$ mols s^{-1}. Again using Faraday's law in equation 3-1, this gave a value of 1.3 A. This value would allow the capillary to be placed anywhere above the electrode and a change would be measured. From the two calculations above we have a very conservative estimate of 10^{-3} A to a more realistic value of 1 A as the minimum amount of current needed to see a response. It is important to mention both assume 100% reaction efficiency and selectivity towards a specific reaction.

3.3 Parallel flat blocks

From previous research[102] it appeared redox chemistry based on electron transfer could take place in a flame. The simplest design to explore this theory was two plane electrodes opposing each other with a flame flowing through the middle. Carbon (SGL Carbon Group – Grade R 7340), brass (Advent), and stainless steel (Advent) material where fashioned in to blocks of 30 mm by 30 mm by 5 mm. A flat groove was also created in the centre to act as a channel and was 10 mm wide and 1 mm deep. A 0.5 mm hole was drilled through the centre of the block, 10 mm from the base to allow the capillary as described in section 2.5.1 to be placed. The blocks were supported by 2.8 mm thick ceramic rods that fitted into holes on the burner top as describe in section 2.4.1. The edge nearest to the flame were tapered to act as a guide into the channel created when the two electrodes where facing each other. A schematic of this arrangement is shown in Figure 3-1.

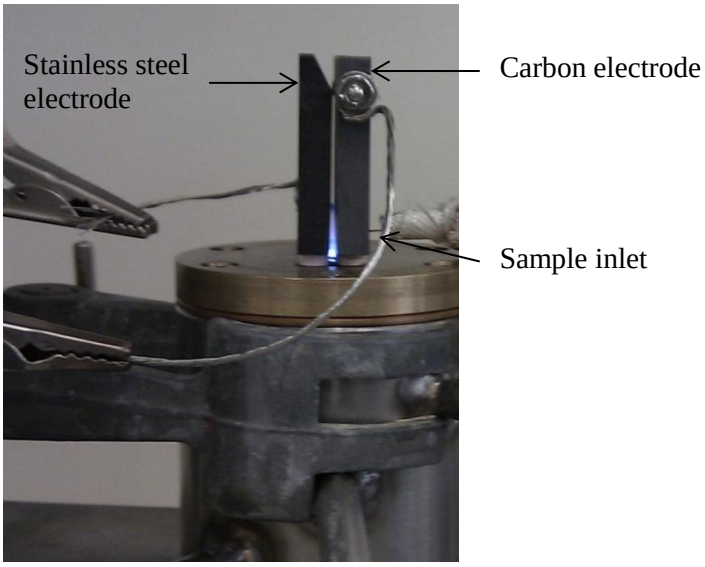

Figure 3-1: Photo showing positioning of the system using two flat blocks that act as electrodes. This setup used the electrode placement as described in section 2.4.1 and the gas and burner support platform as in section 2.2 and 2.3 respectively. The burner top sustained a methane flame using the gas ratios of 1.0/2.0/2.3 for $CH_4/O_2/N_2$ respectively, and the capillary was placed at a height of 4 mm.

Two experiments were conducted to see the effect of using brass or carbon as the negatively charged electrode. The positive electrode was made from stainless steel in both cases and voltages of ±150 V and ±75 V was used while scanning with a mass spectrometer. A gas ratio of 1.0/2.0/2.3 for $CH_4/O_2/N_2$ respectively was used and the mass spectrometry inlet placed at a height of 4 mm on the negative side. The procedure and processing used is described in section 2.8 and 2.9 respectively. For the masses 12-17, 19, 20, 22, 24, 30, 34, 36, 40 no observable changes from the baseline could be detected.

3.4 Mesh layered electrode

In order to maximize surface area and thus the current passed, a mesh styled electrode configuration was developed. Three layers of stainless steel meshes using ceramic spaces to insulate them from each other allowed a flame to sit in between two meshes. The first layer was used to change the flow characteristics of the premixed gas such that a stable flame could be created on top of it. The next layer would act as a counter electrode while the one above it was used to make sure the flame would stabilise on the bottom layer. This was achieved by using a lower aperture which helped modify the flows. A brass plate was used to screw down on the whole assembly. Figure 3-2

illustrates this mesh layered electrode. In order for a stabilised flame to be produced on the first mesh, the whole assembly had to be placed careful and at a specific location on the brass top where the seven holes were free to vent the premixed gas through the brass support.

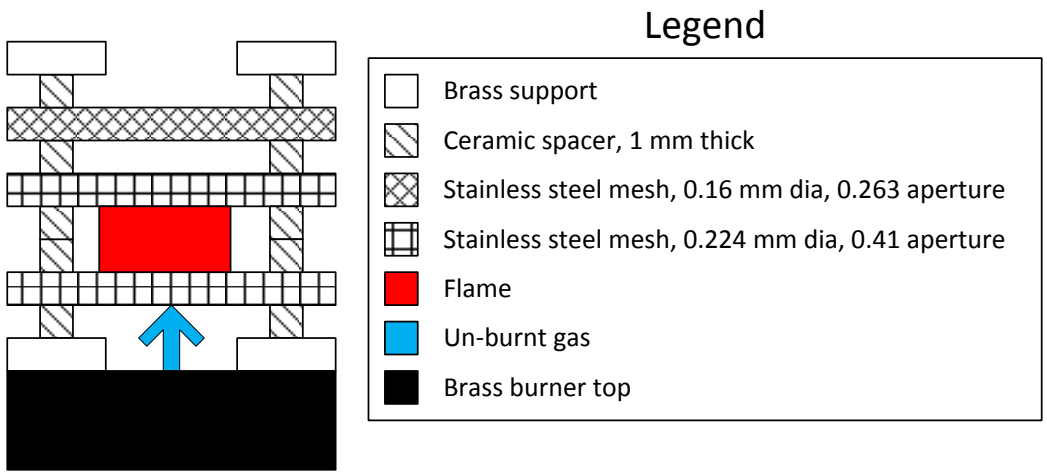

Figure 3-2: Diagram showing the layering of the mesh assembly electrode design. Meshes were supplied from Advent

In order to sustain a flame, the flow rate of 170/175/65 ml min^{-1} for $CH_4/O_2/N_2$ respectively was used. Under this configuration it was found a minimum resistance of 1.0 ± 0.2 MΩ was measured between the first layer and second, 18 ± 1 MΩ between the second and third layer and finally 19 ± 1 MΩ between the first and third layer. All readings were measured by a Keithly multimeter (175A). Unfortunately due to the electrode design mass spectrometry readings couldn't be taken due to condensation in the capillary when being placed over the electrode assembly. However using the value of 1.0 ± 0.2 MΩ for the first layer and the minimum current range needed for detection from section 3.2 (1 A - 10^{-3} A) indicates a voltage from 10^2 – 10^5 V needing to be applied.

3.5 Interdigitating pins

It was determined that turnover had to be greatly increased to observed the electrochemical effect on a flame. In order to achieve this, a high surface area geometry consisting of interdigitating wires from two brass blocks was developed. 35 tungsten wires of 0.5 mm thickness (99% Purity Advent) were protruded from one side using a brass block as shown in Figure 3-3a, while 24 from the other as in Figure 3-3b. On the side of the brass block not facing the flame, a rectangle area was hollowed out to ease fabrication of the numerous holes. Steel wire was placed in the rectangle recess to create a good contact between the tungsten wires and brass support, and high temperature adhesive was used to ensure the wires didn't move. Depending on the experiment one of the tungsten pins could be replaced with a capillary inlet to facilitate mass spectrometry reading. The placement of the brass support block was the same as in Figure 3-1 which results in Figure 3-3c.

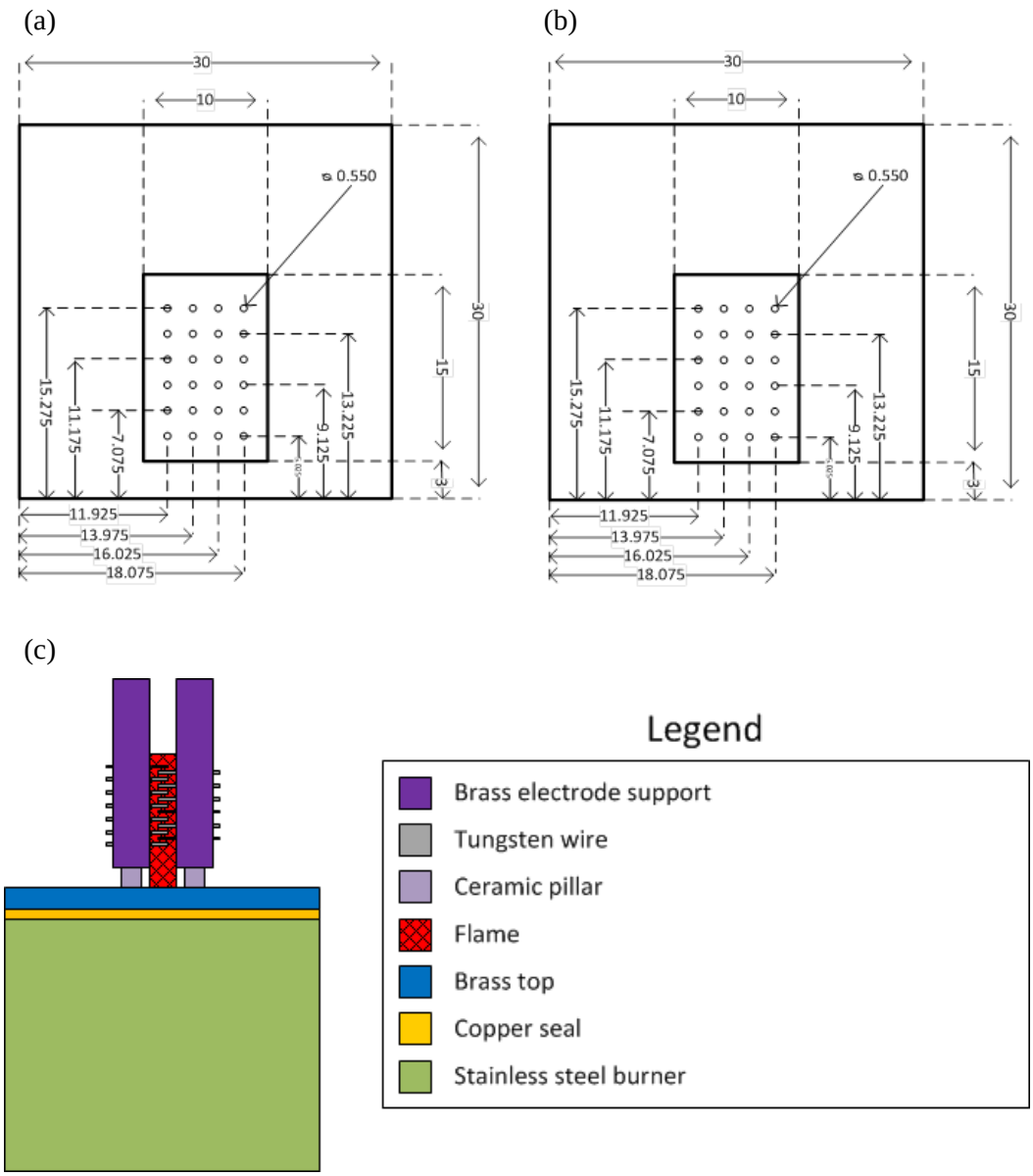

Figure 3-3: Schematic of the interdigitating pins design showing the (a) left electrode and the (b) right electrode and when (c) put together.

Using this configuration it was found a maximum of 85 ± 5 µA could be passed by using a flow rate of 550/600/100 ml min^{-1} for $CH_4/O_2/N_2$ respectively. Like the previous designs this is well short of the calculated current needed of 1 A - 10^{-3} A for detection as shown in section 3.2.

3.6 Point to plane configuration

The next geometry tried was a point electrode opposing a plane electrode. This configuration is typically used to create corona discharges. Various slopes were tried by varying the angle of the electrode, from a very sharp point to a blunt point.

3.6.1 Plane electrode

The plane electrode in the point to plane configuration was made using a brass support with a 10 mm by 9 mm by 1 mm slot. This allowed inserts of different material to be used. The brass support used two screws with washers to hold and make a connection with the material that was being investigated. As positoning was found to be critical, ceramic spacers were used to ensure the tickness of the brass support and material was 5.30±0.05 mm. This was measured using a micrometer at three different points. The plate electrode was fixed in place as described in section 2.4.2 and together, the position of the material could be reproducibilty placed with an accuracy of 10 micrometres. This value was obtained by placing the plane electrode and measuring it's position then removing it and dismantling it. Reassembeling it and placing it again and taking it's position then repeating this procedure two more times. A 0.5 mm hole was drilled through the brass support in the center to allow the capillary as described in section 2.5.1 to be placed 10 mm from the base of the brass support. Figure 3-4 illustrates the plane electrode.

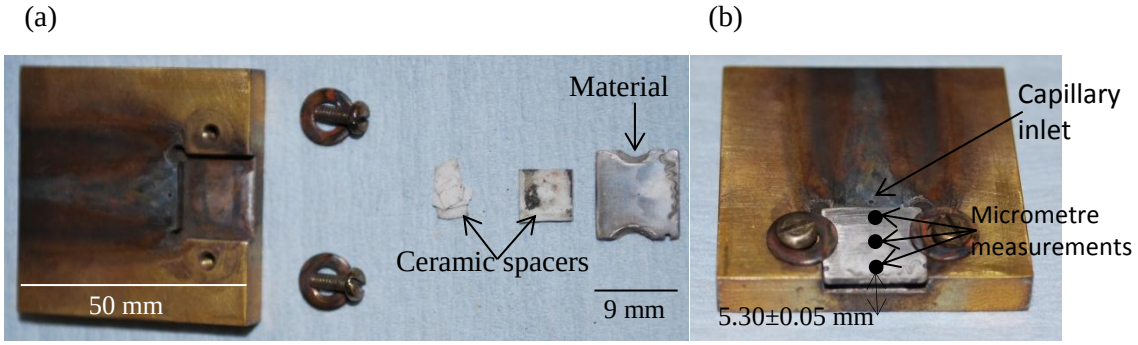

Figure 3-4: Photos showing the breakdown of the (a) plane electrode setup and (b) assembled.

3.6.2 Point electrode

The first point electrode explored was a stainless steel Luer-Lock hypodermic needle (16g x 4’’). The advantage of this needle was a defined slope, however the needle rapidly deformed after being placed in the flame. The next material tried was 1 mm diameter platinum wire (99.95% purity, Advent Research Materials). Cost prohibited having the material manufactured to exact dimensions so was shaped by using sand paper. These electrodes were able to keep their shape and not melt. This section aims to show the response of three different shaped electrodes. An electrode with no slope, medium slope and steep slope. All three were created from a length of about 30 mm of the 1 mm diameter platinum wire.

The electrode with no slope was created by sanding down the top face of the platinum wire. This was done by holding the wire perpendicular to the sand paper and carefully moving the wire in a figure of 8 pattern until the face seemed flat. The sides were very lightly sanded to ensure there were no sharp edges. Figure 3-5 (a) shows the electrode formed. The electrode with the steep slope was created by holding the wire in a vice pointing upwards with roughly 10 mm of Pt protruding. Each side was sanded using 180 grit sand paper at an angle until a point electrode as shown in Figure 3-5 (c) was formed. The medium slope electrode was made in the same way as the steep slope however the angle used was less steep. The electrode formed is shown in Figure 3-5 (b). From Figure 3-5 it is clear three different shaped electrodes were made.

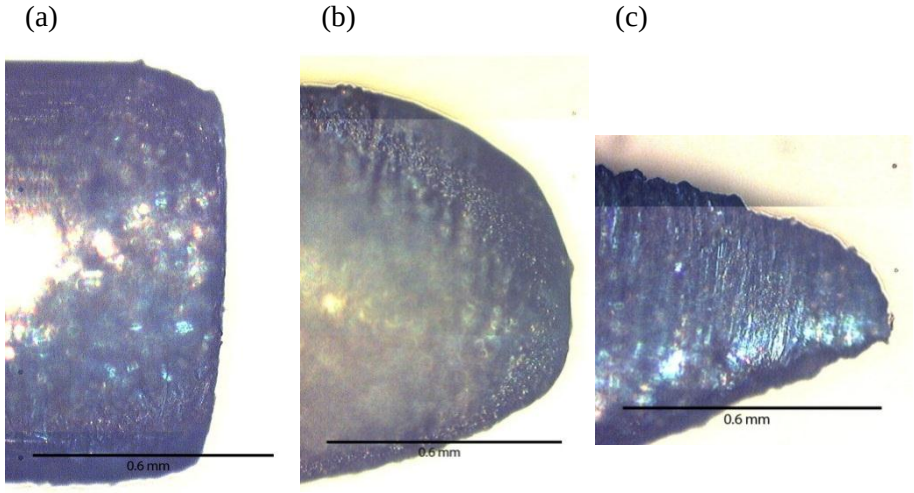

Figure 3-5: Photos of electrodes used. (a) No slope (b) Medium slope. (c) Steep slope.

3.6.3 Positive discharge results and discussion

The following results will explore a positive discharge created with the point to plane system. First starting with the current-voltage characteristics, then the effect of the discharge on the ratio change of mass 44 will be discussed.

3.6.3.1 Current – Voltage trace

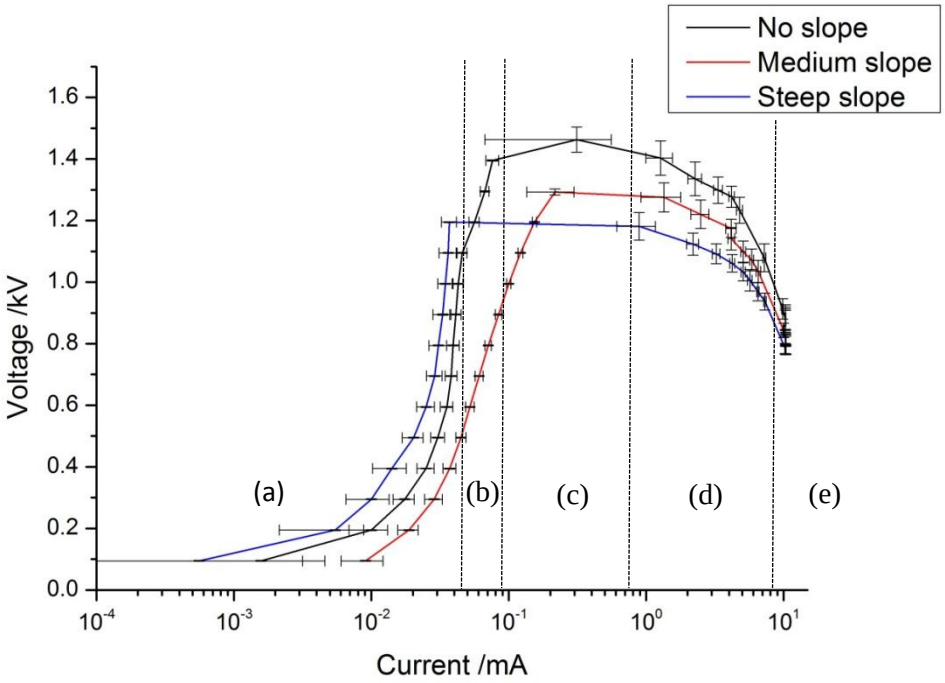

Figure 3-6: Graph showing log of current against voltage for three different Pt point electrodes as shown in Figure 3-5. Electrodes were placed 2.05 mm away from a Pt plate material held in place as described in section 3.6.1. Each point represents 200 data points obtained by holding the set potential for 2 seconds. Voltage steps increasing by 100 V were applied from 0-5000 V while the current was set to 10 mA. Electrodes were placed 2.4 mm above the burner top sustaining a methane flame using the gas ratios of 1.0/2.0/2.3 for $CH_4/O_2/N_2$. Setup of the electrode system and support platform as described in section 2.

Figure 3-6 illustrates the current – voltage response from three electrodes of varying slope steepness. It can be seen that all three show the same basic trend. They start off with an exponential increase in voltage as the current saturates (a), followed by a slight increase in current (b), an apex (c) then a rapid decrease (d) and finally converging on a single point (e). The regions marked in Figure 3-6 are only associated with the no slope electrode.

Region (a) describes the response from the electrons due to the background ionization from the flame and surroundings traveling across the gap. It is important to note the error bars are uniform and thus indicate a steady flow of electrons rather than an intermittent stream. It is clear the electrodes with no slope and with a steep slope forms a saturation region however the medium slope does not. Comparing the two that forms a saturation region, the electrode with no slope seems to be able to pass more current at the same voltage. This is expected as the larger surface area means more electrons can be collected. From this the medium slope would be expected to lie between the electrode with no slope and the steep slope but instead the results show it transfers more current than the electrode with no slope. This could only happen if the medium slope electrode had a larger surface or the resistance of the flame was lower. A lower resistant flame would also support the observation that no saturation region was formed due to there being more electrons around, thus harder to saturate. The exact reason for these observations remains unknown.

Region (b) shows a slight increase in current while the error bars remain uniform. Combining equation 1-19 along with the fact that the current has increased indicates that Townsend mechanisms as described in section 1.3.1 are occurring. This only happens for the point electrode with no slope. The uniform error bar also shows that the discharge is not a streamer however the slight change in current means the Townsend discharge hasn't formed.

Region (c) is indicated where the increasing current starts to have large error bars. This is a sign that the streamer corona discharge has formed. The large error bars is due to the current being intermittent and is expected as described in section 1.3.2. For all three electrodes this is the point with the maximum voltage. The electrode with no slope was able to sustain the highest voltage. It is interesting to note that it is in this region that the trend no slope, medium slope then steep slope appears with respect to voltage applied.

Region (d) is marked just after the maximum voltage is obtained and the voltage starts to drop as higher currents are passed. It is in this region that the streamer corona discharge turns into a glow corona.

Region (e) is a single point at 10 mA which was the maximum set current. This point corresponds to the spark discharge formation and happens for all three electrodes. It is the sudden drop in voltage and the decrease in error that indicates that the streamers have formed into a single narrow channel.

Overall the electrodes with no slope and a steep slope show consistency with the theory used to explain Townsend and corona discharges however the point electrode with a medium slope showed some unexpected features. It is important to note that the power supply had a quoted error of 1% of its full scale value, which was around 0.1 mA however the trends observed below this value fit with theory.

3.6.3.2 Voltage against ratio change of mass 44

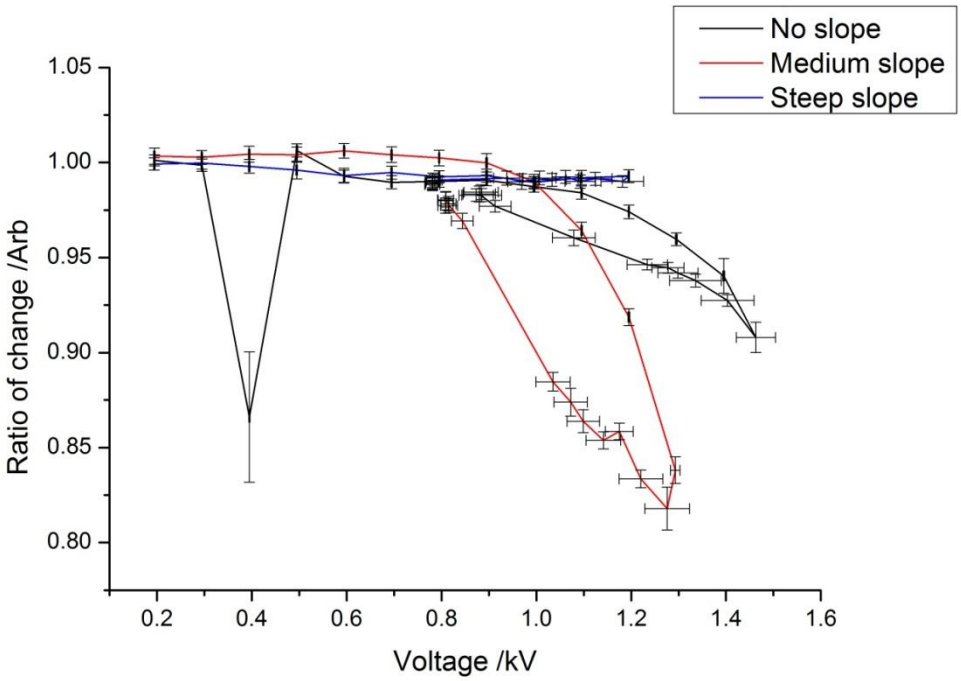

Figure 3-7: Graph showing voltage against ratio change of mass 44 amu taken by a mass spectrometer. Setup as described in Figure 3-6.

Figure 3-7 shows the corresponding results obtained from a mass spectrometer sampling mass 44 which is assumed to be CO_2, while Figure 3-6 was created. The electrode with no slope had an anomalous reading at 0.4 kV due to condensation briefly blocking the capillary which caused a large drop in pressure. All three electrodes show a relatively flat response in the beginning however the electrodes with a medium

slope and no slope show a change in CO_2 readings at higher voltages, while the electrode with the steepest slope showed negligible change. This shows that electrode geometry has a greater effect than the potential applied on changing the amount of CO_2. This is not surprising given Figure 3-6 shows corona discharges are formed, which are known to be highly dependent on the geometry of the stressed electrode.

The change in CO_2 for the electrode with no slope starts to occur right when the Townsend mechanism Figure 3-6 (b) occur. The rate of change in CO_2 was much more gradual compared to the medium sloped electrode. For both the maximum decrease in CO_2 coincides with the maximum voltage applied, which is also when a streamer corona discharge Figure 3-6 (c) is formed. Both electrodes also showed a hysteresis effect against voltage which seems to show the change in CO_2 is not solely dependent on the voltage applied. This hysteresis occurs during the same region as the glow corona discharge and the Townsend mechanism region. Given the potentials are the same in both discharges, it seems the different processes sustaining each discharge maybe the cause for the difference in ratio of change of CO_2.

All three electrodes show nearly the same value of CO_2 reduction at around 0.8 kV, which corresponds to Figure 3-6 (e). At this point they have very similar applied voltage, current and type of discharge being formed, so the change in CO_2 is expected to be similar. Overall it appears that having a point electrode that is too sharp yields no response though having the opposite, is also not optimal, and instead a balance is required. The maximum change in CO_2 was achieved by using the medium sloped point electrode which yielded a decrease of around 18% and was obtained near 1.3 kV.

3.6.3.3 Current against ratio change of mass 44

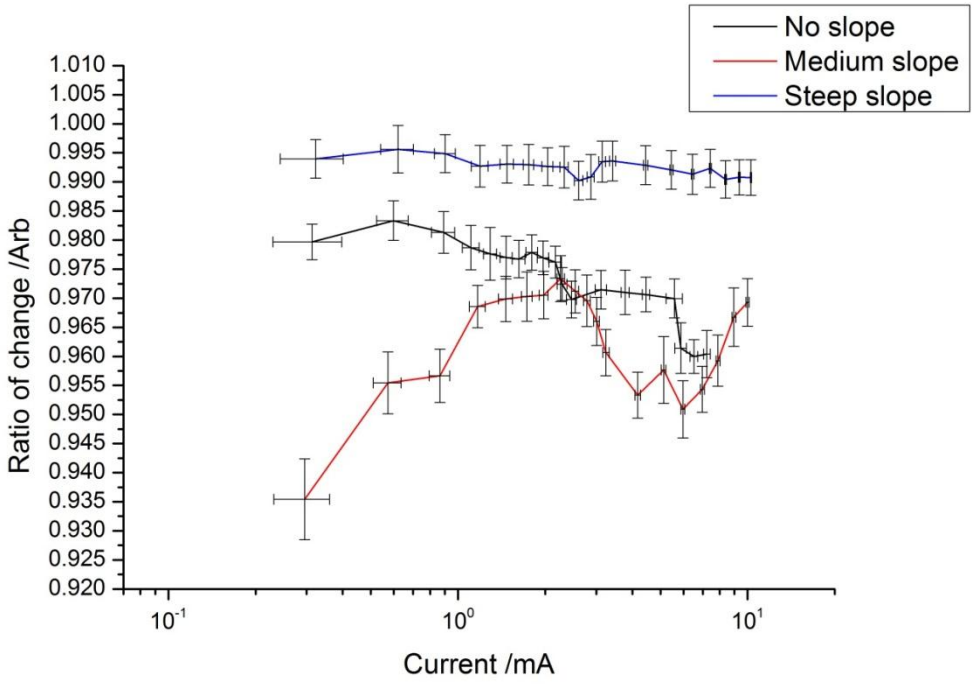

Figure 3-8: Graph showing log of current against ratio of change in mass 44 amu taken by a mass spectrometer. Setup as described in Figure 3-6 using current steps instead of voltage steps of 0.25 mA from 0.25 – 3 mA then in 1 mA steps from 4 – 10 mA both with a set voltage of 2.5 kV.

Figure 3-8 shows the response when changing the current while holding the voltage at 2.5 kV for the three electrodes being investigated. All three show very little change in CO_2 when increasing the current passed. No trends could be obtained as the sharp electrode showed no change with varying current however the electrode with a medium slope showed less decrease as increasing current, while the electrode with no slope showed the opposite. From this it is clear that the ratio of change in CO_2 is independent of current passed.

3.6.4 Reproducibility results and discussion

As the setup was custom built it was important to check the repeatability of the system. For each experiment a repeat was done at the end to insure changes were independent of the time the electrode was in the flame. It should be noted though that because an automated routine was used, repeats done on different days with the same routine could easily mask an under lying systematic error. In order to check this, during one experiment the repeats done at the end were conducted in a random order.

3.6.4.1 Current – Voltage trace

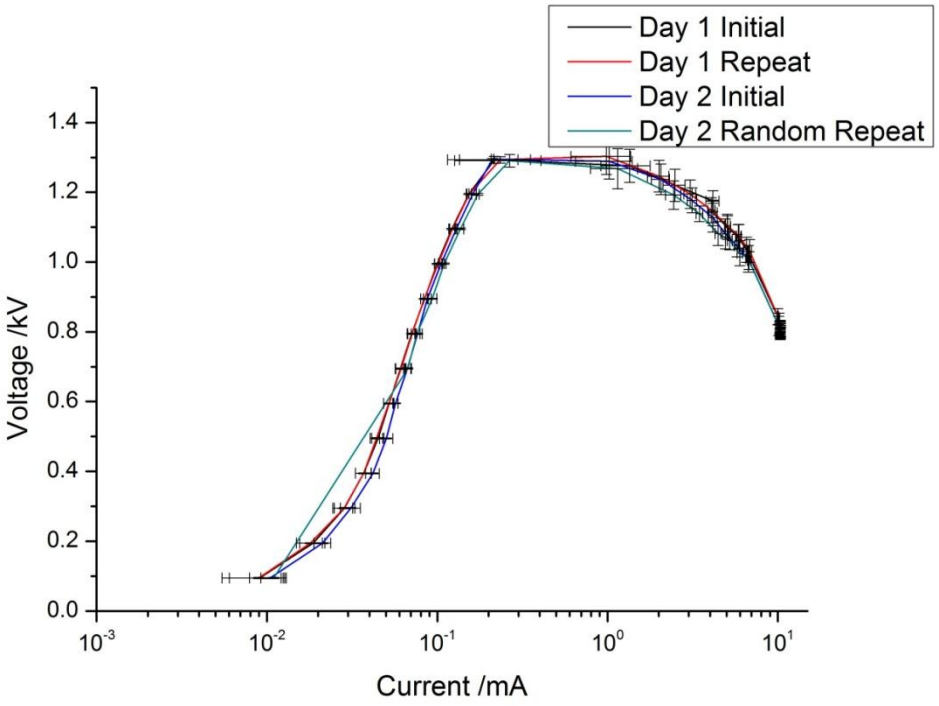

Figure 3-9: Graph showing log of current against voltage for 2 experiments each with one repeat taken on different days. A medium sloped Pt point electrode as shown in Figure 3-5 (b) was used and placed 2.05 mm away from a Pt plate material held in place as described in section 3.6.1. Each point represents 200 data points obtained by holding the set potential for 2 seconds. Voltage steps increasing by 100 V were applied from 0-5000 V while the current was set to 10 mA. Electrodes were placed 2.4 mm above the burner top sustaining a methane flame using the gas ratios of 1.0/2.0/2.3 for $CH_4/O_2/N_2$. Setup of the electrode system and support platform as described in section 2.

From Figure 3-9 it is clear the current – voltage trace is reproducible within error bar. The straight line joining the points at in the 10^{-2} mA region for the Day 2 Random Repeat is due to lack of points and not a real trend. It is important to note that all the features discussed in section 3.6.3.1 regarding both the features and error bars associated with the trace are present in all 4 graphs.

3.6.4.2 Voltage against ratio change of mass 44

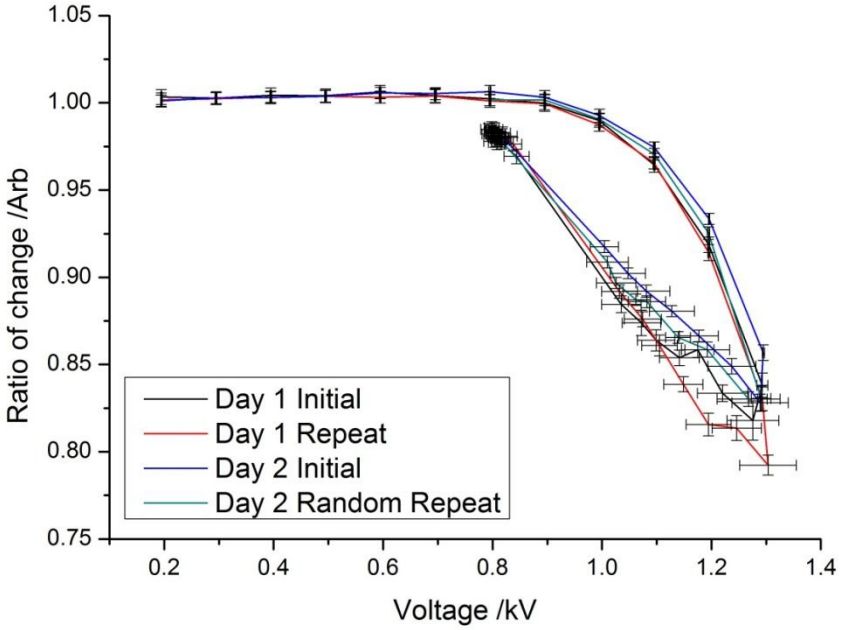

Figure 3-10: Graph showing voltage against ratio change of mass 44 amu taken by a mass spectrometer. Setup as described in Figure 3-9.

Figure 3-10 should show 4 curves all within error bars of each other however it appears the Day 1 Repeat falls outside this requirement. The trends of all 4 curves are reproducible; but given the high precision from Figure 3-9 suggests a systemic error could be present. On close inspection it can be seen that the repeats from Day 1 and 2 both show slightly higher changes in CO_2 response. The repeat conducted during Day 2 was closer to the initial which suggests over time something has changed that either has allowed more CO_2 to decrease or made the mass spectrometer perceive a larger change than has occurred. It is important to point out every point is checked against a control taken just before and after and normalised as described in section 2.8. The reason for the slight shift is currently unknown however possible reasons may include temperature effects or oxide formation.

3.6.5 Negative discharge results and discussion

Along with experimenting on different electrodes slopes, the effect of polarity was explored. First the current – voltage trace will be shown followed by the effect the discharge had on mass 44 amu.

3.6.5.1 Current – Voltage trace

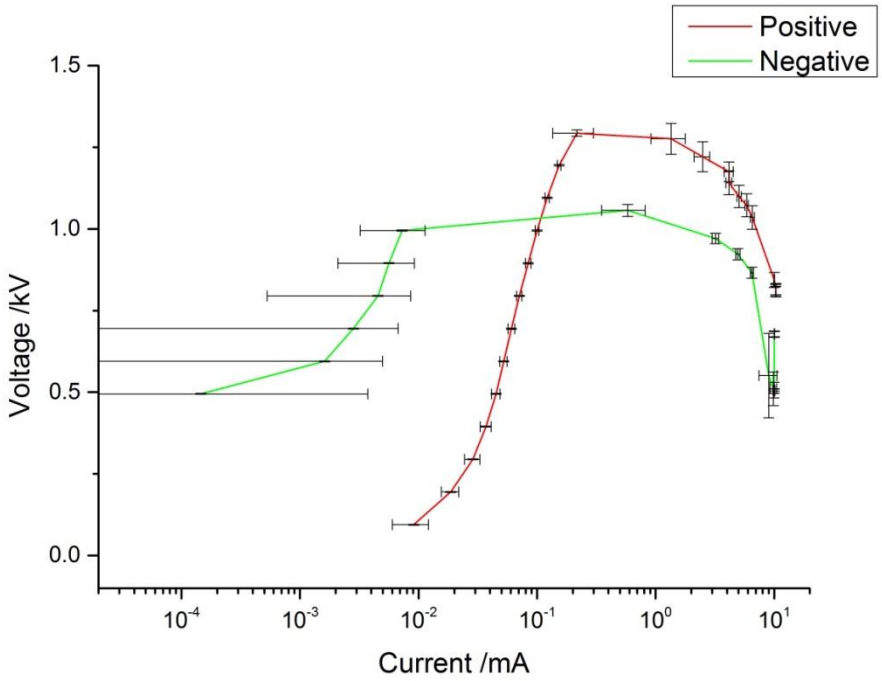

Figure 3-11: Graph showing log of current against voltage for positive and negative applied polarities. A medium sloped Pt point electrode as shown in Figure 3-5 (b) was used and placed 2.05 mm away from a Pt plate material held in place as described in section 3.6.1. Each point represents 200 data points obtained by holding the set potential for 2 seconds. Voltage steps increasing by 100 V were applied from 0-5000 V while the current was set to 10 mA. Electrodes were placed 2.4 mm above the burner top sustaining a methane flame using the gas ratios of 1.0/2.0/2.3 for $CH_4/O_2/N_2$. Setup of the electrode system and support platform as described in section 2.

From Figure 3-11 we can see the shape of the negative current-voltage trace has some similarities to the positive trace. A regions of exponential increase in voltage as the current tends to saturate, followed by an apex, than a rapid decrease and finally converging on a point can be seen. The differences here are instead of a streamer discharge forming a pulsesless corona forms as explained in section 1.3.2. Also the maximum voltage obtained is much lower than the positive discharge.

3.6.5.2 Voltage against ratio change of mass 44

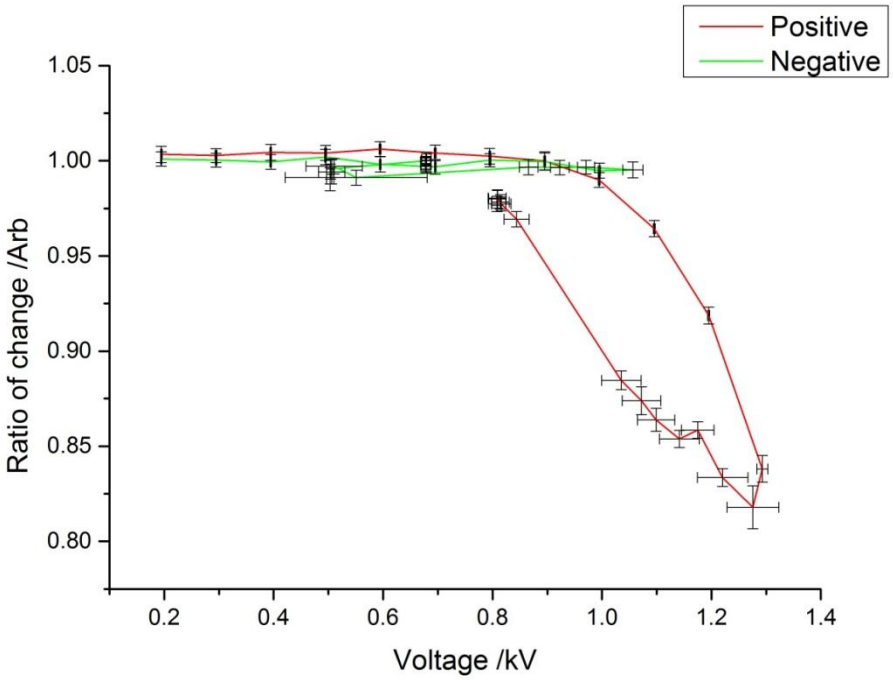

Figure 3-12: Graph showing voltage against ratio change of mass 44 amu taken by a mass spectrometer. Setup as described in Figure 3-11.

From Figure 3-12 we can immediately see when applying a negative discharge there is negligible difference in the change in CO_2. Although the maximum voltage reached by the negative discharge is only around 1.1 kV this is enough that had the discharge been positive a change would have been seen. From this the polarity of the discharge seems to play a role in changing the amount of CO_2.

3.7 Summary

The experiments in this chapter show that using two electrodes in a point to plane configuration appears to change the amount of CO_2 being sampled from a methane flame. The optimal point shape was one with a medium slope and made from 1 mm dia Pt. With this electrode, CO_2 response was decreased by a maximum of 18% when applying a voltage of positive 1.3 kV which coincided with the formation of a streamer corona discharge. It was also shown there is some relationship between voltage and the amount of CO_2 being changed however it was impossible to tell if it was a direct or indirect relationship. On the other hand it was shown the change is independent of current applied.

4 Characterisation of corona discharges created in a methane flame

4.1 Introduction

This chapter will explore the discharges created in a methane flame by the point to plane electrode configuration in chapter 3 in more depth. This will be done primarily by exploring the effect of distance between the point and plate electrodes on the resulting discharges created.

Section 1.5 details the important physical aspects regarding flames and this section will be concerned with the properties of using methane as a fuel. Methane was chosen as it was the simplest hydrocarbon flame and was hoped would make analysis of mass spectrometry data simpler. As there are many reactions that occur during combustion, the combustion mechanism for methane can be simplified as shown in Reaction 4-1 and the overall reaction at stoichiometry in Reaction 4-2[103]. Using simulation and sensitivity analysis the primary and secondary rate limiting reaction steps are shown in Reaction 4-3 and Reaction 4-4[104] respectively.

$$CH_4 + O_2 \rightarrow CO + H_2 + H_2O$$

$$CO + H_2O \rightarrow CO_2 + H_2$$

$$O_2 + 2H_2 \rightarrow 2H_2O$$

Reaction 4-1

$$CH_4 + O_2 \rightarrow CO_2 + 2H_2O$$

Reaction 4-2

$$H + O_2 \rightarrow OH + O$$

Reaction 4-3

$$CO + OH \rightarrow CO_2 + H$$

Reaction 4-4

At stoichiometric ratios the theoretical adiabatic flame temperature from thermodynamics was found to be 2318 K [105] when burnt in air (25% O_2, 75% N_2). Other important properties of methane are its flammability limits which are 5% and 61% in lean and rich O_2 environment respectively[106], and it's maximum burning velocity of 36.2 cm s^{-1} [107], these values determine the operational limits of the experiment.

Another important aspect to consider are the ions present in the flame. In this case Reaction 4-5 describes the reaction that is suggested to be the dominant primary reaction[108].

$$CH + O \rightarrow CHO^+ + e^-$$

Reaction 4-5

Given the flame produces many different species[68], once the primary CHO^+ ion has formed, it can then go on to form other ions such as the important H_3O^+ ion as shown in Reaction 4-6[108].

$$CHO^+ + H_2O \rightarrow H_3O^+ + CO$$

Reaction 4-6

This chapter will start by showing the effect of distance between the point to plane electrode configuration when in a methane flame. Using two different distances the streamer, glow and spark corona discharge were formed and will be explored in depth. Next a comparison between the discharges in methane and air will be made. Finally the effect of applying the breakdown voltage on CO_2 will be shown for different distances.

4.2 Experimental

4.2.1 Electrode design

The electrode design and setup was the same as described in section 3.6 however a new Pt point electrode had to be made. The procedure for making the electrode is described in section 3.6.2 and was made to be as similar to the electrode with a medium slope seen in Figure 3-5 (b). The electrode from section 3.6 and the newly created electrode are shown in Figure 4-1 for comparison.

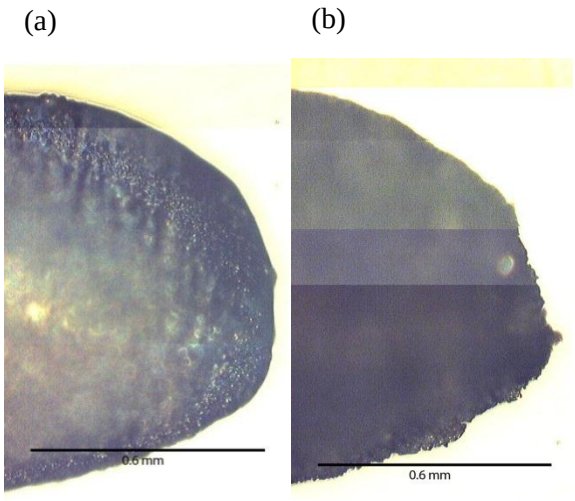

Figure 4-1: Photo of (a) the medium sloped point electrode used in section 3.6 and (b) the electrode used to create the results in this chapter.

From Figure 4-1 it can be seen the size and the overall curvature of the two electrodes formed are visually similar. Electrode (b) seems to show a slight protrusion and the point is less round when compared to electrode (a). It is hard to predict what the effect the slight differences between the electrodes will cause. This is as when using a point to plane setup, slight variances in the point geometry will cause large variances in the electric field produced.

4.2.2 Video analysis

A video camera was used to record experiments so that detailed visual observations could be made after. This allowed experiments to explore more variables in a shorter period of time. A Sony HDR CX550E using a charge-coupled device took images at a resolution of 1440x1080 pixels. This was done at a rate of 50 fields per second in an interlaced manner. Due to the fields being interlaced, this would equal to 25 complete frames per second. In order to extract more data, the raw fields taken at 50 per second were used. Interpolation was used for deinterlacing allowing footage at 50 frames per second to be analysed. It is also important to note the detector used non square pixels and when resized to square pixels this was a resolution of 1920x1080. Due to the large size of the raw footage and the area of interest being relative small, each frame was cropped into a segment of 400x400 pixels at the desired area.

As the region of interest was relatively small and the intensity from the flame and Pt point electrode was very high, observing changes between images was difficult. To make the changes more visible, simple image processing was done. The frame just before the frame of intent was used as a control. All following frames had their red, green and blue values subtracted from this control frame. While changes can be seen much more clearly, due to the subtraction the absolute colour was lost. Figure 4-2 shows an example of a frame that has been captured and its corresponding processed image. Further image analysis could have been done such as using histograms to find the maximum peak intensity and spatial differences but was not carried out. This was as the effect of reflections, heating up of metals and other effects could not properly be accounted for.

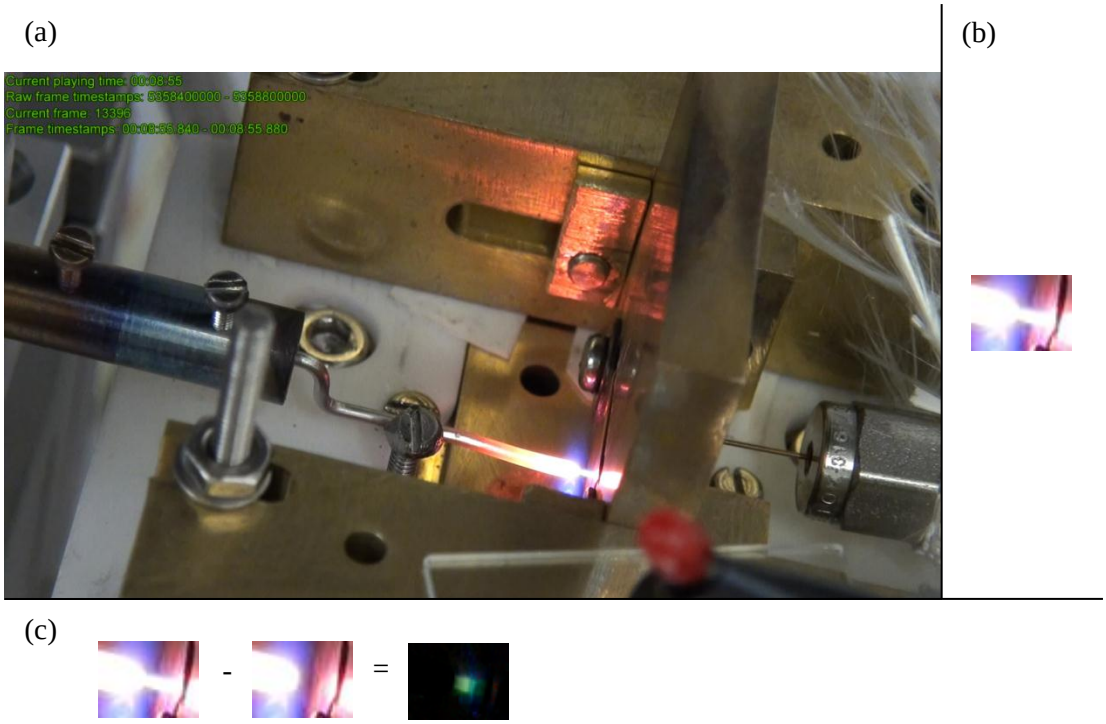

Figure 4-2: (a) An example of a frame capture from a Sony HDR CX550E that has been resized to its correct aspect ratio of 16:9 at 1920x1080 resolution, but scaled down by half. (b) Region of interest from (a) at its native resolution. (c) The result of image subtraction processing.

As mentioned in section 2.8 the video camera was synchronised using an LED that was pulsed at certain points during the experiment. Unfortunately as the camera footage was taken at 50 Hz and electrical readings at 100 Hz the pulsing LED alone was insufficient to synchronised single frames to the electrical readings. To get this resolution the footage was viewed back frame by frame looking for a change that appeared in both the electrical and video footage. Fortunately when the streamer corona discharge forms, a short pulse of light is emitted with a corresponding peak in current and drop in voltage. This was confirmed by counting the number of peaks over time against the number of flashes observed. For example in one experiment 25 electrical peaks matched exactly with 25 visual flashes. Video footage was then synchronised by using the first frame a pulse of light was observed. The video was synchronised every time footage was used to prevent accumulation of error in case of drifting clocks.

4.2.3 Audio analysis

Along with the video footage obtained, the camera also recorded an audio feed during the experiment. This was done at 5.1 channels and a sample rate of 48 kHz with 16 bits

of resolution. From the Nyquist-Shannon sampling theorem this meant a frequency of up to 24 kHz can be analysed. The camera used the AC3 compression codec with a maximum bandwidth of 448 kbps.

While audio analysis could be done on a frame by frame basis it is much more useful to look at longer time scales such as the overall waveform and frequency distribution. The spectrum started by exporting only the left channel into the waveform audio file format (wave) and disregarding the others. This was done to reduce the amount of data and to insure the signal would not be further altered by another compression algorithm. The file was then sliced at the desired points. These points corresponded to the same ones used for the video footage.

The next step was to choose the correct number of samples to create a frequency analysis. As the AC3 codec used by the camera processes the raw analogue signal by putting 256 frequency coefficient in to blocks[109], a sample size of 256 was used. Any higher and the results would be artefacts and lower would lose information. These frequencies were then background subtracted using frequency spectrums obtained near the time of interest but when no discharge was being operated. It is important to note that microphone frequency profile responses can vary greatly, and as the audio has not been calibrated, the magnitudes of values cannot be used.

When generating the full waveform the sample rate was 1000 Hz. However when the files were sliced previously, they could only be done to the nearest 0.04 s. This meant synchronisation had to be done otherwise the electrical readings and audio could be off by two electrical reading. Synchronisation was done in the same way as the video, using the large audio burst to correspond to a peak in current. This was confirmed by counting the number of bursts over time and compared to electrical peaks. For example 25 audio bursts matched with 25 electrical peaks. The waveform was then shifted so the start of the burst matched exactly with the start of a peak. Unfortunately this meant is it impossible to tell if the sound comes before or after the current peak.

4.3 Results and discussion

4.3.1 Effect of distance between electrodes on electrical resistance in a methane flame

The following result aims to characterise the methane flame's resistance against distance. This can be used to infer some structure about the flame.

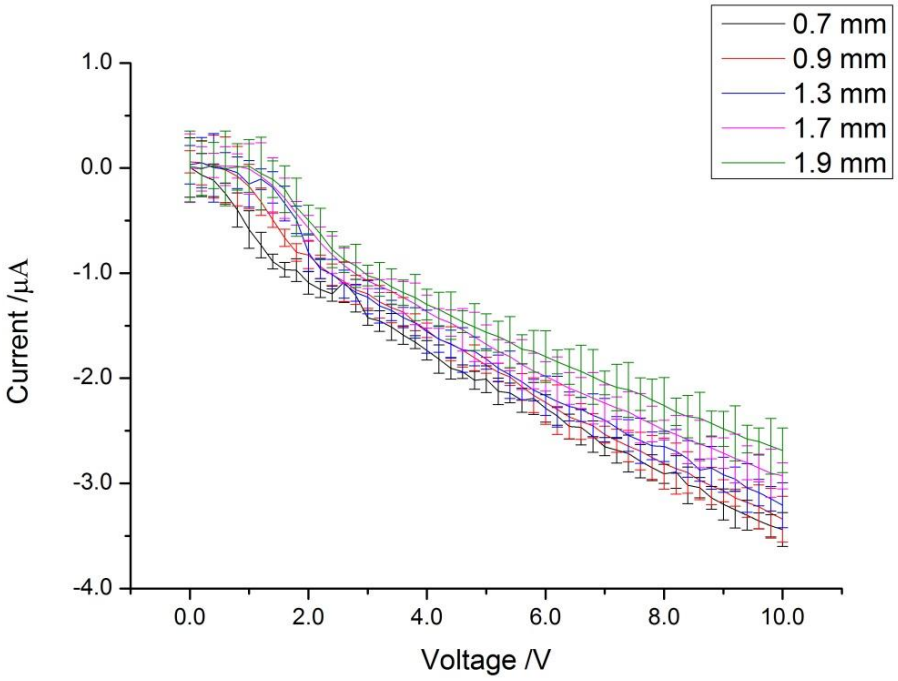

Figure 4-3: Graph showing current against voltage for 5 different distances. Each point represents 200 data points obtained by holding the set potential for 2 seconds. Voltage steps were increased by 0.2 V. Point electrode was placed 2.4 mm above the burner top sustaining a methane flame using the gas ratios of 1.0/2.0/2.3 for $CH_4/O_2/N_2$. Setup of the electrode system and support platform as described in section 2 and 3.

From the Figure 4-3 we find the response of the current when changing the voltage from 0 V to higher voltages starts off flat, and then becomes linear. When the electrode is furthest away, the period where the current response is flat at the start is the largest. A possible reason for this is that the further away the electrodes are the greater the ohmic loss, similar to a solutions IR drop in electrochemistry. This translates into needing a higher voltage before a current can be passed.

Using Figure 4-3 we can obtain the resistance for each distance by taking the very last point and calculating the resistance as shown in Figure 4-4.

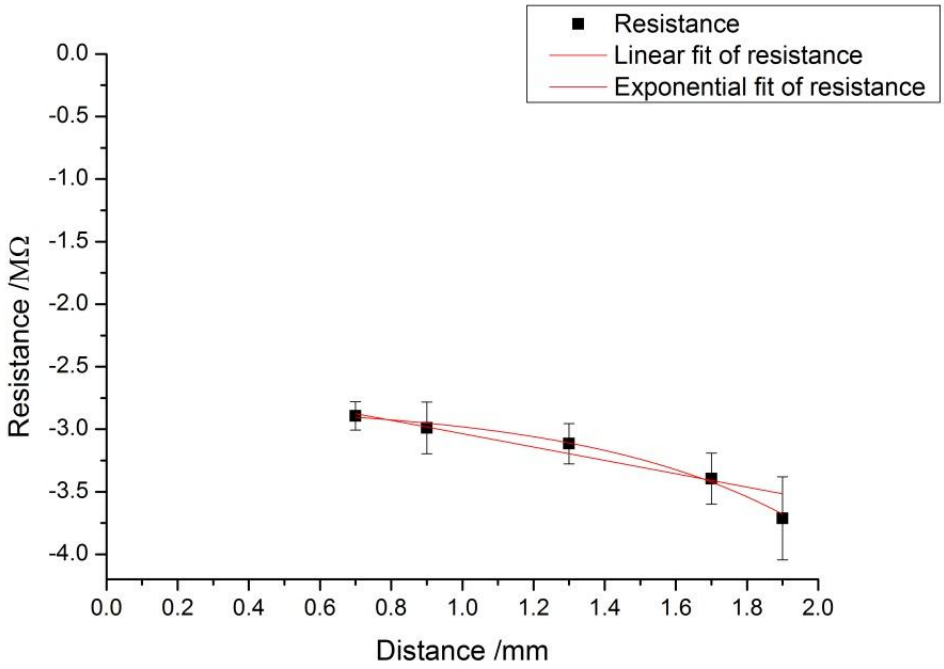

Figure 4-4: Graph showing resistance against distance using results obtained from Figure 4-3. Current values when the voltage applied was 9.8 V and 10.0 V were used to calculate resistance. The linear fit obtained was y = 0.53±0.08x + 2.50±0.10 with a R^2 value of 0.91, while the exponential fit was y = -2.79±0.07 - 0.04±0.03$e^{1.70\pm0.4\,x}$ with a R^2 value of 0.98

Figure 4-4 shows a linear and exponential fit for the resistance measured against distance, with the exponential showing a better fit. Assuming the methane flame was homogenous we would expect the fit to be linear as the resistance is due to the amount of charge carriers. Points before 1.7 mm tend to show good agreement with a linear fit however points 1.7 mm and 1.9 mm break this trend. This would suggest the region around 1.7 mm and onwards is different from the region before it. A possible explanation is that at distances around 1.7 mm the electrode is near the interface of the flame and air and thus the region more resistive.

Another feature of Figure 4-4 is that when extrapolating either the linear or exponential fit, it is a clear that at 0.0 mm the resistance is not zero as expected. A possible reason for this is that the electrodes are acting like a Langmuir probe. This is as the flame is a weak plasma and thus the size difference in electrodes allows the plane electrode to collect many more electrons than the point when not polarised.

4.3.2 Detailed current voltage trace in methane at 0.9 mm and 1.9 mm

Section 3.6.3.1 identified five different regions when a current – voltage traces was applied to a methane flame using a point to plane electrode setup. This section will go into detail of four of these regions. These regions were the background ionization, streamer corona, glow corona and the spark corona region. Current – voltage traces obtained by placing the point electrode at two distances, 0.9 mm and 1.9 mm away from a plane electrode are shown in Figure 4-5.

Although taking averages and errors can show the overall trends, detail regarding the processes that go on during a particular phase is lost. To solve this, current and voltage responses over time needed to be analysed. To do this we will examine the raw data from 4 points, one for each region and at two different distances. To get a better understanding of these responses, camera footage along with audio will be used to provide a more complete picture. Spectrograms were also calculated however meaningful interpretations could not be obtained from them. They can be found in Figure A-1 for the distance 0.9 mm and Figure A-2 for the distance 1.9 mm.

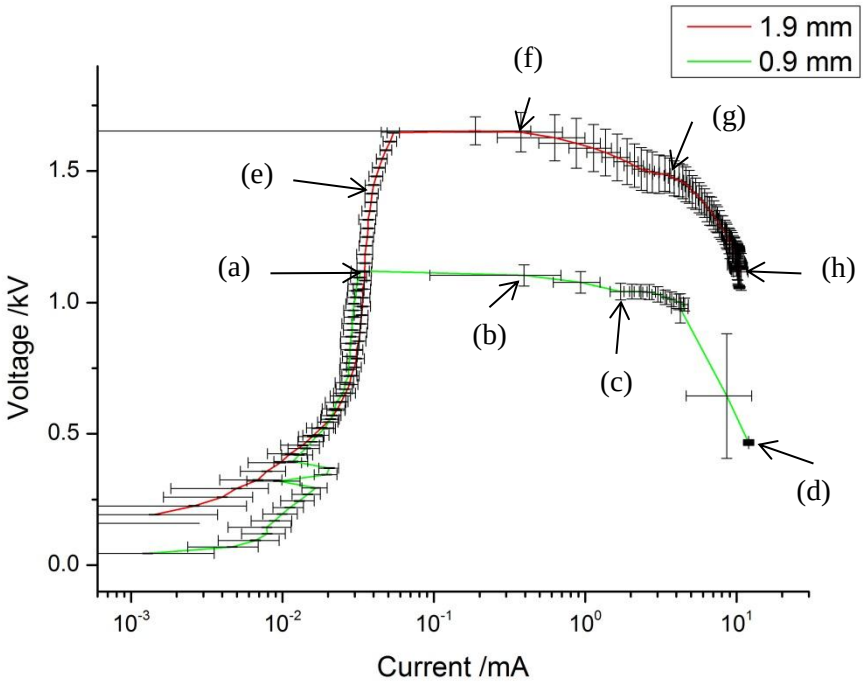

Figure 4-5: Graph showing log of current against voltage traces when a Pt point is placed at distances 0.9 mm and 1.9 mm away from a brass plate material. Each point represents 200 data points obtained by holding the set potential for 2 seconds. Voltage steps were applied from 0-5000 V. When the electrode was placed 0.9 mm steps of 25 V were done while at 1.9 mm, 33 V steps were used. For both, the current was set to 12 mA. Electrodes were placed 2.4mm above the burner top sustaining a methane flame using the gas ratios of 1.0/2.0/2.3 for $CH_4/O_2/N_2$. Setup as described in section 2 and 3.6.

Point (a) shows the maximum current passed due to electrodes from background ionization of the flame when the Pt electrodes are separated by a distance of 0.9 mm. This was when a voltage of 1125 V was set (1120±1 V measured) which passed a current of 0.033±0.004 mA.

Point (b) shows a streamer corona was formed when 1150 V was set (1100 V measured). The corresponding current measured was 0.39 mA and visually sparks were intermittently observed and heard. As higher voltages were set the stuttering rate increased.

Point (c) indicates when a corona glow discharge was formed. This occurred when 1200 V was set (1040 V measured) and a current of 1.71 mA was measured. At this point the intermittent stuttering turned into a continuous sound and a cone like discharge could be observed.

Point (d) is when a spark discharge was formed. This occurred when 1500 V was set (470 V measured) with a current of 12.0 mA. The formation of a spark could be observed and was silent to the ear.

Point (e) attempts to show the maximum current passed due to background ionization of the flame when the Pt electrodes are separated by a distance of 1.9 mm. This was done by finding when the relatively straight plateau in current appeared to turn into a linear increase. This point was when a voltage of 1452 V was set (1447±2 V measured) which passed a current of 0.040±0.005 mA.

Point (f) shows a streamer corona was formed when 1700 V was set (1650 V measured) with a corresponding current of 0.19 mA. Intermittent sparks were observed and heard which increased in rate as the voltage set was increased.

Point (g) indicates when the streamer discharged turned into a glow discharged. This occurred at a set voltage of 2050 V (1500 V measured) and a current of 2.77 mA was passed. At this point a glow discharge was observed with its characteristic cone like shape.

Point (h) is when the maximum current of 8.88 mA could be passed at the distance of 1.9 mm. This occurred with a set voltage of 5000 V (1230 V measured). Even at this current, it was still the glow discharge that was formed.

4.3.2.1 Streamer corona discharge - Figure 4-5 Points (b) and (f)

0.9 mm - Point (b)	1.9 mm - Point (f)
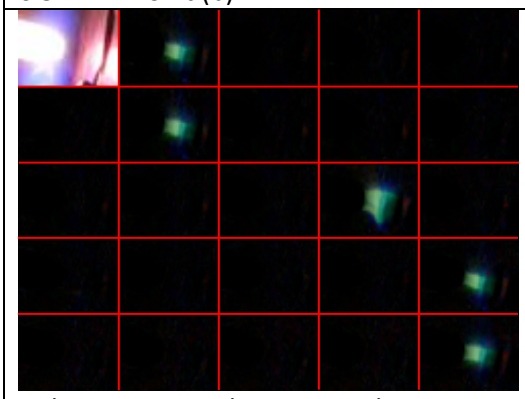	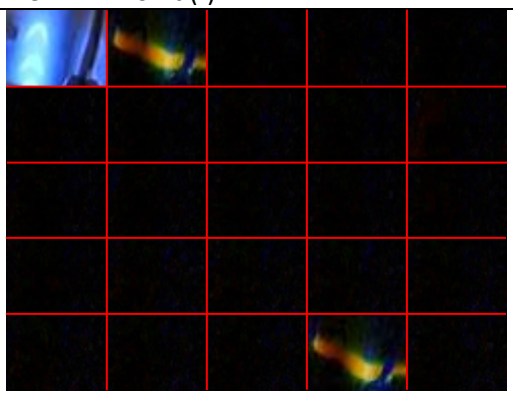
Voltage measured: 1.10±0.04 kV Current measured: 0.39±0.299 mA	Voltage measured: 1.65±0.05 kV Current measured: 0.19±0.249 mA

Table 4-1: Table showing images obtained during Figure 4-5 corresponding to a streamer corona discharge. Each section represents 25 frames which is 0.50 s. The first frame at the top left corresponds to the frame just before a discharge was formed and used for processing the subsequent frames by subtraction. Section 4.2.2 explains this in more detail. Frames are read from left to right.

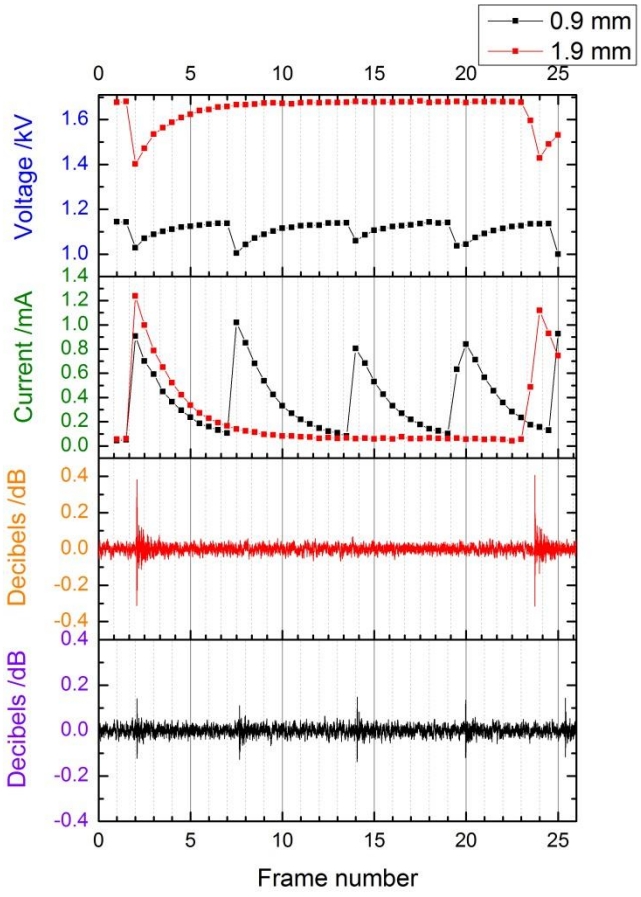

Figure 4-6: Current, voltage and decibel readings corresponding to pictures in Table 4-1 for 0.9 mm and 1.9 mm. Electrical readings were taken at 100 samples per second while audio at 1000 samples per second. Synchronisation was done as described in section 4.2 with all readings synchronised to frame 2 in Table 4-1. Frame number 1 is the top left image in Table 4-1.

4.3.2.2 Glow corona discharge - Figure 4-5 Points (c) and (g)

0.9 mm - Point (c)	1.9 mm - Point (g)
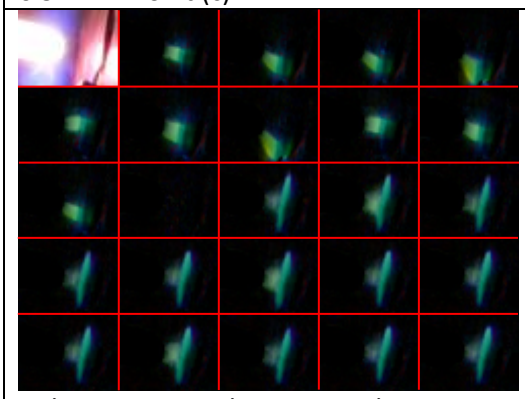	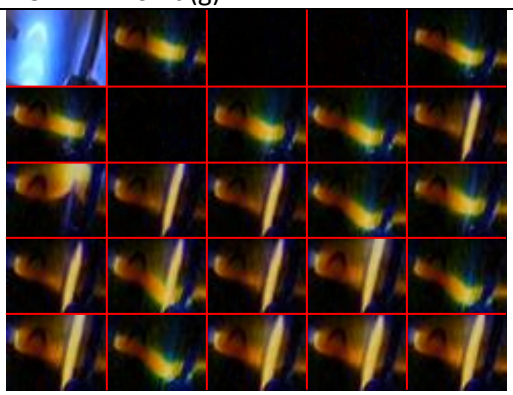
Voltage measured: 1.02±0.03 kV Current measured: 3.38±0.243 mA	Voltage measured: 1.49±0.07 kV Current measured: 3.08±0.294 mA

Table 4-2: Table showing images obtained during Figure 4-5 corresponding to a glow corona discharge. Each section represents 25 frames which is 0.50 s. The first frame at the top left corresponds to the frame just before a discharge was formed. Frames are read from left to right. Section 4.2.2 explains this in more detail.

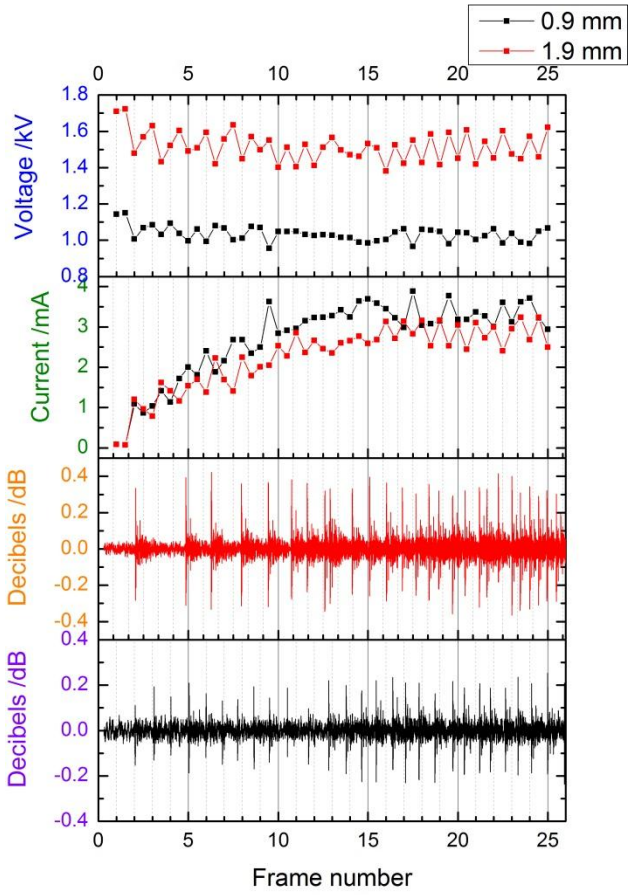

Figure 4-7: Current and voltage readings corresponding to pictures in Table 4-2 for 0.9 mm and 1.9 mm. Readings were taken at 100 samples per second.

4.3.2.3 Spark corona discharge - Figure 4-5 Points (d) and (h)

0.9 mm - Point (d)	1.9 mm - Point (h)
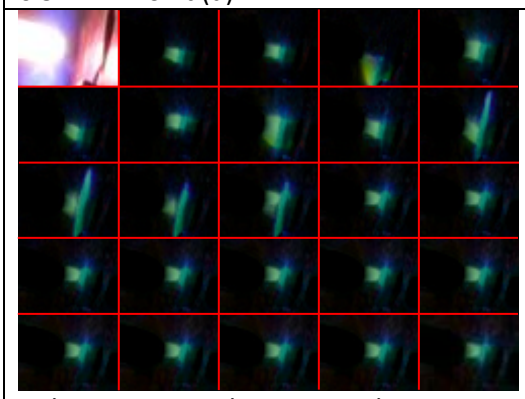	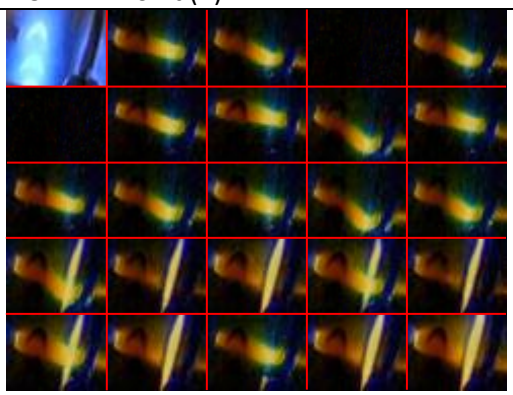
Voltage measured: 0.47±0.01 kV Current measured: 12.00±0.019 mA	Voltage measured: 1.23±0.05 kV Current measured: 8.88±0.65 mA

Table 4-3: Table showing images obtained during Figure 4-5 corresponding to a spark corona discharge. Each section represents 25 frames which is 0.50 s. The first frame at the top left corresponds to the frame just before a discharge was formed. Frames are read from left to right. Section 4.2.2 explains this in more detail.

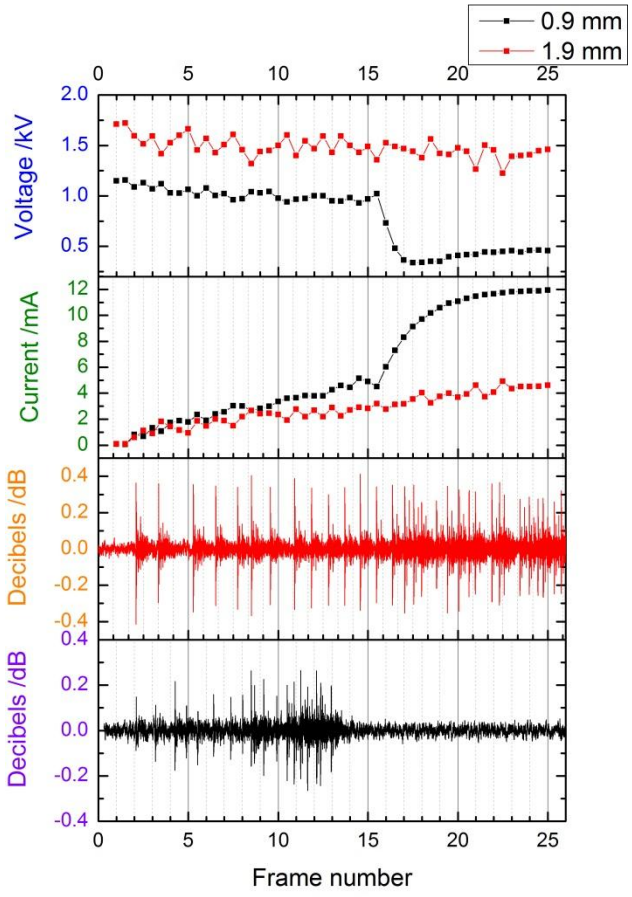

Figure 4-8: Current and voltage readings corresponding to pictures in Table 4-3 for 0.9 mm and 1.9 mm. Readings were taken at 100 samples per second.

4.3.2.4 Discussion

4.3.2.4.1 Background ionization – Point (a) and (e)

The first two points, (a) and (e) that will be discussed are the maximum current that could be passed due to the background ionization of the flame. The distance of the electrode setup for point (e) is nearly double that of point (a) and thus it was expected there should be double the amount of free electrons, assuming uniform ionization per volume. This should translate in to the current of point (e) (0.040±0.005 mA) being nearly double the current of point (a) (0.033±0.004 mA) but this is clearly not the case.

Two explanations can be given for this. The first is that, as mentioned in section 4.3.1, the resistance of the flame changes at 1.7 mm due to being at the interface between the air and flame. This would mean the distances from 1.7 mm to 1.9 mm would have less ionization per volume thus reducing the amount of electrons, which translates into less current being measured. This seems unlikely as 8 mm out of the extra 1 mm when comparing the distances between points (a) and (e), should still have the same ionization rate.

The other explanation is that the point electrode has become saturated and is unable to collect all the electrons. This could be due to either the surface area being too small or the rate that electrons are created is faster than the rate the electrodes are able to pass the electrons. To try and understand which it might be, we will first calculate the volume of electrons surrounding the point electrode and the volume of electrons between the two electrodes.

Approximating the point electrode as a cone with a radius of 0.5 mm (width of the Pt point) and height of 0.6 mm from Figure 4-1, we get an area of 9.4×10^{-7} m^2. By using the Debye radius from equation 1-13, the value of the electron temperature as 0.2 eV (2320 K)[110] and the concentration of electrons as 10^{14} m^{-3} (from Figure 1-1) we get 0.3 mm as shown in equation 4-1. It should be noted the actual concentration of electrons is most likely to be much higher given the point electrode is attracting electrons.

$$3 \times 10^{-4}\ m = \sqrt{\frac{(8.85 \times 10^{-12}\ F\ m^{-1})(1.38 \times 10^{-23}\ J\ K^{-1})(2320\ K)}{(10^{14}\ m^{-3})(1.60 \times 10^{-19}\ C)^2}} \qquad \textbf{4-1}$$

Using the area and Debye radius calculated gives an active volume of $2.8x10^{-10}$ m^3. In comparison the volume of electrons between the two electrodes can be approximated as a cylinder with 0.5 mm radius (width of the Pt point) which gives $7.8x10^{-7}$ m^3. The above assumes a uniform distribution of electrons, which is unlikely as the interface between the air and flame was around 1.7 mm. With these limitations this is around 4 orders of magnitude greater than the volume around the point electrode. In order to maintain charge neutrality and surface area not being a limiting factor, the rate that electrons must be absorbed and emitted must be 4 magnitudes greater than ion formation ~$2x10^{15}$ cm^3 s [111] (propane-air flame). Using the value of 0.040 mA and Faradays constant gives a value of $2.52x10^{13}$ as the number of electrons being passed.

4.3.2.4.2 Streamer corona discharge - Figure 4-5 Points (b) and (f)

The streamer corona discharge is an intermittent discharge and this can clearly be seen in Table 4-1. From the table it can be seen point (b) shows 5 flashes while point (f) shows only 2. For point (b) 4 of the flashes can be seen with the same width however one of them (frame 14) shows a much large width. Given how streamers form it could be possible that this was captured around the time when the streamer branches were just reaching the electrode and thus the enlarged volume. The others would have been after the branches have reached the electrode and thus collapsed into a single more stable stream. Point (f) shows two similar images in Table 4-1 with a much longer plume than that at point (b) but relatively similar width. Although the images show a colour gradient it is very difficult to explain the physical meaning behind them as discussed in section 4.2.2. What is clear is that for both distances a discharge was formed and dissipated within 0.02 s which is expected as propagation times of streamers are in the order of hundreds of nanoseconds.

The flashes observed had a regular pulse with point (b) having an interval of 0.10 s while only 0.44 s at point (f). As the electrode distance between point (b) and point (f) is nearly half, this meant in this instance halving the distance between the two electrodes caused nearly 4 times as many flashes. These flashes are in sync with spikes in the audio, current and voltage results as seen in Figure 4-6. Comparing the decibel levels of the flashes shows when the electrodes were 1.9 mm apart they were much louder than when they were 0.9 mm apart. This can be understood as the current and

voltage applied were both higher and thus more energy inputted to the system. The physical origin of the sound can be understood as the streamer channel gets heated rapidly by the sudden input of energy, but is unable to expand as fast. This causes a pressure to build up and is subsequently released as a pressure wave[112].

One possible reason why the streamers form intermittently rather than continuously is that the system is functioning as a Geiger counter. The high electric fields mean that a slight increase in ionization will cause an avalanche to form which will create a streamer event. One possible source for this increase could be from background radiation. This however seems unlikely as when the electrodes are separate by a distance of 1.9 mm, fewer events were recorded. Given that the recovery times for both distances were similar, it would be expected that a greater distance will yield more events due to a larger catchment area or at least equal if saturated.

The regular intervals lends to the idea that the pulses are due to the power supply. This seems reasonable for point (b) where the voltage curves show that once the voltage passes a certain value, a streamer event occurs. For point (f) however, the voltage remains stable at a voltage that could trigger a streamer event for a relatively long time. This seems to suggest that at least for point (f), the system is stable at the voltage applied and the streamer is externally triggered.

4.3.2.4.3 Glow corona discharge - Figure 4-5 Points (c) and (g)

In Table 4-2 both points (c) and (g) show a glow corona discharge forming. From the table point (c) forms the glow discharge from frame 12 onwards. When comparing the glow to the streamer frames, the luminous region starts further away from the electrode. This is consistent with glow discharges as they have a region of dark space known as the anode dark space[113], surrounding the electrode. The luminous region is known as the anode glow and in the table seems less bright than the streamer discharge. Unfortunately it can't be distinguished if the long straight luminous region on the plane electrode is part of the glow discharge, or due to something else, such as the area being heated which would emit a different wavelength. For point (g) the same remarks can be made however it is at frame 10 that the glow discharge appears to form. The discharge seems not as stable as the one create at point (c) as it can be seen

to transition briefly to a streamer discharge several times. The glow discharge also takes the shape of a diffused cone, in comparison to the narrow channel of the streamer discharge. This is likely due to the greater distance creating a large anode glow area.

When looking at the electrical results in Figure 4-7 for point (c), the voltage remains relatively stable throughout all the frames. The same can be said for point (g) although the voltage is consistently higher. The current for point (c) seems to oscillate around 3 mA from frame 12 onwards, which is when the glow discharge forms. For point (g) there appears to be an increase even when the glow is formed in frame 10. This shows that the glow discharge can be stabilised for a range of currents as expected from Figure 4-5.

The audio results for both points show that more than one event can be heard per frame of video. For point (c) the intervals between peaks is relatively constant while as for point (g), it is clear when the glow discharge is active more peaks can be observed. This can be seen as when the glow briefly transitions to a streamer in frames 10, 15 and 22 the time interval between peaks briefly increases. The decibel level for point (g) is always higher and can be explained due to more energy being supplied.

4.3.2.4.4 Spark corona discharge - Figure 4-5 Points (d) and (h)

Points (d) and (h) are the points were the maxmium current could be passed from Figure 4-5. This was more for point (d) than (h) and only point (d) produced a spark discharge. The spark discharge can be seen from frame 14 and onwards. In these frames the electrode shape is much more clear due to the spark heating it up. It can also been seen that the lumionous discharge in between is very small. It is interesting to note that the electrical results don't show the characteristic large increase in current and corollary decrease in voltage until frame 16. The audio results show the spark is a silent discharge and matches the visual appearance of the spark.

Point (h) shows a glow discharge being formed and has been discussed previously in section 4.3.2.4.3. The only difference that can be noticed is at higher currents the frequency of peaks in the audio results is much greater.

4.3.3 Current voltage trace in air

Using the same setup and procedure as in section 4.3.2, air was used instead of a methane flame and results shown in Figure 4-9. In the absence of the methane flame or flow, the glow and arc discharges were unable to form as shown in 4.3.2. Instead highly intermittent streamers were formed in the same manner as those in section 4.3.2.1 Table 4-4 summarises the main current ranges for the different environments used.

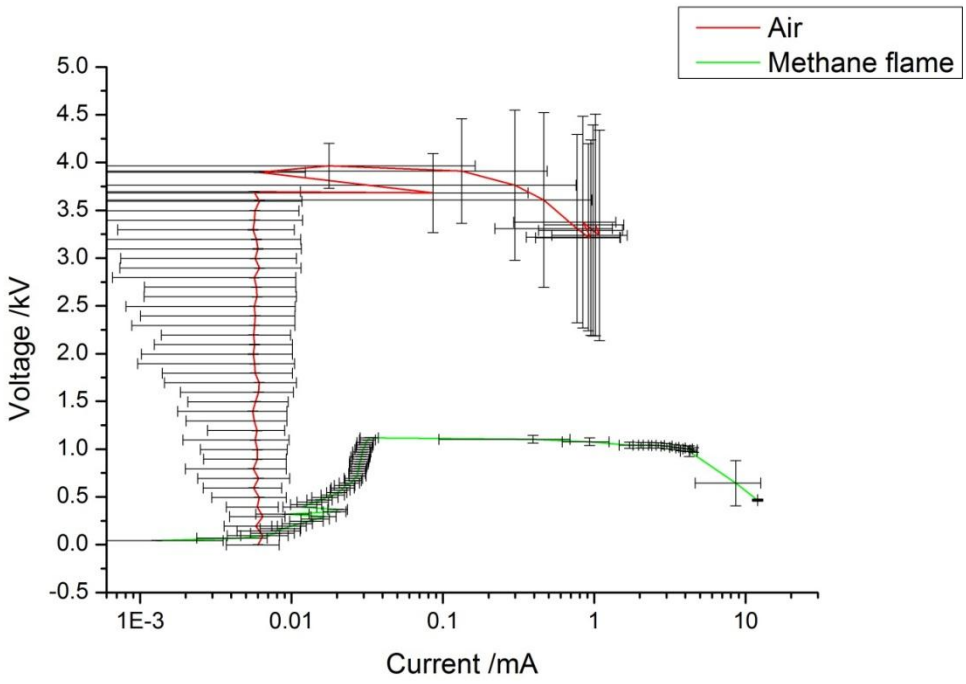

Figure 4-9: Graph comparing the log of current against voltage when using air or methane using the setup as described in Figure 4-5. Voltage steps for air was 100 V and all other variables kept the same.

From Figure 4-9 it can be seen in a methane flame the entire graph is shifted towards higher currents. This is most likely due to the relatively high amounts of background ionization provided by the flame. The next difference is that in air it appears the range of current for the curve is compressed. Instead of several magnitudes separating each discharge, here we see the same shape formed within three magnitudes of each other. It is important to note that it is only the shape that has been compressed as the glow and spark discharges weren't formed. It is likely the setup would not be able to sustain a glow discharge in air and instead a spark discharge would form next. This effect is also likely due to the relatively high amount of background ions present in the methane flame. This allows for greater charge densities to be reached at lower applied voltages.

	Current range in mA		
Discharge type	**Methane flame - 0.9 mm separation**	**Methane flame - 0.9 mm separation**	**Air - 0.9 mm separation**
Streamer corona	0.032-1.71	0.19-2.77	~0.30+
Glow corona	1.71-8.62	2.77-8.88	-
Spark corona	8.62+	-	-

Table 4-4: Table comparing discharge type formed and corresponding current ranges for a methane flame from Figure 4-5, and in air from Figure 4-9.

From Table 4-4 it can be seen the methane flame is necessary to form the glow and spark corona discharges when using the setup as described. It also shows that in air the current onset of the streamer corona is much higher. This could be due to the much larger ohmic loss over distance when comparing air to a flame.

4.3.4 Effect of distance on decrease of CO_2 at the breakdown voltage

From section 3.6.3.2 it was shown that when using a quadrapole mass spectrometer and applying a voltage using a point to plane electrode configuration, mass 44 showed a decrease from a baseline. From section 4.3.2 it has been revealed that the voltages that showed the maximum decrease in Figure 3-7 corresponds to the streamer discharge. With this in mind various distances were used while applying voltages near the onset of the streamer discharge using the same setup and results shown in Figure 4-10.

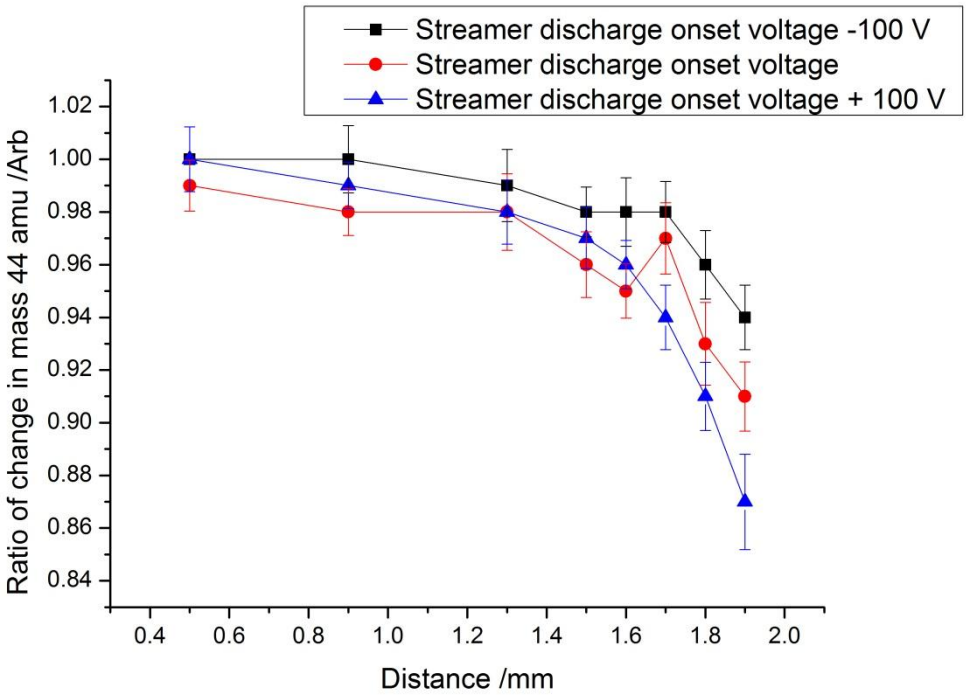

Figure 4-10: Graph showing ratio change of mass 44 against electrode separation of a Pt point from a brass plate material at voltages near the breakdown voltage. Ratios where obtain by taking the average of 20 points (taken over 50 seconds) when a voltage was applied and comparing to a baseline of 20 points before the applied field, and 20 points after. Points were taken by a mass spectrometer as described in section 2.5 was placed 10 mm from the burner top. The Pt electrode was placed 2.4 mm above the burner top sustaining a methane flame using the gas ratios of 1.0/2.0/2.3 for $CH_4/O_2/N_2$. Setup as described in section 3.7.

From Figure 4-10 it can be seen that the further apart the electrodes are, the greater the decrease in mass 44 when a streamer discharge is formed. In particular it appears that at distance beyond 1.6 mm the decrease becomes more pronounce. From section 4.3.1 it was suggested that around this distance the electrode could be at the flame and air boundary. One possible reason linking the two is that when the electrode is at the flame and air boundary, the voltage required to create a streamer discharge is much higher. It could be this higher streamer onset voltage which causes the more rapid decrease in mass 44. This relationship was also mentioned in section 3.6.3.2 and is further supported as the results from Figure 4-10 show, when an addition 100 V is applied after the streamer onset voltage mass 44 decreases even more.

4.4 Summary

The experiments in this chapter have shown that streamer, glow and spark corona discharges can be created in a methane flame. The spark discharge was observed to only form at a close distance, while in air only the streamer corona formed. It was found that the further away the point electrode was placed, the higher the apparent decrease in mass 44.

5 Investigated the Townsend regime created in a methane flame

5.1 Introduction

Chapters 3 and 4 demonstrated setups which showed the ability to decrease the amount of mass 44 which is assumed to be CO_2. This is as the only stable products of combustion of a stoichiometric methane flame are CO_2 and H_2O. This chapter will use mass spectrometry to understand the mechanism how CO_2 is being apparently decreased.

Although the results from chapter 3 and 4 show the streamer corona discharge to produce the largest change in CO_2, work on this discharge is rich in the literature involving its chemistry[114–121]. The Townsend mechanism regime on the other hand also showed the ability to remove CO_2 and as there is a lot less literature about the chemistry in this area, this regime will be explored. The setup will continue to use a Pt point to brass plate electrode configuration and a methane flame. Different flame mixtures will be used to help understand the processes going on.

If we make the assumption that CO_2 is being removed, it is important to understand the methods which the molecule can react in plasmas. Decomposition of CO_2 as shown in Reaction 5-1[122] is rate limited by the dissociation of CO_2[123] as shown in Reaction 5-2[122]. The reaction is endothermic with a rather high enthalpy. After the CO molecule is formed O can recombine to form O_2 or react with other CO_2 molecules to form more CO or O_2.

$$CO_2 \rightarrow CO + \frac{1}{2}O_2 \quad \Delta H = 2.9 \text{ eV mol}^{-1}$$

Reaction 5-1

$$CO_2 \rightarrow CO + O \quad \Delta H = 5.5 \text{ eV mol}^{-1}$$

Reaction 5-2

While the CO produced by Reaction 5-2 is harmful it can easily be converted to useful H_2 by the exothermic reaction shown in Reaction 5-3[122].

$$CO + H_2O \rightarrow CO_2 + H_2 \qquad \Delta H = -0.4 \text{ eV mol}^{-1}$$

Reaction 5-3

Of more interest is the direct conversion of CO_2 to carbon and O_2. Unfortunately the extremely high bonding energy of the CO molecule makes this kinetically difficult as shown in Reaction 5-4. A kinetically easier approach is converting the CO from Reaction 5-2 in to carbon by Reaction 5-5[122].

$$CO_2 \rightarrow C_S + O_2 \qquad \Delta H = 11.5 \text{ eV mol}^{-1}$$

Reaction 5-4

$$CO + CO \rightarrow CO_2 + C \qquad \Delta H = 5.5 \text{ eV mol}^{-1}$$

Reaction 5-5

While the creation of carbon from CO can be achieved, unfortunately carbon reacts easily with CO_2 as shown in Reaction 5-6[122]. This reaction is fast and makes it difficult to reduce CO_2 directly to carbon when there is an abundance of CO_2.

$$C + CO_2 \rightarrow CO + CO \qquad \Delta H = 0.5 \text{ eV mol}^{-1}$$

Reaction 5-6

Experimental works that attempt to use the reactions mentioned above for decomposition of CO_2 found in combustion gases[40,124] have been document in the literature using non-thermal discharges. While the above has been concerned with the removal of CO_2 by plasmas, it is important to note that NO_x[44,125–127] and SO_x[126–129] have also be treated using a similar systems.

This chapter will explore three different applied fields in a stoichiometric methane flame followed by three different oxygen rich environments with the same applied field. Finally the inert gas N_2 will be replaced by inert Ar. In order to understand the process that goes on a discussion of all the results will given at the end, rather than by section.

5.2 Experimental

5.2.1 Electrode design

As in chapter 4 a new Pt point electrode was made. This was made in the same method as described in section 3.6.2. For comparison the newly created electrode, the medium slope electrode from section 3.6 and the electrode used in chapter 4 are all shown in Figure 5-1.

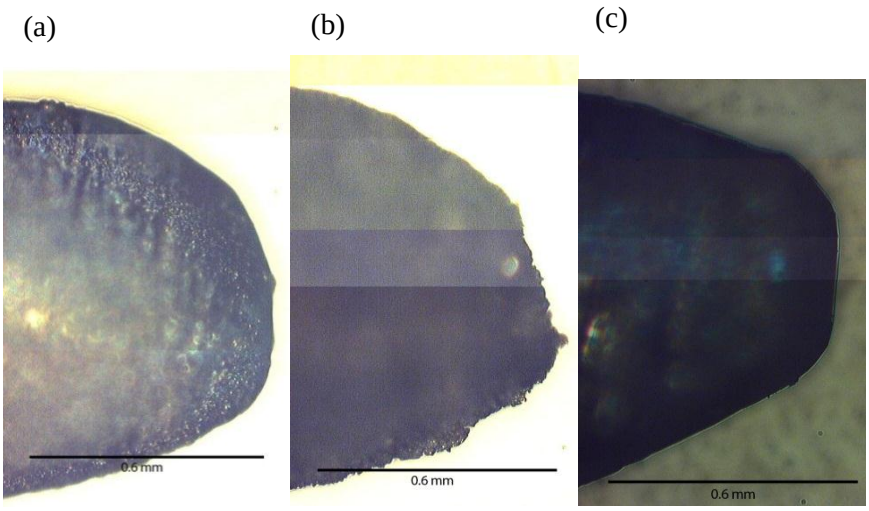

Figure 5-1: Photo of (a) the medium sloped point electrode used in section 3.6, (b) the electrode used in chapter 4 and (c) the electrode used to create the results in this chapter.

From Figure 5-1 (c) we can see the electrode created has the same over all dimensions. Visually the point is much flatter and takes the shape like a cone. As mentioned before it is hard to predict what effects the difference in geometry will have.

5.2.2 Mass spectrometry

Mass spectrometer data was used to understand the processes that occur when applying a voltage. To do this the procedure needed to be optimization to enable the maximum number of data points to be collected while balancing for completeness. From section 2.5 it can be seen that the two detectors (Faraday and SEM) was needed as the partial pressures of masses 18, 28, 32 and 44 will be too high for the SEM. While it would be easier to set the spectrometer to do a scan that goes from the smallest mass to the largest mass and switch detectors when needed, this was not done as switching detectors requires a delay and is inefficient. Instead for each scan all masses that required the SEM were taken together, followed by the masses requiring the

faraday. This meant for each scan two changes between detectors needed to be made which took around 1 s for both.

The SEM detector was tuned to make sure masses near $1x10^{-6}$ Torr would be safely in the 10^{-7} Torr range. This was done to ensure the mass spectrometer would not halt as described in section 2.5. The consequence of this is the majority of the masses were taken on the SEM. This also meant the absolute partial pressures cannot be compared between the SEM and faraday detectors without scaling. At the time of the experiments, the species that were expected were unknown which meant calibration couldn't be done. This meant relative sensitivities, fragmentation patterns and intensities were given a ±10% error as done previously in section 2.5.3.

5.3 Results

5.3.1 Stoichiometric

In this section a methane flame using the gas ratio of 1.0/2.0/2.3 for $CH_4/O_2/N_2$ respectively was used. To understand this system the quadrapole mass spectrometer as describe in section 2.5 was used to obtain mass spectrums. Previous work showed no activity in the ranges 1 – 9 amu and 51 – 200 amu with the majority of features occurring between 10 – 50 amu. With this in mind only mass spectrums from 10 – 50 amu were taken using the procedure described in section 5.2.2.

5.3.1.1 Background flame mass spectrum

A mass spectrum of the methane flame used is shown in Figure 5-2 (experimental). A scaling factor of 2 was applied to the SEM data so that the faraday data, masses 18, 28, 32 and 44 could be combined. This scaling factor was found by trial and error to provide the best fit. Using the same method of linear combination and fragmentation patterns described in section 2.5.3 a calculated mass spectrum is also shown. Table 5-1 shows the species present and their concentration. Both Figure 5-2 and Table 5-1 show the raw mass spectrum obtained which contains the signal from the background vacuum chamber. Background subtraction of the chamber was not done as experiments could last long enough such that heating of the chamber could cause

systematic errors to occur and when subtracting could not be accounted for. Instead the species from section 2.5.3 will be compared to those found in Table 5-1.

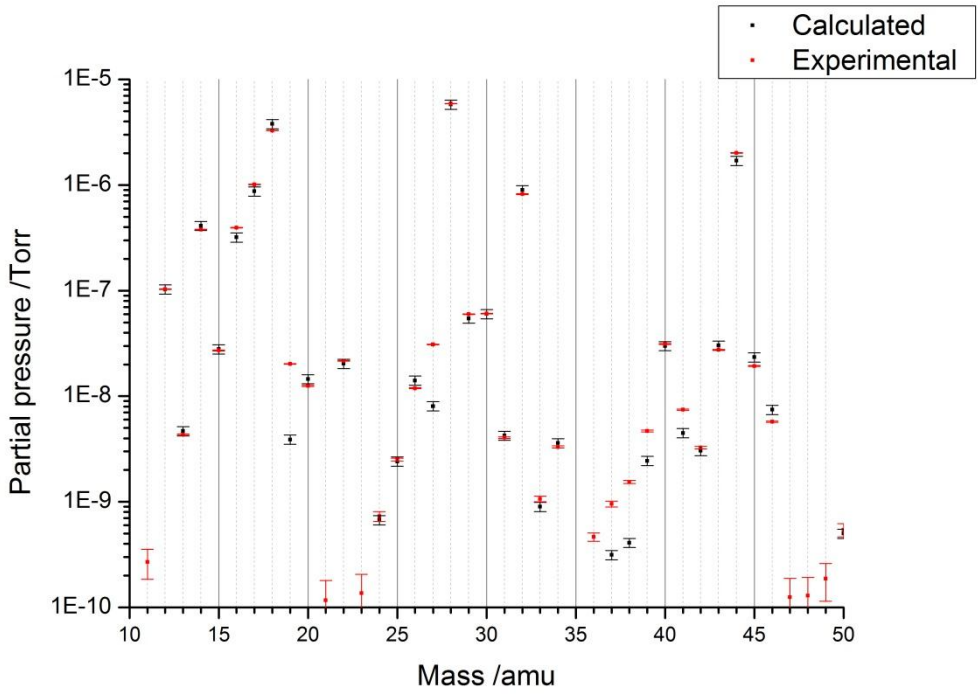

Figure 5-2: Graph showing a mass spectrum of masses 10-50 amu above the threshold of detection for a bare methane flame. A Pt point electrode was placed 1.9 mm away from a Pt plate material and 2.4 mm above the burner top, however no potential was applied. Each point is obtained by taking the average of 20 points with the full spectrum taking 50 seconds. A methane flame using the gas ratios of 1.0/2.0/2.3 for $CH_4/O_2/N_2$ was used and as described in section 2. Graph showing theoretical mass spectrum created using the fragmentation patterns in Table A-1 and the relative amounts from Table 5-1

From Figure 5-2 it can be seen the calculated mass spectrum provides a good fit however there are a few masses that are significantly outside error bars. These are masses 19, 27, 36-39 and 41. From section 2.5.3 mass 19 could either be fluorine or the tail end of the large water peak, and the differences masses 36 - 39 showed was speculated to be due to acetone. This leaves masses 27 and 41. The higher partial pressure of mass 41 can be explained as the range scanned did not include pump oils and mass 41 is a fragment of them. Mass 27 could be explained similarly to mass 19 in that there is a very large peak, mass 28 nearby.

Species	Multiplier x10^{-9} ±10%	Calibrated multiplier ±10%	Percentage of total gas measured ±10%
H_2O	38	42	35
CO_2	17	12	10
N_2	56	56	46
O_2	9	10	8.6
NO	0.6	0.5	0.41
Ar	0.3	0.25	0.21
CH_4	0.3	0.19	0.15
C_3H_6O	0.15	0.042	0.034
C_4H_{10}	0.15	0.030612	0.025
C_2H_2	0.12	0.12	0.098
C_2H_5OH	0.04	0.011111	0.0091
DP oil ppe	0.005	0.005	0.0041

Table 5-1: Relative amount of species used to produce Figure 5-2 and the calibrated amounts using Table A-2.

From Table 5-1 it can be seen there are three dominant species, H_2O, CO_2 and N_2. This is expected as H_2O and CO_2 are products of methane combustion and N_2 was used as an inert gas and found in large amounts in the air. The expected ratio of H_2O:CO_2 is 2:1 however the value obtained is 3.5±0.4:1. The high H_2O partial pressure from the vacuum chamber would bring this closer to 3.0±0.4 which is still far from the expected value. The source of the extra H_2O is likely due to droplets forming in the pre-chamber and being trapped. In particular when opening and replacing the capillary as described in section 2.5.1 droplets of water was found on the graphite feral. The ratio of N_2:O_2 is 5.3±0.8 compared to the atmosphere value of 3.9:1. This suggests there is some entrainment of air however the N_2 observed is likely from the N_2 used to stabilise the flame. The rest of the species observed are also found in the background vacuum chamber spectrum as described in section 2.5.3 and in near the same amounts so it is difficult to determine if they are from the flame or chamber. The most important observation from Table 5-1 is that the only carbon containing compound found in the percentage range is CO_2. This indicates the flame has undergone complete combustion.

5.3.1.2 Current vs Voltage trace

A current voltage trace was obtained for the methane flame and the results shown in Figure 5-3. This was done as the voltages which correspond to the Townsend regime can change depending on the point electrode geometry.

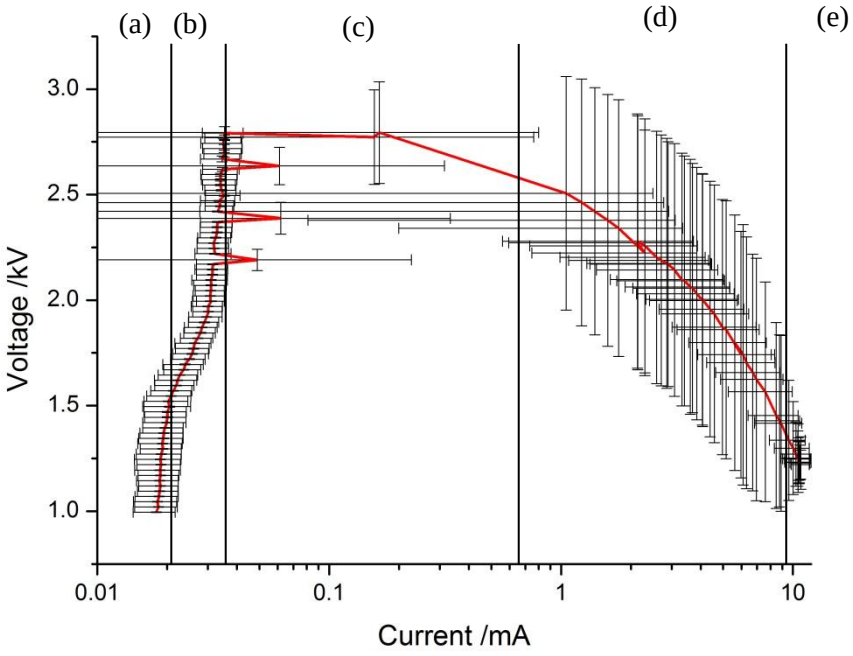

Figure 5-3: Graph showing log of current against voltage when a Pt point is placed 1.9 mm away from a Pt plate material. Each point represents 200 data points obtained by holding the set potential for 2 seconds. Steps were made in 25 V from 1000-4000 V. Electrodes were placed 2.4 mm above the burner top sustaining a methane flame using the gas ratios of 1.0/2.0/2.3 for $CH_4/O_2/N_2$. Setup as described in section 2 and 3.6.

Figure 5-3 illustrates the five regions as described in section 3.6.3.1, region (a) background ionization, (b) Townsend mechanisms, (c) streamer corona discharge, (d) glow corona and (e) spark discharges respectively. Using the figure, three applied voltages 1.5 kV, 2.00 kV and 2.50 kV found in region (b) were chosen to be further explored using mass spectrometry.

5.3.1.3 Mass spectrometry results due to an applied electric field

As mentioned earlier, no activity was seen in the ranges from 1 – 9 amu and 51 -200 amu. Only the spectrums from 10 – 50 amu were taken using the procedure described in section 5.2.2 and will be shown.

In order to analyse the effects of applying an electric field on the mass spectrum obtained, how each mass changes will be examined. From this we will obtain possible species present that can then be used with linear combination and their fragmentation pattern as in section 2.5.3 and 5.3.1.1. By looking at the changes the background flame and vacuum chamber response is removed which should make the analysis easier.

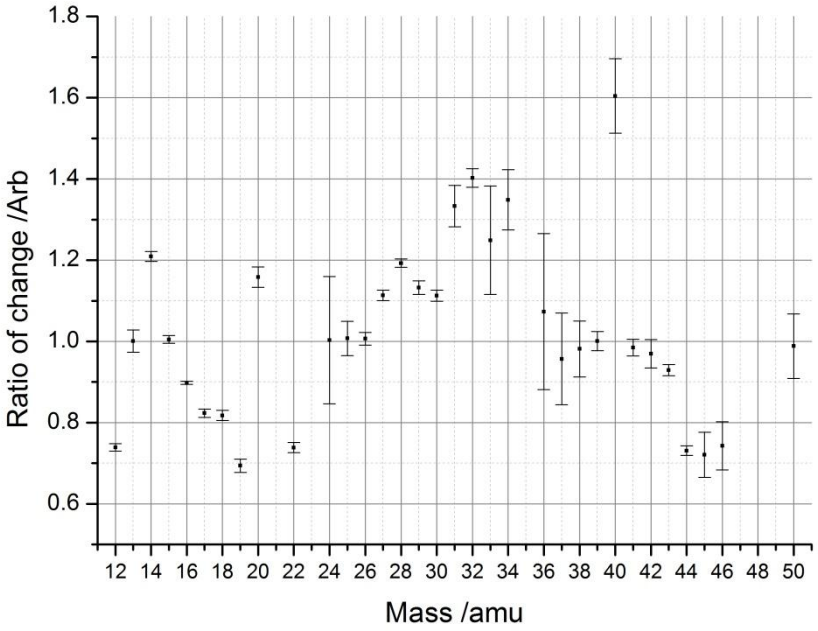

Figure 5-4: Graph showing ratio of change for masses 10-50 amu above the threshold of detection. Ratios where obtain by taking the average of 20 points (taken over 50 seconds) when a 2.5 kV field was applied and comparing to a baseline of 20 points before the applied field and 20 points after. The field was created by a Pt point placed 1.9 mm away from a Pt plate material and 2.4 mm above the burner top as in section 3.6. A methane flame using the gas ratios of 1.0/2.0/2.3 for $CH_4/O_2/N_2$ was used and as described in section 2.

In Figure 5-4 we notice some masses show a change (have a ratio other than 1) while others show no change (have a ratio of 1) when a 2.5 kV field was applied. In order to turn these changes into meaningful information all masses that showed the same change where grouped together. The reasons for this is that although each species has a different fragmentation pattern, by using the ratio change, all masses relating to the

same species will change by the same amount. Table A-1 can then be used to check these masses do correspond to the same species. For example masses 12, 22, 44, 45, 46 all show a ratio change of 0.73, from Table A-1 it is most likely that these are the fragmentation of CO_2. The final identification of all the masses is shown in Table 5-2.

Voltage set in kV	1.50	2.00	2.50	
Voltage measured in kV	1.495±0.002	1.996±0.002	2.496±0.002	
Current measured in mA	0.024±0.004	0.035±0.005	0.040±0.005	
Mass in amu	**Ratio change from baseline**			**Species**
12	0.97±0.01	0.85±0.00	0.74±0.01	CO_2
22	0.97±0.01	0.85±0.01	0.74±0.01	
44	0.97±0.01	0.85±0.01	0.73±0.01	
45	0.96±0.01	0.84±0.03	0.72±0.06	
46	0.96±0.02	0.84±0.03	0.74±0.06	
31	1.01±0.03	1.17±0.03	1.33±0.05	O_2
32	1.03±0.02	1.21±0.02	1.40±0.02	
33	1.02±0.10	1.13±0.10	1.25±0.13	
34	1.03±0.03	1.18±0.04	1.35±0.07	
14	1.01±0.01	1.11±0.01	1.21±0.01	N_2
28	1.01±0.00	1.10±0.01	1.19±0.01	
17	0.98±0.01	0.91±0.01	0.82±0.01	H_2O
18	0.98±0.01	0.91±0.01	0.82±0.01	
40	1.04±0.01	1.32±0.04	1.60±0.09	Ar
16	0.98±0.01	0.94±0.00	0.90±0.00	$H_2O + CO_2 + O_2$
29	1.00±0.01	1.07±0.01	1.13±0.02	$CO_2 + N_2$
20	1.01±0.01	1.09±0.01	1.16±0.02	H_2O + Ar
30	0.99±0.01	1.05±0.01	1.11±0.01	NO*
19	0.97±0.01	0.84±0.01	0.69±0.02	H_2O*
27	1.00±0.01	1.05±0.01	1.11±0.01	N_2*
43	0.99±0.01	0.96±0.01	0.93±0.01	C_3H_6O

Table 5-2: Identification of masses from Figure 5-4 (used to create the 3rd column) to correlate masses in amu to species. Red indicates a decrease of the species, green indicates an increase of the species while orange indicates the parent mass. Experimental conditions as in Figure 5-4 with columns 1 and 2 obtained by applying a 1.50 kV and 2.00 kV field respectively. Assignment of starred masses are explained in the text.

In Table 5-2 it can be seen that mass 31 shows a similar change to that of 32 (within error) but is not in Table A-1 as an expected fragment of O_2. It has been assigned to O_2 as although the quadrapole is rated as having 1 amu resolution, the 32 peak is significantly large and the signal may have bled over. This is supported by the fact that the absolute change measured is small, 3.29×10^{-10} Torr when compared to 3.29×10^{-7} Torr from the mass 32 peak.

While most of the fragments of the species of CO_2, O_2, N_2 and H_2O show a consistent ratio change with themselves, several of their expected fragments do not. These are shown as masses 16, 29 and 20. By using the fragmentation values in Table A-1 and other masses taken on the SEM, expected partial pressures can be obtained for masses 20 and 29. For mass 20 with the assumption that it is a combination of only H_2O and Ar, a partial pressure of $1.08x10^{-10}$ Torr is expected using mass 17 and mass 40 to represent H_2O and Ar respectively. This can be compared to a measured response of $9.46x10^{-10}$ Torr. The large error is suspected to be due to the difference in scaling, Ar is scaled by 6.8 while H_2O by 0.014 (2 orders of magnitudes different). The component of mass 20 from Ar is $1.32x10^{-9}$ Torr near the measured response. Using the same method for mass 29, $1.90x10^{-9}$ Torr is expected using mass 12 and mass 14 as estimators of CO_2 and N_2 respectively which is near the measured value of $3.78x10^{-9}$ Torr. Mass 16 can be a combination of two species that move down, H_2O and CO_2 and one that moves up O_2. As the overall movement is downwards this suggests the amount of H_2O and CO_2 that decreases is more than the amount of O_2 that increases.

The remaining peaks of masses 30, 19 and 27 were determined by noting their behaviour in other experiments. Mass 30 and 27 has been identified to be nitrogen containing compounds as their values changed in tandem, though not to the same ratio as N_2 when the N_2 gas flows were changed. Mass 19 was identified as H_2O, and was done by observing its movement with mass 18 (H_2O) in previous un-optimised setups. In previous experiments involving fast changes (turning the applied voltage on and off rapidly), mass 18 would show a delay in its response (likely due to condensation), mass 19 and mass 17 would mirror this movement while all others would not. The reason for why masses 19 and 27 don't show the same ratio is unknown but may have something to do with their parent peaks, H_2O and N_2 being extremely large and only 1 amu apart.

The final mass that remains is mass 43 typically assigned to acetone. It can be seen that it decreases when a voltage is applied however this is unexpected. This is as any acetone used would be in the vacuum system and should be invariant to experimental conditions.

From Table 5-2 it can be seen only 7 unique species are present by the time the sample reaches the detector. These are H_2O, CO_2, N_2, O_2, NO, Ar and C_3H_6O. Using these species and their fragmentation pattern from Table A-1 we will use linear combination

to create a calculated mass spectrum. The values used are shown in Table 5-3 and the resulting mass spectrum along with the experimental values for when a 2.5 kV voltage is applied is shown in Figure 5-5.

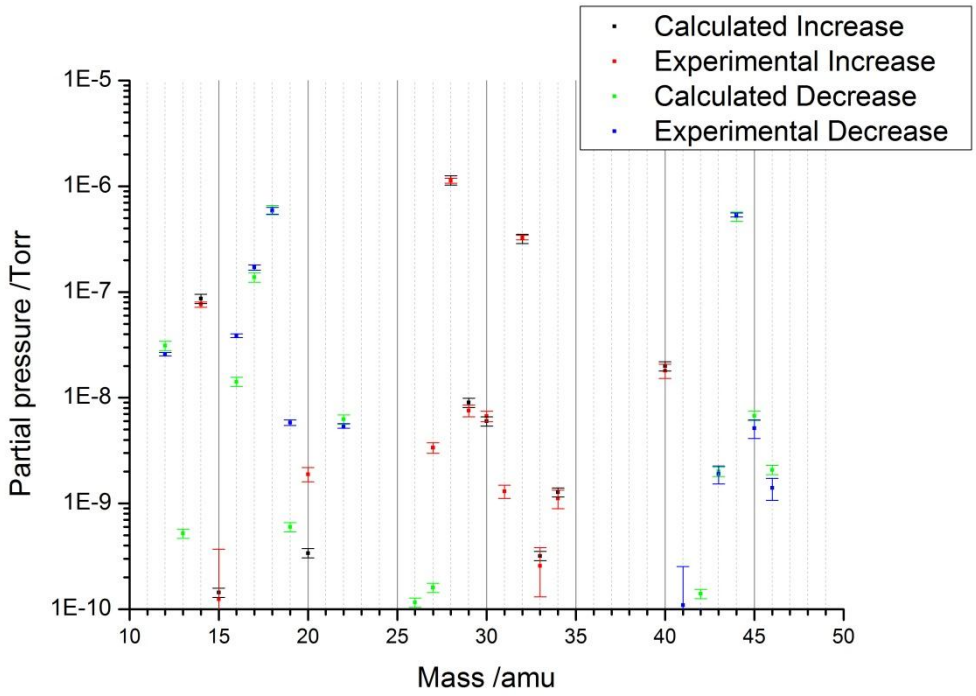

Figure 5-5: Graph showing mass spectrums of the absolute changes observed for the increase and decrease of masses 10 – 50 amu when a voltage of 2.5 kV was applied. Calculated values were obtained using the fragmentation patterns in Table A-1 and the relative amounts from Table 5-3. Experimental conditions are from Figure 5-4.

From Figure 5-5 we see the calculated mass spectra approximates the experimental spectrums well aside from a few masses. These are masses 16 and 19 for those that decrease and 20, 27 and 31 for those that increase. These are also the same masses found in Table 5-2 that do not show the same ratio change as their other fragments. Previous explanations can account for masses 19, 27 and 31 which suggests their very large parent peak that is only 1 amu away caused measurement error. This explanation is consistent with the observed response as the experimental values are always larger than calculated values. Finally this leaves a greater experimental decrease in mass 16 and a greater experimental increase in mass 20. The reasons for these two masses showing a higher experimental response is unknown.

From section 5.1 it can be seen that CO is an important species in the decomposition of CO_2. Unfortunately the mass spectrometer could only resolve 1 amu and both CO and

N_2 have a mass of 28 thus other means must be used to distinguish them. This can be done using mass 12 which is due to a carbon fragment for small carbon containing species such as CO_2, and CO. It is important to note that in Figure 5-5 mass 12 was predicted within error bar. Table 5-2 also builds confidence that the only small carbon containing species observed to change is CO_2. To further support the conclusion that CO isn't present are masses 14 and 28. These masses belong to N_2 and Figure 5-5 and Table 5-2 shows a high level of confidence that the entire signal from mass 28 is from N_2.

The same observations made above for Figure 5-5 can also be made when a 2.0 kV or 1.5 kV electric field was applied. These results are shown in Figure A-3 and Figure A-4 respectively and Table 5-3 shows the multipliers used.

	Multiplier x10^{-9} ±10%			**Calibrated multiplier ±10%**			**Percentage of total gas measured ±10%**		
	Voltage set			**Voltage set**			**Voltage set**		
Species	1.5	2.0	2.5	1.5	2.0	2.5	1.5	2.0	2.5
H_2O	-0.8	-3.4	-6	-0.889	-3.778	-6.667	41	27	25
CO_2	-0.6	-3	-5.2	-0.429	-2.143	-3.714	20	15	14
N_2	0.6	6	12	0.600	6.000	12.000	28	42	46
O_2	0.2	1.8	3.2	0.233	2.093	3.721	11	15	14
NO	-0.004	0.03	0.06	-0.003	0.025	0.050	0.15	0.18	0.19
Ar	0.014	0.1	0.2	0.012	0.083	0.167	0.54	0.59	0.63
C_3H_6O	-0.004	-0.012	-0.02	-0.001	-0.003	-0.006	0.051	0.024	0.021

Table 5-3: Relative amount of species used to produce Figure 5-5, Figure A-3 and Figure A-4 and their respective calibrated amounts using Table A-2.

From Table 5-3 it can be seen that when a 1.5 kV electric field was applied, the values obtained for the percentage change of species vary significantly compared to when a 2.0 kV or 2.5 kV was applied. The reason for this is that the experimental values have large error bars compared to the change measured as seen in Table 5-2. This meant the calculated values had a wide range that would still produce a good fit and can be seen in Figure A-4. The other two voltages used, 2.0 kV and 2.5 kV both show the same vales for the percentage of total gas measured. This meant the composition of the resulting change in gas due to an applied electric field was the same. It can be seen from the calibrated multiplier values that 1.9±0.3 times more gas is changed when comparing the two voltages.

The calibrated values seem to show that more gas in drawn when the electric field is applied as the total amount of gas that increases is more than those that decreases. A possible reason for this is that vacuum systems are known to pump away different gases at different rates. These rates are used when calculating the conductance of a vacuum system and are shown in Table A-3. Using the conversion factors for a molecular and laminar flow we obtain Table 5-4 which shows the total amount of gas that the vacuum pumped away.

	Molecular flow ±10%		**Laminar flow ±10%**	
	2.5	2.0	2.5	2.0
Decrease	11.4	6.5	16.2	9.2
Increase	15.5	8.0	15.4	7.9

Table 5-4: Table showing the total amount of gas that increases and decreases when normalized to air.

In the vacuum system used the gas undergoes molecular flow through the capillary then laminar flow onwards. From Table 5-4 it can be seen once normalised to air the amount of gas that increases is near the amount that decreases assuming molecular or laminar flow as expected.

5.3.2 Effect of extreme oxygen rich ratios

In order to further understand the changes in mass spectra due to an applied electric field, oxygen rich ratios were examined. Fuel rich ratios were explored but as they changed the size of the flame, it was hard to make meaningful comparisons. By using an oxygen rich ratio this meant the extra oxygen would have nothing to combust with and thus only the effect of the extra oxygen would be observed.

5.3.2.1 Background flame mass spectrum

To confirm that the extra oxygen used did not create additional species, a mass spectrum of the methane flame with extra oxygen used is shown in Figure 5-6 (experimental). Similar to section 5.3.1.1 linear combination was used to produce Table 5-5 to show what species are present.

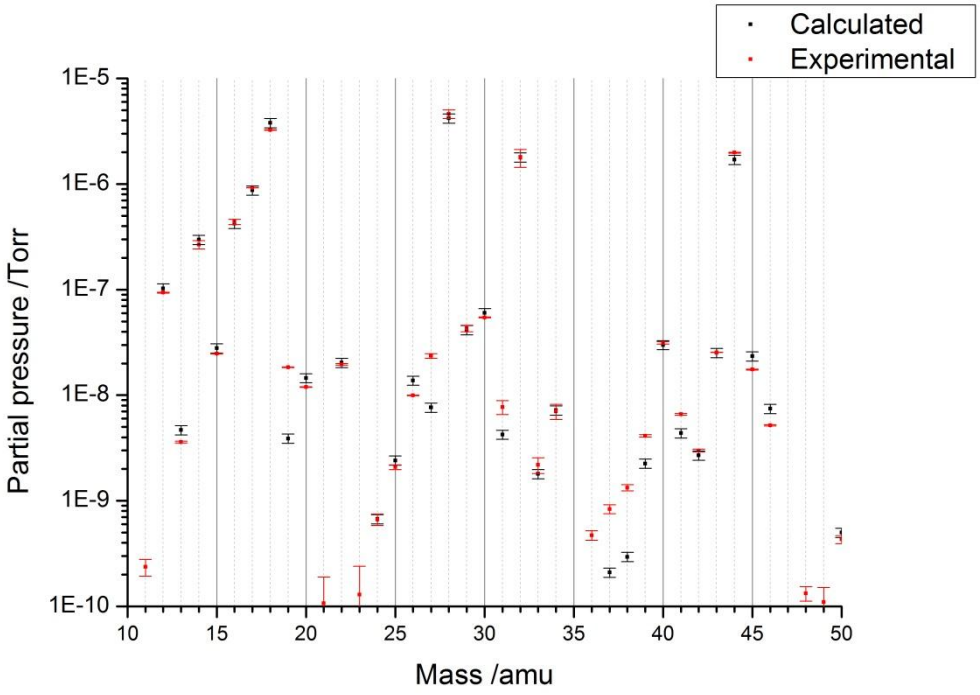

Figure 5-6: Graph showing a mass spectrum of masses 10-50 amu above the threshold of detection for a bare methane flame with excess oxygen. A Pt point electrode was placed 1.9 mm away from a Pt plate material and 2.4 mm above the burner top, however no potential was applied. Each point is obtained by taking the average of 20 points with the full spectrum taking 50 seconds. A methane flame using the gas ratios of 1.0/2.8/1.5 for $CH_4/O_2/N_2$ was used and as described in section 2. Graph showing theoretical mass spectrum created using the fragmentation patterns in Table A-1 and the relative amounts from Table 5-5.

From Figure 5-6 it can be seen the calculated and experimental mass spectrums show the same good fit as in the previous background flame spectrum. The masses that deviate significantly outside error bars are the same as Figure 5-2 and thus the same explanations can be used.

Species	Multiplier x10^{-9} ±10%	Calibrated multiplier ±10%	Percentage of total gas measured ±10%
H_2O	38	42	36
CO_2	17	12	10
N_2	40	40	34
O_2	18	21	18
NO	0.6	0.50	0.43
Ar	0.3	0.25	0.21
CH_4	0.3	0.19	0.16
C_3H_6O	0.1	0.028	0.024
C_4H_{10}	0.15	0.031	0.026
C_2H_2	0.12	0.12	0.10
C_2H_5OH	0.04	0.011	0.0095
DP oil ppe	0.005	0.005	0.0043

Table 5-5: Relative amount of species used to produce Figure 5-5 and the calibrated amounts using Table A-2.

Comparing Table 5-3, which was obtained under stoichiometric conditions, with Table 5-5, it is clear no extra species were found when the methane flame was burnt with excess oxygen. The amounts of the species observed were the same aside from N_2 and O_2. When excess oxygen was used a calibrated amount of 20 and 40 was obtained for O_2 and N_2 respectively. This is compared to 10 and 56 under stoichiometric conditions. These differences were expected given the amount of O_2 was increased and N_2 decreased. It is interesting to note the sum of these two species were nearly the same, 61 and 66 for excess oxygen and stoichiometric conditions respectively.

5.3.2.2 Mass spectrometry results due to an applied electric field

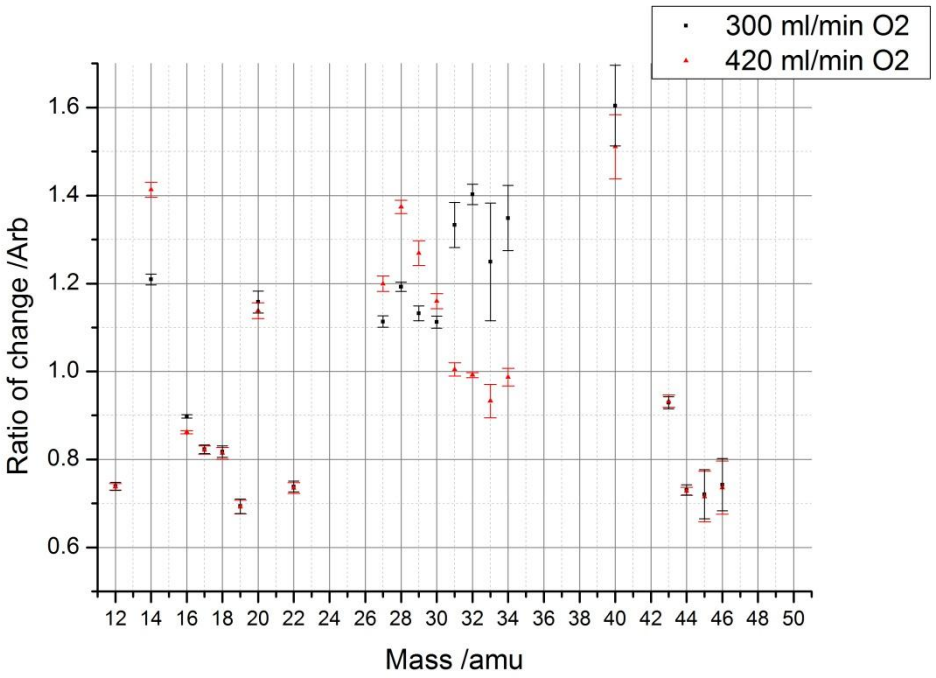

Figure 5-7: Graph showing ratio of change for masses 10-50 amu above the threshold of detection. Ratios where obtain by taking the average of 20 points (taken over 50 seconds) when a 2.5 kV field was applied and comparing to a baseline of 20 points before the applied field and 20 points after. The field was created by a Pt point placed 1.9 mm away from a Pt plate material and 2.4 mm above the burner top as in section 3.6. Two gas ratios of 1.0/2.0/2.3 and 1.0/2.8/1.5 for $CH_4/O_2/N_2$ was used and as described in section 2.

From Figure 5-7 it can clearly be seen that the changes in some masses when an electric field is applied are independent of both O_2 and N_2. It appears that these masses are only the ones that show a decrease. Table 5-6 has been produced using the same method to identify all the different species as in section 5.3.1.3 regarding the changes observed in a stoichiometric flame due to the applied electric field.

N_2 flow in ml min^{-1}	350	290	230	
O_2 flow in ml min^{-1}	300	360	420	
Voltage set in kV	2.50	2.50	2.50	
Voltage measured in kV	2.50±0.00	2.49±0.03	2.50±0.01	
Current measured in mA	0.04±0.01	0.04±0.11	0.03±0.03	
Mass in amu	**Ratio change from baseline**			**Species**
12	0.74±0.01	0.74±0.01	0.74±0.01	CO_2
22	0.74±0.01	0.73±0.01	0.73±0.01	
44	0.73±0.01	0.73±0.01	0.73±0.01	
45	0.72±0.06	0.72±0.05	0.72±0.06	
46	0.74±0.06	0.74±0.05	0.74±0.06	
31	1.33±0.05	1.12±0.02	1.00±0.02	O_2
32	1.40±0.02	1.11±0.01	0.99±0.01	
33	1.25±0.13	1.02±0.06	0.93±0.04	
34	1.35±0.07	1.10±0.02	0.99±0.02	
14	1.21±0.01	1.30±0.01	1.41±0.02	N_2
28	1.19±0.01	1.28±0.01	1.37±0.02	
17	0.82±0.01	0.82±0.01	0.82±0.01	H_2O
18	0.82±0.01	0.82±0.01	0.81±0.01	
40	1.60±0.09	1.56±0.07	1.51±0.07	Ar
16	0.90±0.00	0.88±0.00	0.86±0.00	H_2O + CO_2 + O_2
29	1.13±0.02	1.20±0.02	1.27±0.03	CO_2 + N_2
20	1.16±0.02	1.15±0.02	1.14±0.02	H_2O + Ar
30	1.11±0.01	1.13±0.02	1.16±0.02	NO*
19	0.69±0.02	0.69±0.02	0.69±0.02	H_2O*
27	1.11±0.01	1.16±0.01	1.20±0.02	N_2*
43	0.93±0.01	0.93±0.01	0.93±0.01	C_3H_6O

Table 5-6: Identification of masses from Figure 5-7 (used to create 3rd column) to correlate masses in amu to species. Red indicates a decrease of the species, green indicates an increase of the species while orange indicates the parent mass. Experimental conditions as in Figure 5-7 with columns 1, 2 and 3 obtained by changing the amount of O_2 and N_2. For all gas ratios a 2.50 kV field was applied.

From Table 5-6 it can be seen that it is the large changes in CO_2 and H_2O that are invariant against changes in N_2 or O_2. It can also be seen that the negative change in O_2 due to the applied electric field, decrease with higher flows of O_2. The opposite can be said for N_2. Interestingly the amount of Ar observed seems to decrease with greater flows of O_2. Like the changes observed in a stoichiometric flame, the only species present were H_2O, CO_2, N_2, O_2, NO, Ar and C_3H_6O. Using these species and multiplier values from Table 5-7, linear combination was applied to produce Figure 5-8 and Figure A-5 for flow rates of 420 and 360 O_2 ml min^{-1} respectively.

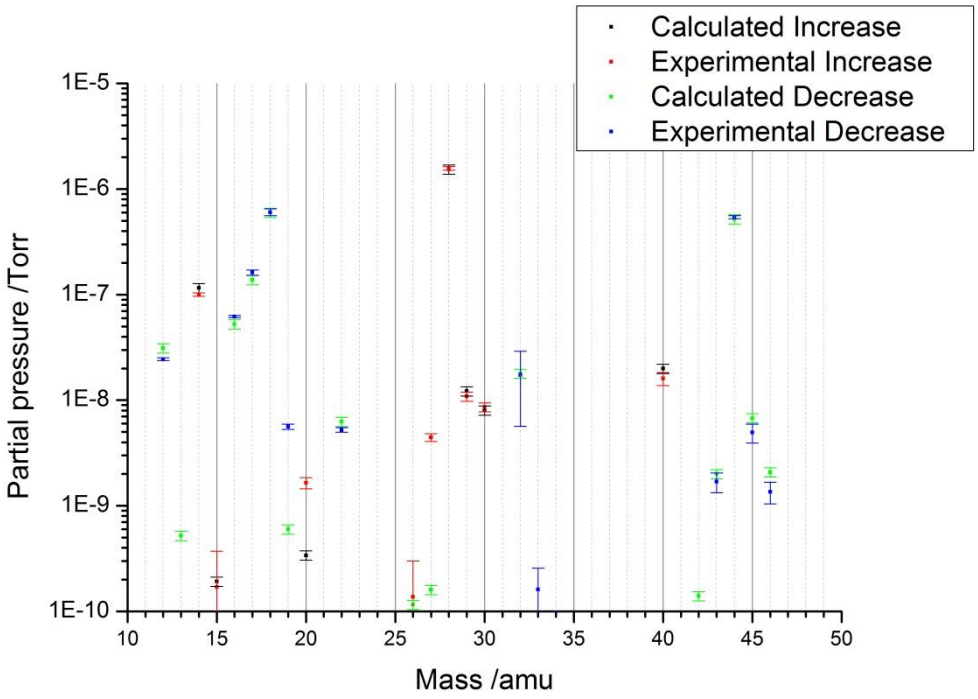

Figure 5-8: Graph showing mass spectrums of the absolute changes observed for the increase and decrease of masses 10 – 50 amu when a voltage of 2.5 kV was applied. Calculated values were obtained using the fragmentation patterns in Table A-1 and the relative amounts from Table 5-7. Experimental conditions are from Figure 5-7.

It can be seen from Figure 5-8 the mass spectrum obtain experimentally fits well with the calculated one produced by Table 5-7. There are some masses that lie outside error bars and these have been discussed in section 5.3.1.3 regarding the changes in stoichiometric conditions.

	Multiplier x10^{-9} ±10%			Calibrated multiplier ±10%			Percentage of total gas measured ±10%		
	O_2:N_2 flow in ml min^{-1}			O_2:N_2 flow in ml min^{-1}			O_2:N_2 flow in ml min^{-1}		
Species	300: 350	360: 290	420: 230	300: 350	360: 290	420: 230	300: 350	360: 290	420: 230
H_2O	-6	-6	-6	-6.667	-6.667	-6.667	25	26	25
CO_2	-5.2	-5.2	-5.2	-3.714	-3.714	-3.714	14	15	14
N_2	12	13	16	12.000	13.000	16.000	46	51	60
O_2	3.2	1.5	-0.18	3.721	1.744	-0.209	14	6.9	0.78
NO	0.06	0.08	0.06	0.050	0.067	0.050	0.19	0.26	0.19
Ar	0.2	0.18	0.2	0.167	0.150	0.167	0.63	0.59	0.62
C_3H_6O	-0.02	-0.02	-0.02	-0.006	-0.006	-0.006	0.021	0.022	0.021

Table 5-7: Relative amount of species used to produce Figure 5-5, Figure 5-8 and Figure A-5 and their respective calibrated amounts using Table A-2.

From Table 5-7 it can be seen the only changes observed are in the amounts of N_2 and O_2. Adding the calibrated values for these two species gives 15.7, 14.7 and 15.8 for the flow rates of 300, 360 and 420 O_2 ml min^{-1} respectively. This suggests the two are linked in some way. It is important to note that no additional species were found and the decrease in H_2O and CO_2 remained the same. A similar observation that the total amount of gas detected increased when an electric field was applied. Table 5-8 shows the amounts normalised to the conductance of air.

	Molecular flow ±10%			Laminar flow ±10%		
	O_2:N_2 flow in ml min^{-1}			O_2:N_2 flow in ml min^{-1}		
	300:350	360:290	420:230	300:350	360:290	420:230
Decrease	16.2	16.2	16.4	16.2	16.2	16.4
Increase	15.5	14.7	16.0	15.4	14.6	16.0

Table 5-8: Table showing the total amount of gas that increases and decrease when normalized to air.

From Table 5-8 it can be seen that the total amount of gas that increase is near the amount that decrease for the three different environments of excess oxygen.

5.3.3 Methane flames balanced in argon

In order to examine the effect nitrogen has on the discharge, argon was used as a substitute. First the effect on the current voltage trace will be shown followed by mass spectrometry data.

5.3.3.1 Current vs Voltage trace

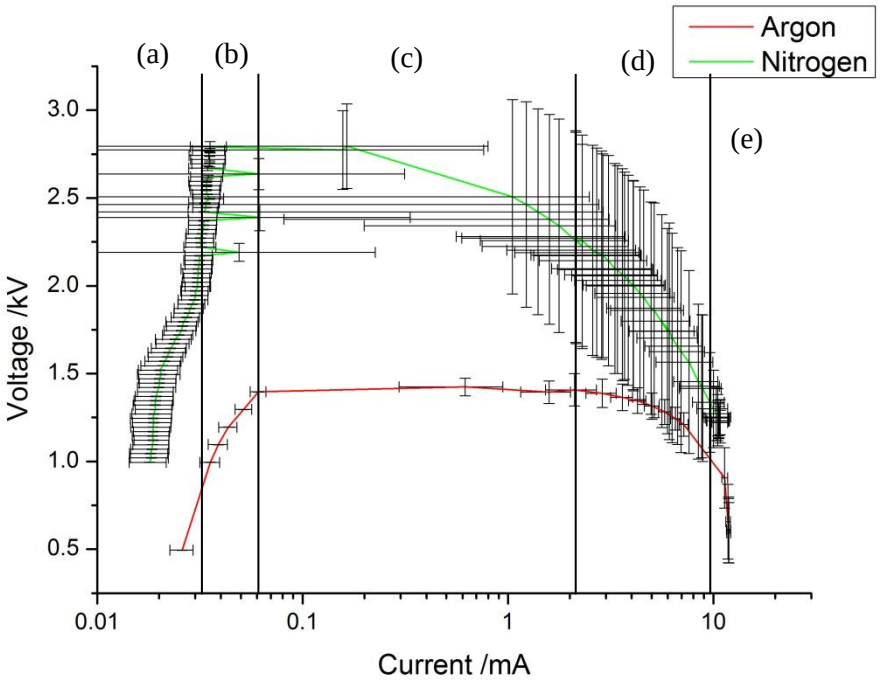

Figure 5-9: Graph showing log of current against voltage when a Pt point is placed 1.9 mm away from a Pt plate material as in section 3.6. Each point represents 200 data points obtained by holding the set potential for 2 seconds. Steps were made in 25 V from 1000-4000 V. Electrodes were placed 2.4 mm above the burner top sustaining a methane flame using the gas ratios of 1.0/2.0/2.3 for CH_4/O_2/Ar. Setup as described in section 2. Nitrogen values as found from Figure 5-3.

From Figure 5-9 it can be seen the breakdown voltage occurs much earlier in argon than nitrogen. Another feature is the plateau region before the creation of a spark is much flatter. Lastly the stabilisation voltage needed for a spark is much lower. The overall result being only lower applied potentials could be sustained (< 1.5 kV).

Similarly to the flame using nitrogen in section 5.3.1, Figure 5-9 has been divided into 5 regions (a), (b), (c), (d) and (e) corresponding to the background ionization, Townsend mechanism region, streamer corona, glow corona and spark corona discharges respectively. Two different applied voltages in the Townsend mechanism region (1.2 kV and 1.4 kV) were picked to perform mass spectrometry on.

5.3.3.2 Mass spectrometry results due to an applied electric field

Mass spectrums from 10 – 50 amu was taken for the argon – methane flame and shown in Figure 5-10.

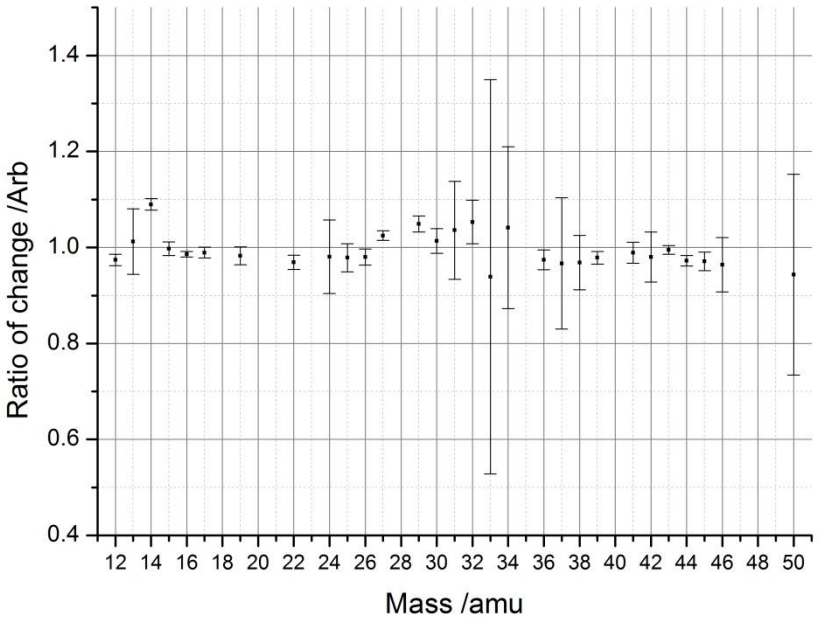

Figure 5-10: Graph showing ratio of change for masses 10 - 50 amu excluding masses 18, 28, 40, 20 above the threshold of detection. Ratios where obtain by taking the average of 50 points (taken over 50 seconds) when a 1.40 kV field was applied, and comparing to a baseline of 50 points before the applied field and 50 points after. The field was created by a Pt point placed 0.9 mm away from a Pt plate material and 2.4 mm above the burner top as in section 3.6. A methane flame using the gas ratios of 1.0/2.0/2.3 for $CH_4/O_2/Ar$ was used and as described in section 2.

The same method as described in section 5.3.1.3 was used to analyse the mass spectrums obtained. It is important to note that the ratio changes were much smaller than in nitrogen and the appearance of mass 36. Table 5-9 shows the full list of masses that changes and their corresponding species assignment along with a column from Table A-2 for easy comparisons.

Inert gas used	Argon		Nitrogen	
Voltage set in kV	1.20	1.40	1.50	
Voltage measured in kV	1.20±0.00	1.40±0.00	1.495±0.002	
Current measured in mA	0.04±0.00	0.06±0.01	0.024±0.004	
Mass in amu	**Ratio from baseline**			**Species**
12	0.99±0.01	0.97±0.01	0.97±0.01	
22	0.99±0.01	0.97±0.01	0.97±0.01	
44	0.99±0.01	0.97±0.01	0.97±0.01	CO_2
45	0.99±0.02	0.97±0.02	0.96±0.01	
46	1.00±0.05	0.96±0.06	0.96±0.02	
31	1.00±0.10	1.04±0.10	1.01±0.03	
32	1.00±0.05	1.05±0.05	1.03±0.02	O_2
33	0.94±0.38	0.94±0.41	1.02±0.10	
34	1.00±0.16	1.04±0.17	1.03±0.03	
14	1.00±0.01	1.09±0.01	1.01±0.01	N_2
28		1.17±0.06*	1.01±0.00	
17	0.99±0.01	0.99±0.01	0.98±0.01	H_2O
18		0.99±0.01*	0.98±0.01	
40		0.95±0.02*	1.04±0.01	
39	0.99±0.01	0.98±0.01		Ar
36	0.99±0.02	0.97±0.02		
16	0.99±0.01	0.99±0.01	0.98±0.01	$H_2O + CO_2 + O_2$
29	0.99±0.02	1.05±0.02	1.00±0.01	$CO_2 + N_2$
20			1.01±0.01	CO_2 + Ar
30	1.00±0.03	1.01±0.03	0.99±0.01	NO
19	0.99±0.02	0.98±0.02	0.97±0.01	H_2O
27	0.99±0.01	1.02±0.01	1.00±0.01	N_2
43	0.99±0.01	0.99±0.01	0.99±0.01	C_3H_6O

Table 5-9: Identification of masses from Figure 5-10 (used to create the 2nd column) to correlate masses in amu to species. Red indicates a decrease of the species, green indicates an increase of the species, orange indicates the parent mass, while blue represents a change in sign when compared to a nitrogen flame. Asterisked mass 18, 28 and 40 are explained below. Experimental conditions as in Figure 5-10 with columns 1 and 2 obtained by applying a 1.20 kV and 1.40 kV field respectively. Column 3 is obtained from Table 5-2.

The Ar column in Table 5-9 has mass 20 missing due to its partial pressures being too high, therefore needed to be taken on the faraday detector. While masses 28, 18 and 40 also needed to be taken on the faraday, they were taken during a different experiment however mass 20 was missed out. It should be noted that the voltage applied in the experiment was 1.5 kV and not 1.4 kV as in the table. For comparison mass 44 showed a change of 0.95±0.02 when 1.5 kV was applied compared to the table value of 0.97±0.01 when 1.4 kV. While the values cannot be used, the direction of change can be used to link them to their respective fragments.

Two new masses, 36 and 39 were also observed to show a change when applying a voltage and these were assigned to argon. Mass 36 being a fragment as seen from Table A-1, and 39 likely being due to bleed over from the large 40 peak from argon.

When comparing the effect of the inert gas on the changes in ratios for the species identified, it can be seen that only argon shows a difference in sign. While a nitrogen balanced flame shows that when a discharged is applied an increase in argon is observed, in an argon balanced flame, argon is shown to decrease. The only other noticeable difference is in the nitrogen and nitric oxide changes. Far higher increases in nitrogen and nitric oxide are observed in an argon balanced flame.

5.4 Discussion

From the results obtained in this section it can be seen the only species that decrease are CO_2, H_2O and C_3H_6O when an electric field was applied. Out of the three it was found that only CO_2 and H_2O decreased in large amounts and were also expected species in the flame. The exact reason for the observed decrease in C_3H_6O is unknown however given its change is typically less than 0.05% of the total gas changed, it will be ignored. On the other hand it was seen that N_2, O_2, NO and Ar were found to increase when an electric field was applied. Of the four, N_2 and O_2 were found to increase in large amounts. These observations can be seen in Table 5-3 regarding different electric fields applied under stoichiometric conditions and Table 5-7 regarding the same electric field in different environments of excess oxygen. In this discussion we will explore the different possibilities that could have caused these changes and choose the most likely. Four scenarios can be given for the decrease in CO_2 and H_2O being observed. They are:

1) The applied field is directly or indirectly pushing away the CO_2 and H_2O formed from the sample inlet.
2) The applied field is causing the CO_2 and H_2O to be formed at a different location.
3) The applied field is facilitating plasma reactions as described in section 5.1 or manipulating the flame reactions as described in section 1.5.2. These reactions would involve converting CO_2 and H_2O into other products thus reducing the CO_2 and H_2O signal.
4) The applied field is hindering the reactants, CH_4 and O_2 from reacting thus decreasing the amount of CO_2 and H_2O signal observed.

Applied field is repelling the CO_2 and H_2O away from the sample inlet

This scenario suggests the changes observed in Table 5-3 and Table 5-7 were due to a transport effect. By moving the CO_2 and H_2O away from the inlet we would observe a decrease in both. As the large amounts of CO_2 and H_2O got pushed away, something would have to take its place and the surround air is the most likely candidate. Table 5-3 and Table 5-7 support this as the species that increase are N_2, O_2, NO and Ar, and three of them are found in air. More evidence that the species that increase is from the surroundings is from the experiment replacing N_2 for Ar as the inert gas. From Table 5-9 it can be seen Ar was observed to decrease while in N_2 experiments Ar was seen to increase. This can be explained as during Ar experiments the surrounding air would be rich in Ar. As the CO_2 and H_2O are blown away from the inlet, the Ar rich air will be replaced by the surrounding normal air thus resulting in the observed decrease. This idea can also be applied to the results obtained using excess O_2. In Table 5-7 it can be seen at O_2 flows of 420 ml min^{-1} that a decrease in O_2 is observed when a voltage is applied. This is in contrast to the value increasing at lower flow rates. At higher flow rates the concentration of O_2 would be higher than the surrounding air and thus when the CO_2 and H_2O gets pushed aside, the O_2 rich air gets replaced by normal air which results in the observed decrease.

Applied field is repelling the CO_2 and H_2O directly

With the knowledge that the species that increase are most likely due to air filling the space, the question remains how CO_2 and H_2O were moved. First we will consider if the applied field directly repelled the CO_2 and H_2O away from the sample inlet. H_2O can be polarized as it has a dipole moment[130] however CO_2 cannot be as it is a straight molecule. Although in a uniform field this would result in the H_2O molecule spinning about its centre of mass, in a non-uniform fields this will cause movement[131]. From Figure 5-11 it can be seen that a Pt point electrode opposite a grounded plane electrode produces a highly non-uniform field. The effect of this is that the H_2O molecules will be deflect towards the point electrode.

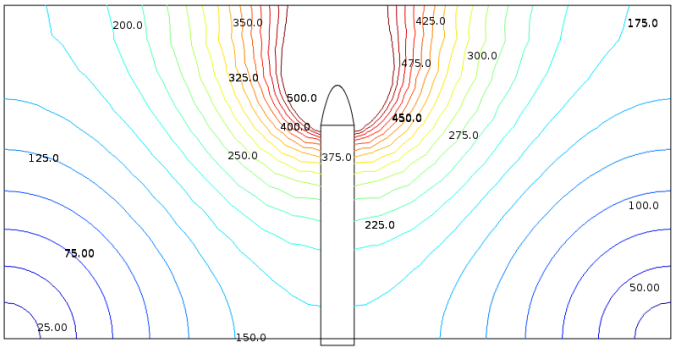

Figure 5-11: Example of the electric field produced from a point shaped electrode polarised positively 100 V opposing a grounded surface.

As the CO_2 molecules cannot interact with the electric field applied, the H_2O that is being displaced would have to move them. From the calibrated multiplier column in Table 5-3 it can be seen that H_2O and CO_2 decreased by the ratio of 1.8±0.3:1 for both when a 2.0 kV and 2.5 kV electric field is applied. This is within error of 2:1, the ratio expected from complete combustion. It is also important to note that a large amount of H_2O still remained when the 2.0 kV and 2.5 kV electric field were applied, 91% and 82% respectively. If H_2O was the primary species to be displaced, it seems unlikely that the amount of H_2O and CO_2 moved away would be in the ratio for complete combustion. It is more likely that much more H_2O would have been pushed away than CO_2. One explanation for the observed ratio of 2:1 is if the H_2O molecules had enough momentum due to the applied electric field to push the CO_2 molecules far enough away from the sample inlet, so they are not drawn in by the vacuum system. It is important to consider the burning velocity of 362 mm s^{-1} [107] for a methane flame as the distance to the sample inlet is only 10 mm.

Applied field is repelling the CO_2 and H_2O indirectly

Another process that could be occurring is the applied field is causing CO_2 and H_2O to move away from the inlet indirectly. From Table 5-1 showing the species present in the bare methane flame we obtain four gases that are in the percentage amounts. These are H_2O, CO_2, N_2, and O_2. Given N_2 and O_2 have no dipole moment they cannot interact with an electric field. This means in order for the electric field to act on them they have

to be ionized. Table 5-10 shows the potentials for ionization and it can be seen O_2 would be the first to ionize.

Species	First Electronic Excitation Potential in eV	Energy of Dissociation in eV	Ionization Potential in eV
O_2	1.635	5.115	12.2
N_2	5.23	9.762	15.58
NO	5.38	6.507	9.25
Ar	11.62		15.76
CO_2	10.0	5.46	13.7
H_2O	7.6	9.511	12.6
CH_4			12.61[132]
CHO			8.14

Table 5-10: Important molecular critical potentials, in electron volts for a methane flame[133]

From the results in Table 5-7 using excess O_2 it was found that there was no effect of changing either the N_2 or O_2 concentration on the decrease in CO_2 and H_2O measured. Using higher amounts of O_2 yield the same amount of decrease in both CO_2 and H_2O. This suggests O_2 is not involved in the processes, although it is also possible the reason no extra change was observed was that amount of O_2 present in the stoichiometric flame as seen in Table 5-1 was enough to saturate the electric field. This meant additional O_2 would not be ionized and therefore no extra decrease in CO_2 and H_2O would be observed. Assuming this was the process occurred, a 2:1 ratio decrease of H_2O to CO_2 would only be observed if the O_2 ion had a large enough momentum to keep CO_2 molecules from being drawn in by the vacuum system.

Applied field is causing CO_2 and H_2O to form away from the sample inlet

The next process that could have led to a decrease in CO_2 and H_2O being observed, is that the applied field caused the combustion reactions to occur away from the inlet. One reason for this happening is the ions produced in the flame are part of the intermediate steps of combustion. In particular for a methane flame the dominant primary ion is CHO^+ as describe in Reaction 4-5. This ion goes on to produce H_3O^+ ion as explained in Reaction 4-6. These ions can be repelled by the applied electric field and therefore the rest of the combustion steps will occur away from their original location. Given the Pt point electrode was positively polarized and directly under the sample inlet, this meant the rest of the combustion could have taken place away from the

sample inlet. This would result in a decrease in observed CO_2 and H_2O. The decrease would be in the ratio 2:1 as the decrease observed is essentially missing combustion. From the calibrated multiplier column in Table 5-3 and Table 5-7 it can be seen the ratio obtained is always 1.8±0.3:1 regardless of voltage applied or amount of excess oxygen.

Applied field is facilitating plasma reactions

The next possibility for explaining the decrease in CO_2 and H_2O is that they are being consumed by a reaction. It is important to point out the following discussion makes the assumption that if a reaction takes place, the products reach the sample inlet unless stated otherwise. Table 5-3 and Table 5-7 do not show any other carbon containing species in the flame apart from CO_2. The only possibility for this is that the products formed have a mass larger than 200 amu or do not reach the detector. It is unlikely that hydrocarbons larger than 200 amu would form and remain stable until the detector. Even if this was the case fragments from these large products would be observed. While it is possible that the CO_2 had been transformed completely in to solid carbon this is also unlikely. This is as the carbon would have been heated from the flame and should give off a yellow emission due to black body radiation. The amount of carbon that would have been produced would make this yellow emission visible to the naked eye. Experiments using a cold finger above the flame were also conducted in an attempt to capture the possible carbon produced. No carbon was found in any of these experiments. Reaction 5-6 also shows any solid carbon formed would react easily with the abundant CO_2

To further support that no plasma reactions involving CO_2 were taking place is that reactions with much lower energies were not observed. One reaction that is likely to have occurred is the reaction of N_2 and O_2 to produce NO as shown in Reaction 5-7[134].

$$\frac{1}{2}\mathrm{N_2}+\frac{1}{2}\mathrm{O_2}\rightarrow\mathrm{NO}\ \ \Delta\mathrm{H}\approx 1.0\ \mathrm{eV\ mol^{-1}}$$

Reaction 5-7

This reaction has been investigated since the 18th century and Birkeland and Eyde commercialised this process for nitrogen fixation. Using an electric arc they converted

N_2 and O_2 into NO which would turn into NO_2 as it cooled with the surrounding O_2. The NO_2 was then dissolved in H_2O to produce HNO_3. Given the environments explored in this chapter, these reactions had the opportunity to occur. Looking at the experiments involving excess O_2 we can see that the flame contained a significant amount of N_2, O_2 and H_2O as seen in Table 5-5. From the table we also see NO with a calibrated amount of 0.50. When a voltage is applied the measured NO is increased, however only by a calibrated amount of ~0.05 as seen in Table 5-7. Table 5-7 also shows NO and N_2 to be the only nitrogen containing species. Given the minimum energy for a CO_2 reaction was 2.9 eV mol^{-1} (Reaction 5-1) compared with 1.0 eV mol^{-1} for a N_2 reaction (Reaction 5-7), it is most likely the observed change in CO_2 was not due to a plasma reaction. This is as little to no N_2 was observed to react.

The production of O_3 also requires much less energy as shown in Reaction 5-8[134] however given the high temperatures of the flame, the O_3 would have likely been converted to nitrogen oxides[135]. The high humidity due to the water vapour would have also decreased the O_3 production due to the formation of OH and HO_2 radicals[136] hindering production. Thus although O_3 is a common product in cold plasmas such as streamers coronas, it would not be expected to be observed.

$$\frac{3}{2}O_2 \rightarrow O_3 \quad \Delta H \approx 1.5 \text{ eV mol}^{-1}$$

Reaction 5-8

A final reaction that could take place is the decomposition of water vapour as seen in Reaction 5-9[122]. From Table 5-1 and Table 5-5 showing the species present in the background methane flame, it is clear H_2O is in abundance. While in Table 5-3 and Table 5-7 no H_2 was observed. It should be noted masses 1 and 2 were not taken however this was because they were never observed to change when using a methane flame and applying an electric field.

$$H_2O \rightarrow H_2 + \frac{1}{2}O_2 \quad \Delta H = 2.6 \text{ eV mol}^{-1}$$

Reaction 5-9

Applied field is hindering combustion

The last possibility for explaining the decrease in CO_2 and H_2O is that the applied field is either preventing some combustion from taking place or from going to completion. This would be able to explain why a drop in CO_2 and H_2O is observed. There are two problems with this theory. The first is that if the field was preventing combustion from taking place a large CH_4 signal should be observed due to the uncombusted fuel and this is not seen in any of the mass spectrums. The field also cannot be preventing the combustion reactions from going to completion as no other carbon containing species were observed aside from CO_2 as shown in both Table 5-3 and Table 5-7.

Most likely process

So far three posibilities have been discussed that could result in the decrease of CO_2 and H_2O. They are:

1) Due to the dipole moment in H_2O, an applied electric field polarizes the molecule thus pushing it away. The H_2O molecules also push the surrounding CO_2 molecules causing the decrease in signal observed.
2) At a high enough electric field O_2 has become ionized and is repelled by the positive electric field. This movement of O_2 ions pushes away the CO_2 and H_2O which causes the decrease in signal.
3) The electric field is repelling ions produced in the methane flame, notably CHO^+ and H_3O^+ causing the final steps of combustion to occur away from the inlet. This would cause an expected decrease of CO_2 and H_2O to happen in the ratio of 2:1 which is observed.

All three mentioned above are transport effects that have caused the decrease in observed CO_2 and H_2O. Figure 5-12 shows video stills of when the electric field was applied and in them seem to show a transport effect has taken place. This is indicated by a dark space appearing where part of the luminous flame once was. Figure A-6 shows the process of this movement taking place over the course of 0.5 s.

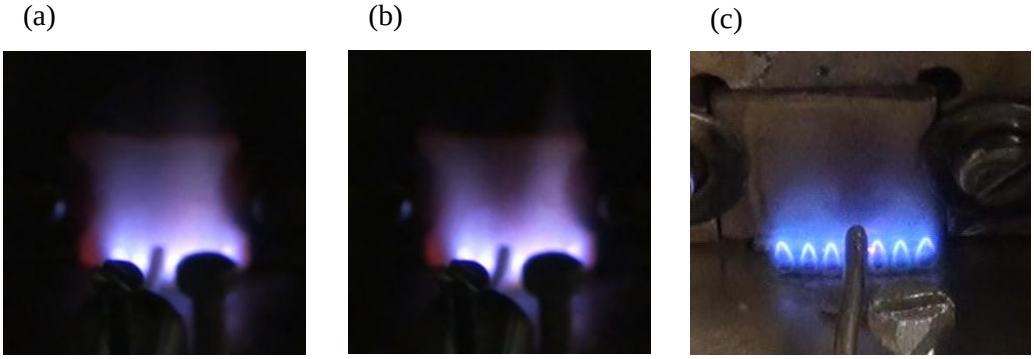

Figure 5-12: Photos showing flame with (a) no electric field taken from Figure A-6(1) (b) with a 2.0 kV electric field taken from Figure A-6(25) (c) also with an applied electric field.

Unfortunately the video stills have some room for interpretation so can't definitively rule any of the three scenarios out however does support that the decrease in CO_2 is transport related.

Results obtained in section 3.6 seem to support the process that the electric field is ionizing O_2 which is then repelled by the point electrode, pushing CO_2 and H_2O away in the process. In that section the same point to plane electrode configuration was used as in this chapter, however slightly different positions and a different point shaped electrode was used. Figure 3-10 shows the ratio change of CO_2 against voltage applied in steps of 0.1 kV when the potential set ranged from 0 – 5 kV and actually applied from 0 – 1.3 kV. It can be seen for that setup after a voltage of 0.9 kV was applied any higher voltages started to cause a decrease in CO_2 observed. This is consistent with the process of O_2 becoming ionized at a particular voltage then once the ion is formed, any higher voltage would push the ion away. As mentioned it is this movement that caused the observed decrease in CO_2.

5.5 Summary

Using mass spectrometry in the Townsend mechanism regime, CO_2 and H_2O were the only species observed to decrease when an electric field was applied to a methane flame. The decrease has been linked to a transport effect moving the species away from the sample inlet. One of the process governing this observation is that at a high enough electric field O_2 gets ionized. Once ionized it is repelled by the highly stressed positive point electrode. This movement of O_2 ions pushes away the CO_2 and H_2O from the sample inlet which causes the decrease in signal. The only species observed to increase were N_2, O_2, Ar and NO have been attributed to the surrounding air replacing the displaced CO_2 and H_2O.

6 Electrical discharge in an oxygen rich hydrogen flame

6.1 Introduction

The previous chapters have used a methane flame as it was the simplest hydrocarbon flame. This chapter will explore the effect of a spark corona discharge on CO_2 and SO_2 in an oxygen rich hydrogen flame. The hydrogen flame is an even simpler combustion reaction and can involve only 8 reacting species. These are H_2, O_2, H, O, OH, HO_2, H_2O_2 and H_2O[137] and corresponds to only 17 elementary reactions[138]. The overall reaction for combustion is shown in Reaction 6-1 and can be reduced to a 2 step mechanism as shown in Reaction 6-2[137].

$$2H_2 + O_2 \rightarrow 2H_2O$$

Reaction 6-1

$$3H_2 + O_2 \rightarrow 2H + 2H_2O$$

$$2H + M \rightarrow H_2 + M$$

Reaction 6-2

The primary ion present in the hydrogen flame is the H_3O^+ ion and is produced as shown in Reaction 6-3[139].

$$2H + OH \rightarrow H_3O^+ + e^-$$

Reaction 6-3

Compared to a methane flame the hydrogen flame is more vigorous. When burnt in air H_2 has a flame temperature of 2400 K and in pure oxygen 3080 K[140]. Its burning velocity is also much higher at 219.7 cm s^{-1} [107] with a flammability limit of 4% and 75% in lean and rich O_2 environments respectively[106].

As chapter 5 has dealt with the possible CO_2 plasma reactions the following will explore possible SO_2 reactions. One of the most common reactions involving SO_2 is its reaction with O_2 to form SO_3 as in Reaction 6-4. This is part of the contact process used for making sulphuric acid. Given the flame used was an oxygen rich flame this reaction is a possible candidate. In the contact process low temperatures are desired as the reaction is exothermic however temperatures of 450 °C are used with a vanadium catalyst.

$$2SO_2 + O_2 \rightarrow 2SO_3 \; \Delta H = \text{-}2.03 \text{ eV}$$

Reaction 6-4

In this chapter the spark corona discharge was created using a Pt point to plane electrode system as in the previous chapters. The Pt point electrode was be moved spatially while obtaining mass spectrometry results.

6.2 Experimental

In this chapter a ceramic burner top was instead of the brass burner top described in section 2.3. Because of this the burner could be water cooled by a Grant (GD120) water bath rather than being gravity fed. To create the spark corona discharge this chapter also used the same Pt point to plane electrode design described in section 3.6. However a set of manual micro positioners (Physik Instrumente M105.20) was used instead of the motorized ones described in section 2.4.2.

The power supply used was also different from the one described in section 2.6 as it was built in house. It was analogue and only the voltage could be controlled. A maximum current of 4.9 mA could be passed and a maximum voltage of 5 kV could be set. The power supply had a switch that enabled it to change polarity, thus the polarity switcher described in section 2.6.1 was not used.

6.2.1 Electrode design

As in the previous chapters, a new Pt point was used. The method for creating the point electrode is described in section 3.6.2 and microscope images of the point electrodes shown in Figure 6-1.

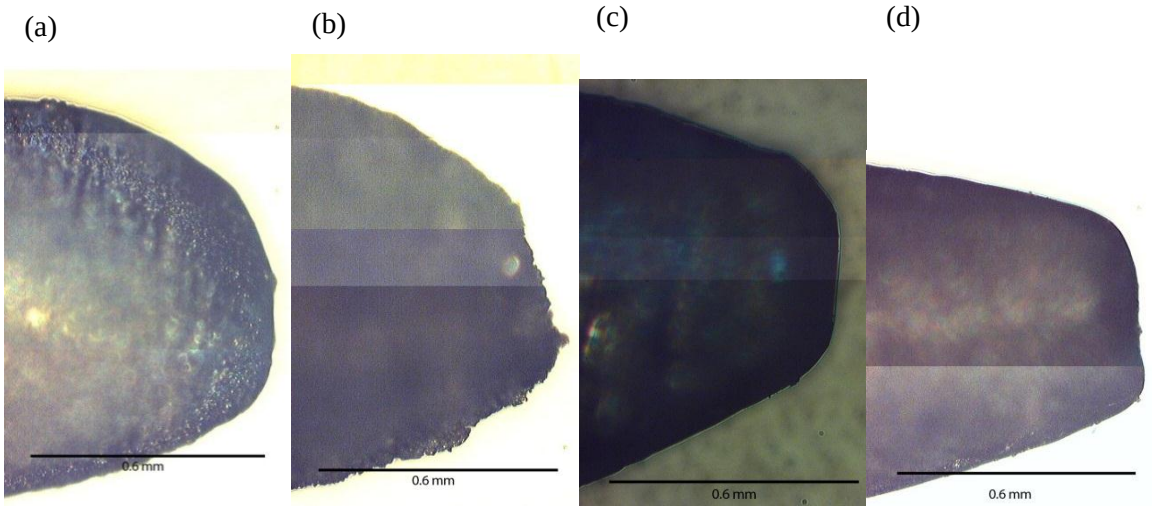

Figure 6-1: Photos of (a) the medium sloped point electrode used in section 3.6 and (b) the electrode used in chapter 4 (c) the electrode used in chapter 5 (d) the electrode used to create the results in this chapter.

From Figure 6-1 (d) it can be seen the electrode created is most visually similar to the electrode used in chapter 5. The point has a flat head and flat sides compared to the more round points used in chapters 3 and 4. As mentioned in previous chapters it is hard to predict what effects the difference in geometry will have.

In this chapter a simple rectangle shaped brass electrode was used for the plane electrode, instead of the electrode described in section 3.6.1 which allowed different materials to be used. The dimensions were 30 mm by 30 mm by 5 mm and held in place using fixing screws as described in section 2.4.2. This arrangement can be seen in Figure 6-3.

6.2.2 Burner setup

The schematic for the ceramic burner top used is shown in Figure 6-2.

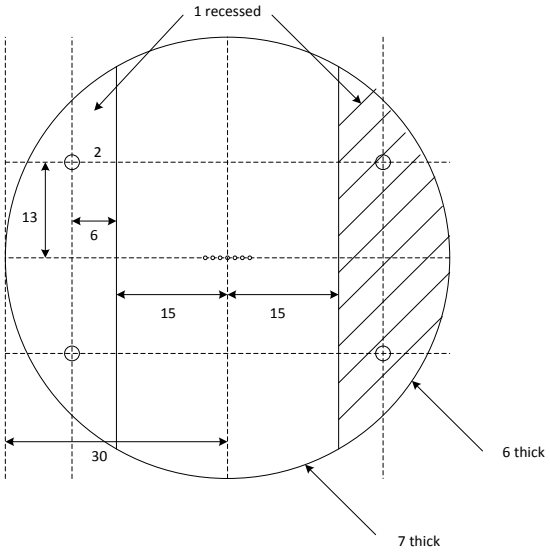

Figure 6-2: Schematic for the ceramic burner top used in this chapter. Dimensions shown are in mm

Seven 0.5 mm holes arranged in a line spaced 0.5 mm apart were drilled in the centre to allow the combustion gases to exit. 6 fixing screws were used along with a copper seal to join the ceramic burner top to the stainless steel support. The ceramic top also had 4 holes which enabled the brass blocks holding the plane electrode described in section 2.4.2, to be screwed directly into the ceramic top. Figure 6-3 shows the experimental setup using the ceramic top.

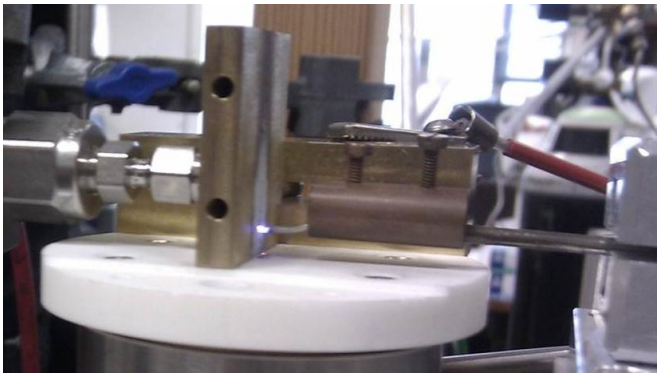

Figure 6-3: Photo showing assembly of the ceramic burner top, Pt point electrode, brass plane electrode and mass spectrometry placement.

6.2.3 Procedure

This chapter investigated the effect of moving the Pt point electrode on the spark corona discharge formed, and the discharge's effect on SO_2 and CO_2. At the start of the experiment the Pt point electrode was placed at a distance 0.3 mm from the brass plane electrode and a height of 1.0 mm from the ceramic top. It was moved out to a distance of 1.2 mm at 0.1 mm increments then up by 0.5 mm. It was then moved from its distance of 1.2 mm back to 0.3 mm again in 0.1 mm increments. This procedure was carried out till a height of 4.0 mm was reached for a total of 70 positions. Figure 6-4 illustrates the beginning of this pattern. At each position 20 mass spectrums were taken. 10 spectrums for the background flame then 10 when a spark was formed. To create the spark discharge the voltage was rapidly increased by hand until a spark was heard to form. The voltage at which the spark stabilized was then recorded.

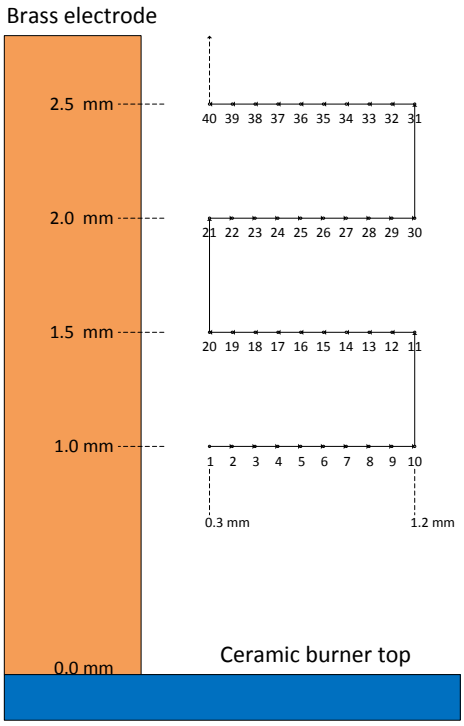

Figure 6-4: First 40 positions of the Pt point electrode during experiments. Not to scale

6.2.4 Mass spectrometer

From the procedure in section 6.2.3, 70 positions were used and 20 mass spectrums taken per position. This gave a total of 1400 mass spectrums per experiment. To collect this data only the SEM detector was used as using faraday became either too time consuming or experimentally complex. The drawback for this was masses 17, 18, 28 and 32 were not taken. These would most likely correspond to the primary peaks of N_2, O_2, and the primary and secondary peaks for H_2O. As all the data was taken on the SEM, their absolute partial pressures are unknown given the detector was tuned to make sure masses near $1x10^{-6}$ Torr would be safely in the 10^{-7} Torr range.

6.3 CO_2 results and discussion

The following results used an oxygen rich hydrogen flame with trace amounts of CO_2. Using the procedure in section 6.2.3 a spark corona discharge was created at various positions. The effect of the discharge and position of the discharge was observed using mass spectrometry.

6.3.1 Spatial dependence of the spark corona discharge voltage and decrease in CO_2 observed

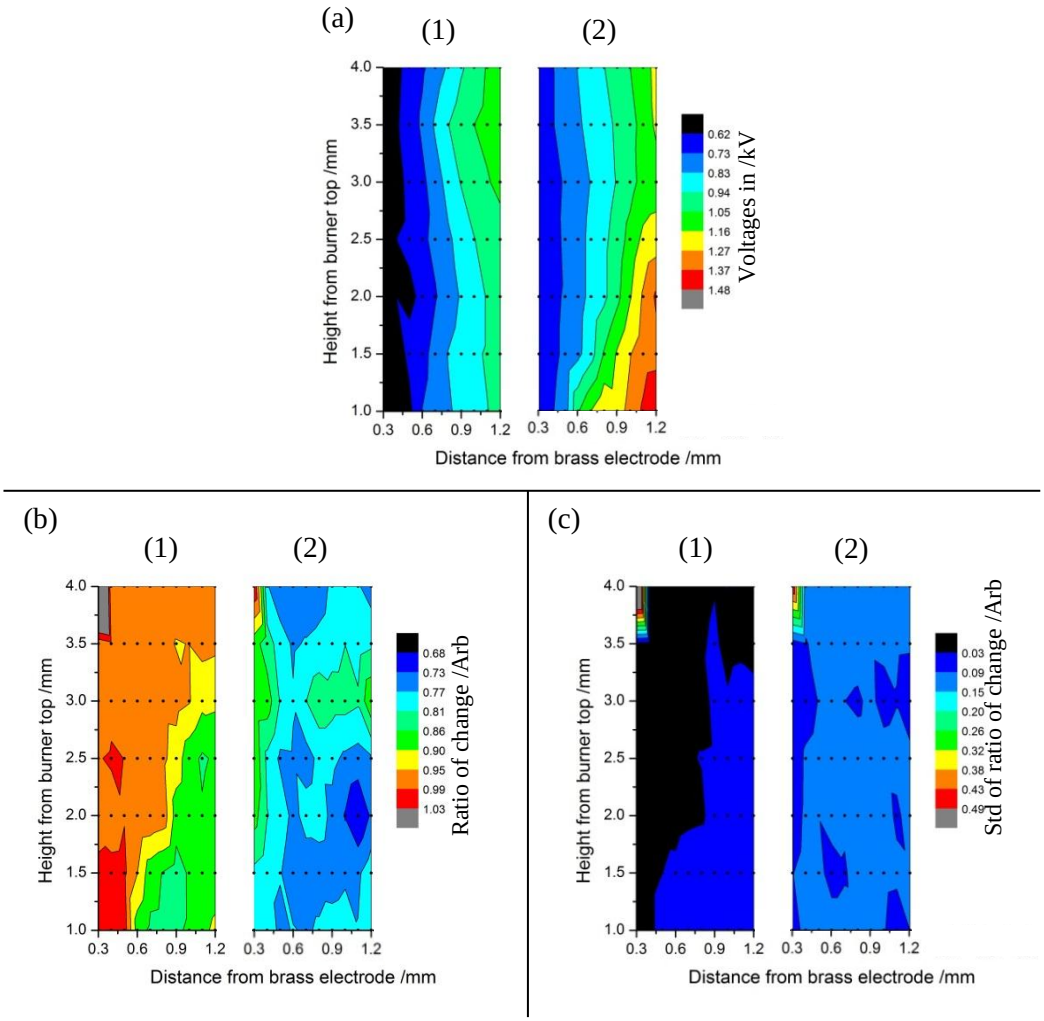

Figure 6-5: Graphs showing spatial plots of (a) voltage used to stabilize a spark corona discharge, (b) ratio of decrease in mass 44 observed taken by averaging 20 points as in section 6.2.4 and (c) 1 standard deviation for (b). Data was obtained when a (1) positive voltage was applied and when a (2) negative voltage was applied. The setup was described in section 2 however the ceramic burner top as mentioned in section 6.2.2 was used. Results were obtained using a hydrogen flame created with the flow rates of 300/300/400/200 ml min^{-1} for $H_2/O_2/N_2/5\%$ CO_2 in N_2. The spark corona discharge was created using a Pt point electrode described in section 6.2.1, moved as described in section 6.2.3 and setup as in section 3.6.

From Figure 6-5 (a) it can be seen the negative spark corona discharges forms at lower voltages than the positive discharge at the same distance. The negative seems to show a uniform relationship between voltages against distance, where the highest voltages are found furthest away. The positive on the other hand seem to outline the flame structure and the highest voltage observed being at the bottom right corner. In Figure 6-5 (b) the negative discharge shows smaller ratio decreases in mass 44 than the positive discharge for the same positions. The highest decrease was observed in a

triangle area near the burner top and furthest away from the brass electrode. The positive discharge on the other hand seems to show an optimal spot for change at 1.1 mm from the brass electrode and 2.0 mm from the burner top. Using Figure 6-5 (c) to account for the error this spot does disappear however only by assuming the averages for the whole section around the spot is at the maximum error. For both the positive and negative discharge, decrease in the change in mass 44 does not follow the same trend as the voltage needed to stabilize the discharge.

6.3.2 Mass spectrometry data

In order to understand the processes that could cause the signal in CO_2 to decrease as observed in section 6.3.1, one position was chosen and its full mass spectrum analysed. This position was when the Pt electrode was placed 1.1 mm away from the brass electrode and 2.0 mm from the burner top. At this position a voltage of 1.28 kV was needed to stabilize the spark corona discharge, and CO_2 decreased by 34±1%. First the background hydrogen flame mass spectrum with the leaked in 5% CO_2 will be shown followed by the changes due to the spark discharge.

6.3.2.1 Background flame mass spectrum

Linear combination along with the fragmentation patterns from Table A-1 will be used to deduce the species and their concentration in the background flame. Figure 6-6 shows the experimental values obtained and the result of the linear combination. Like previous background mass spectrums, the signal from the vacuum chamber has not been removed as the systematic error for doing so could not be accounted for.

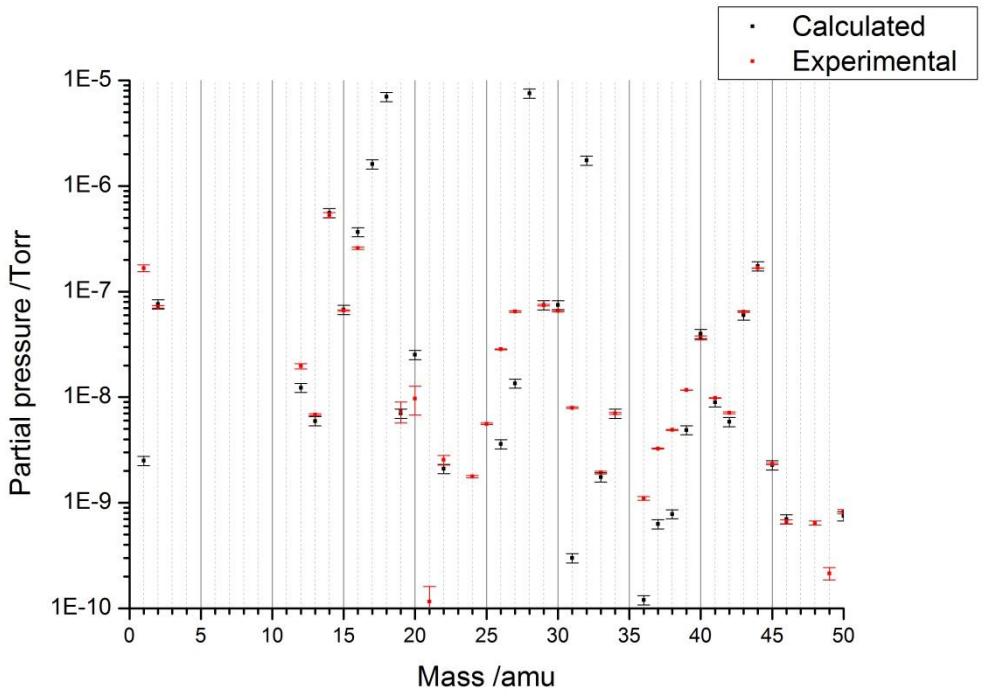

Figure 6-6: Graph showing a mass spectrum of masses 1 – 16, 19 – 27, 29 – 31, 33 - 50 amu above the threshold of detection for a bare hydrogen flame with leaked in CO_2. A Pt point electrode was placed 1.1 mm away from a brass plate electrode and 2.0 mm above the burner top, however no potential was applied. Each point is obtained by taking the average of 10 points. A hydrogen flame using the flow rates of 300/300/400/200 ml min^{-1} for $H_2/O_2/N_2/5\%$ CO_2 in N_2 was used and as described in section 2. Graph showing theoretical mass spectrum created using the fragmentation patterns in Table A-1 and the relative amounts from Table 6-1.

Unfortunately as mentioned masses 17, 18, 28 and 32 were not taken and the effect of this is the amount H_2O, N_2 and O_2 could not be reliably determined. From Figure 6-6 it can be seen the fit of calculated to experimental values was decent but many masses deviated outside error. These were masses 1, 20, 24 - 27, 31, 36 – 39, 48 and 49. The same reasoning for many of these masses can be used from section 5.3.1.1 regarding the background methane flame. Masses 36 – 39 were speculated to be due to acetone not modelled accurately. The difference between calculated and experimental values for masses 27 and 31 was attributed due to their parent peak being extremely large and only 1 amu apart. The high signal of mass 1 was explained by the high transmission peak. From Table A-1 masses 24 – 26 are from the fragmentation of butane and acetone. Both species were found in the empty vacuum chamber in section 2.5.3 however the reason for the fit being better in that section is currently unknown. In previous sections such as 5.3.1.3 mass 20 has shown to give a higher experimental response and the reason for this remains unknown. This leaves masses 48 and 49 which

remain unknown but has been seen in small amounts in the background vacuum chamber in Figure 2-8.

Species	Multiplier x10^{-9} ±10%	Calibrated multiplier ±10%	Percentage of total gas measured ±10%
H_2O	70	77.778	44
CO_2	1.75	1.250	0.71
N_2	75	75.000	42
O_2	17.5	20.349	11
NO	0.75	0.625	0.35
Ar	0.4	0.333	0.19
CH_4	0.75	0.469	0.27
H_2	0.25	0.568	0.32
C_3H_6O	0.6	0.083	0.047
C_4H_{10}	0.3	0.061	0.035
DP oil ppe	0.0075	0.008	0.0042

Table 6-1: Relative amount of species used to produce Figure 6-6 and the calibrated amounts using Table A-2.

As mentioned the values for H_2O, N_2 and O_2 are likely not accurate in Table 6-1 however it can clearly be seen CO_2 is observed. More importantly the table shows the hydrogen flame burnt cleanly and no unexpected products.

6.3.2.2 Mass spectrometry results due to an applied electric field

To understand the effect of the spark corona discharge, the changes of each mass when the discharge is on will be examined. This will allow the signal from the vacuum chamber and background flame to be removed. Once these species are found linear combination with their respective fragmentation patterns will be used to compare the experimental values obtained with calculated ones.

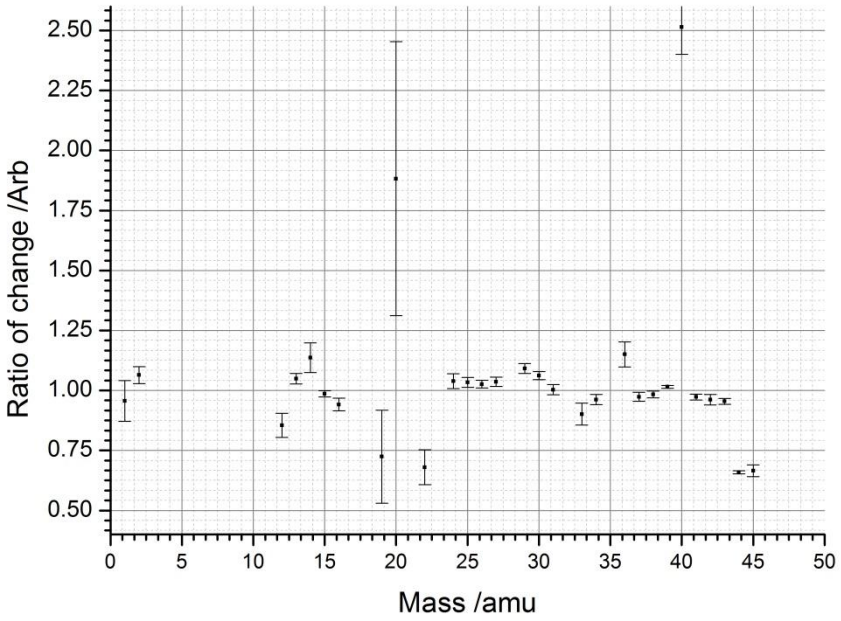

Figure 6-7: Mass spectrum of change taken from Figure 6-5 when Pt point electrode was at a position 1.1 mm from the brass electrode at 2.0 mm from the burner top. A spark corona discharge was formed when 1.28 kV was applied between the Pt point electrode and brass plane electrode.

From Figure 6-7 it can be seen some masses change a lot due to the discharge however some masses are very close to a ratio of 1, but show a statistically significant change, for example masses 24 - 27. The reason for this can be explained in Figure 6-8.

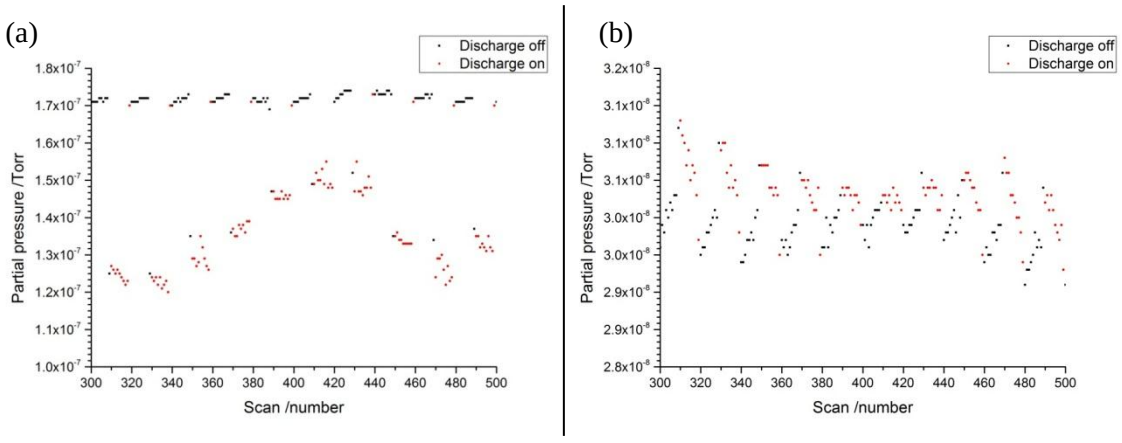

Figure 6-8: Graph showing raw data obtained for (a) mass 44 and (b) mass 26 from Figure 6-5.

In Figure 6-8 we see the response of (a) mass 44 and (b) mass 26 against time. Each cluster from mass 44 shows a distinct response for a different Pt point position from section 6.2.3. Mass 26 on the other hand appears to show all the clusters as oscillating

around a single partial pressure. Responses that behaved in a similar manner to mass 44 were considered as real, while those that responded like mass 26 were attributed to experimental errors. By looking at these ratios and the raw data of how each mass changes over time, only the masses that show real changes were considered. With these masses and using their ratio change, they can be grouped and identified using Table A-1. Table 6-2 shows the result of this process.

Voltage measured in kV	1.28±0.02	
Current measured in mA	4.9±0.04	
Mass in amu	**Ratio from baseline**	**Species**
22	0.68±0.07	CO_2
44	0.66±0.01	
45	0.67±0.02	
46	0.68±0.06	
20	1.88±0.57	Ar
36	1.15±0.05	
40	2.51±0.11	
13	1.05±0.02	N_2
14	1.14±0.06	
29	1.09±0.02	
16	0.94±0.03	O_2
33	0.90±0.03	
34	0.96±0.02	
19	0.72±0.19	H_2O
30	1.06±0.02	NO
12	0.85±0.05	CO_2*
41	0.97±0.01	C_3H_6O
42	0.96±0.02	
43	0.95±0.01	

Table 6-2: Identification of masses from Figure 6-7 to correlate masses in amu to species. Red indicates a decrease of the species, green indicates an increase of the species while orange indicates the parent mass. Experimental conditions as in Figure 6-7. Assignment of starred masses are explained in the text.

From Table 6-2 it can be seen there are only 7 species. These were CO_2, Ar, N_2, O_2, H_2O, NO and C_3H_6O. Like in chapter 5, CO is an important species that needs to be accounted for. Unfortunately mass 28 was not taken and there is no way of knowing if CO was present. Although N_2 could be approximated by masses 14 and 29, the true 28 peak will remain unknown. Worryingly unlike in chapter 5 where mass 12 changed by the same ratio as the other CO_2 peaks, this is not the case here suggesting there could be another small carbon containing species. As CO_2 is the only carbon containing species firmly identified, mass 12 has been assigned to it; however this could be in error. Using the 7 species found and multipliers described in Table 6-3, linear combination along with the

fragmentation pattern from Table A-1 was used to calculate the mass spectrums in Figure 6-9.

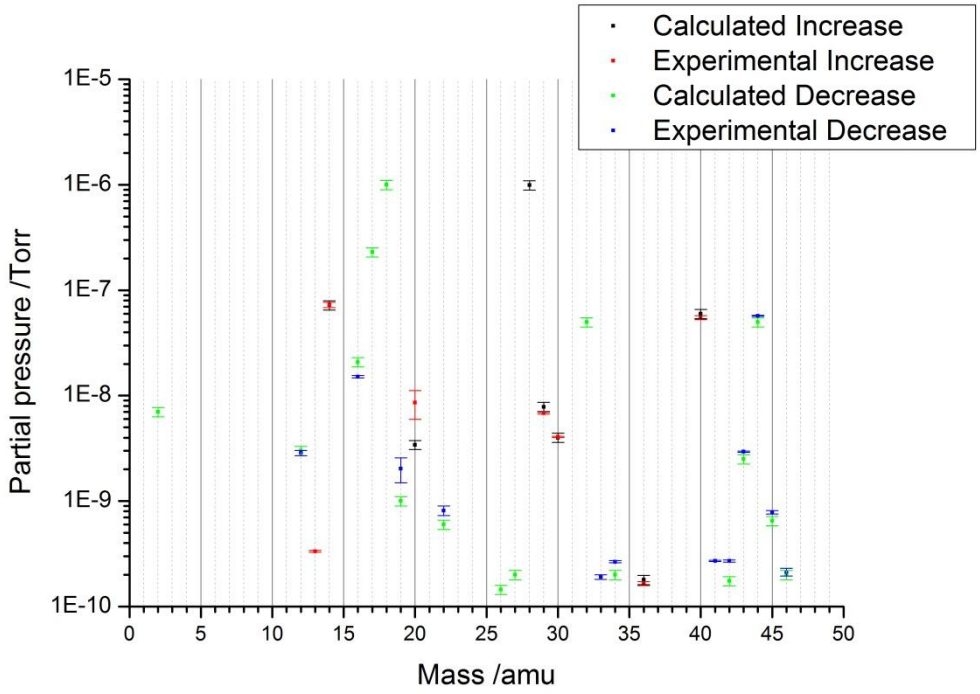

Figure 6-9: Graph showing mass spectrums of the absolute changes observed for the increase and decrease of masses 1 – 50 amu when a spark corona discharge was formed at a voltage of 1.28 kV. Calculated values were obtained using the fragmentation patterns in Table A-1 and the relative amounts from Table 6-3. Experimental conditions are from Figure 6-7.

From Figure 6-9 where there are experimental values, the fit between them and the calculated values appears very good. Unfortunately without the peaks of 28, 32 for N_2 and O_2 respectively and in particular both 17 and 18 for H_2O, it is hard to tell how accurate the predictions really are. In particular, mass 2 a fragment of H_2O was calculated to decrease by a significant amount however was not seen experimentally. It is important to note that mass 19 was the only fragment of H_2O and in previous results its experimental value when compare to calculated, was up to a magnitude too high. The effect is that the change in H_2O will be vastly over estimated however the direction of change can likely be used. The most important mass that is accurately modelled is mass 12. This shows that although Table 6-2 shows it changed by a different ratio than its parent peak, the signal is very likely all due to CO_2.

Species	Multiplier x10^{-9} ±10%	Calibrated multiplier ±10%	Percentage of total gas measured ±10%
H_2O	-10	-11.1111	48
CO_2	-0.5	-0.3571	1.5
N_2	10	10.0000	43
O_2	-0.5	-0.8721	3.8
NO	0.03	0.0250	0.11
Ar	0.6	0.5000	2.2
C_3H_6O	-0.025	-0.0069	0.030

Table 6-3: Relative amount of species used to produce Figure 6-9 and the calibrated amounts using Table A-2. Green represents an increase in concentration due to the discharge while red a decrease.

From Table 6-3 and Figure 6-9 it can be seen that the spark corona discharge decreased the amount of observed CO_2, H_2O, O_2 and C_3H_6O however no other carbon containing species were identified. N_2, NO and Ar on the other hand were observed to increase. Unfortunately as mentioned previously the values obtained for H_2O, N_2 and O_2 are most likely inaccurate with H_2O being the most inaccurate due to missing both its primary and secondary peaks.

6.3.3 Discussion

From Table 6-3 it can be seen there was a decrease in CO_2, H_2O and C_3H_6O, while N_2, NO and Ar increased. These changes are very similar to those obtained in chapter 5 with the main difference being O_2 which decreased in these results. Chapter 5 attributed these changes due to transport effects pushing away the CO_2 and H_2O. As in chapter 5 the reasons for the decrease in C_3H_6O remains unknown but is typically less than 0.05% of the total gas changed. It is also not an expected species produced by a hydrogen flame or CO_2 and will be ignored. The species that show an increase are all found in air. This makes it likely that the surrounding air replaced the displaced CO_2 and H_2O. The reason for the decrease in O_2 in this chapter compared to the increase in chapter 5 is likely to do with the large amount of O_2 in the background flame as seen in Table 6-1. Given that no other carbon containing species were observed transport effects are the most likely cause of these results.

Assuming the transport effects are a function of the applied electric field it would be expected that the spatial results for the decrease in CO_2 from Figure 6-5 (b) would match closely with the voltage needed to sustain the spark in Figure 6-5 (a). This is not the case and currently the reason why remains unknown.

6.4 SO_2 results and discussion

The next set of results was obtained using an oxygen rich hydrogen flame but with trace amounts of SO_2. Again a spark corona discharge was created at various positions, and mass spectrometry was used to measure the effect of the discharge and changing its position.

6.4.1 Spatial dependence of the spark corona discharge voltage and decrease in SO_2 observed

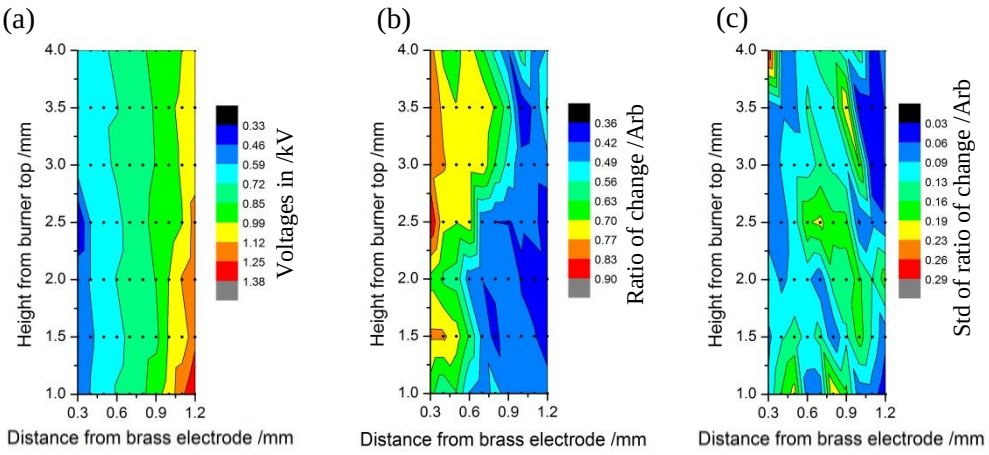

Figure 6-10: Graphs showing spatial plots of (a) voltage used to stabilize a positive spark corona discharge, (b) ratio of decrease in mass 64 observed and (c) standard deviation for (b). The setup was described in section 2 however the ceramic burner top as mentioned in section 6.2.2 was used. Results were obtained using a hydrogen flame created with the flow rates of 300/300/400/200 ml min^{-1} for $H_2/O_2/N_2$/5% SO_2 in N_2. The spark corona discharge was created using a Pt point electrode described in section 6.2.1, moved as described in section 6.2.3 and setup as in section 3.6.

From Figure 6-10 (a) the voltage required to create sustain the positive spark corona discharges shows a uniform relationship against distance. The further away the Pt point electrode was placed, the higher the voltage was needed. Height appeared to not have an effect on the voltage needed. This is in contrast to what was observed for when CO_2 was used shown in Figure 6-5 (a)(1). The voltages required are also much lower and is expected as the breakdown potential relative to air for SO_2 is 0.3 compared to 0.95 for CO_2[141]. Comparing Figure 6-10 (a) and (b) it seems there is no relationship between the ratio of decrease of mass 64 and the voltage required to create the discharge. From (b) it appears the highest decrease was found in a localised area. This was when the Pt point was placed at 1.1 mm away from the brass electrode and at a height 2.0 mm

from the burner top. When accounting for the error using Figure 6-10 (c) the spot could be turned into an area.

6.4.2 Mass spectrometry data

Similar to section 6.3.2 regarding CO_2, the mass spectrums from the position of maximum change for SO_2 will be explored. This was also when the Pt electrode was at a distance of 1.1 mm from the brass electrode and 2.0 mm from the burner top. At this position the discharge required 1.13 kV to be applied and, SO_2 was observed to decrease by 63±11%. First the mass spectrum of the flame with SO_2 will be shown followed by the mass spectrums of the changes due to the spark discharge.

6.4.2.1 Background flame mass spectrum

Like other mass spectrums, the background flame will be analysed using linear combination along with the fragmentation patterns. Figure 6-11 shows the experimental values obtained and the results from linear combination. Like previous background mass spectrums, the signal from the vacuum chamber has not been removed.

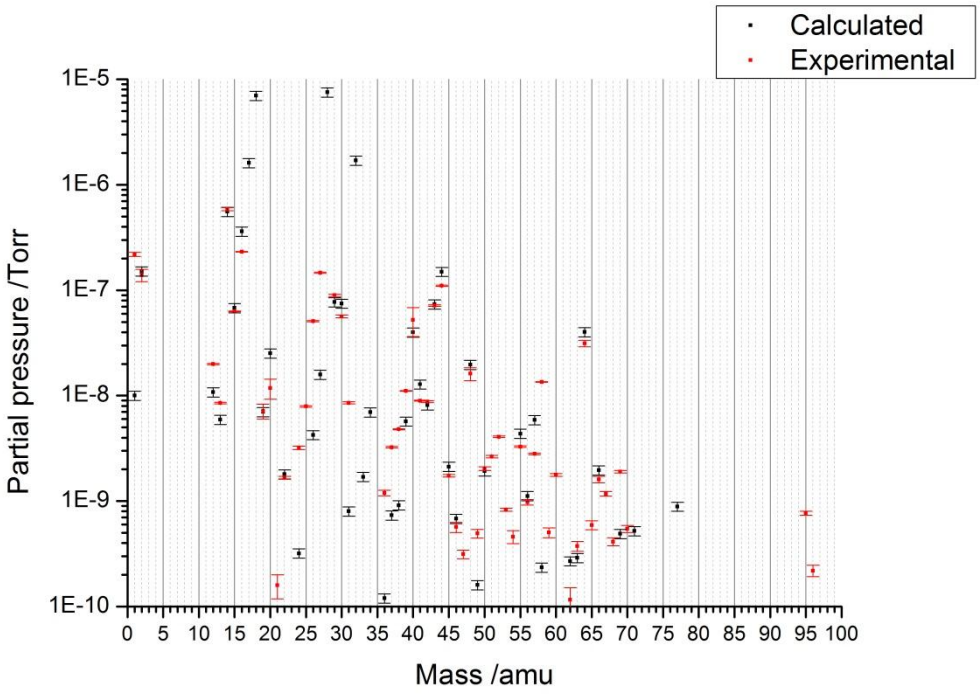

Figure 6-11: Graph showing a mass spectrum of masses 1, 2 , 12 – 16, 19 - 27, 29 - 31, 35 - 70, 95, 96 amu above the threshold of detection for a bare hydrogen flame with leaked in SO_2. A Pt point electrode was placed 1.1 mm away from a brass plate electrode and 2.0 mm above the burner top, however no potential was applied. Each point is obtained by taking the average of 10 points. A hydrogen flame using the flow rates of 300/300/400/200 ml min^{-1} for $H_2/O_2/N_2/5\%$ SO_2 in N_2 was used and as described in section 2. Graph showing theoretical mass spectrum created using the fragmentation patterns in Table A-1 and the relative amounts from Table 6-4.

As in the section 6.3 regarding CO_2 instead of SO_2, masses 17, 18, 28 and 32 were not taken. This meant the amount H_2O, N_2 and O_2 could not be reliably determined. The fit between the experimental values and calculated in Figure 6-11 was reasonable. Masses that deviated largely outside of error bars were 1, 20, 24 – 27, 31, 36 – 39, 48 and 49 and several above 50. Section 6.3.2.1 regarding the background hydrogen flame with CO_2 contains the explanation for masses 1, 20, 24 - 27, 31, 36 – 39, 48 and 49. This leaves masses above 50, which from section 2.5.3 regarding the vacuum background have been attributed to large hydrocarbons like oils. For this section the most

important peak is mass 64, which could be due to SO_2 or SO_2 containing species like H_2SO_4. The good fit of mass 64 and 66 suggests all the mass 64 observed was due to SO_2.

Species	Multiplier x10^{-9} ±10%	Calibrated multiplier ±10%	Percentage of total gas measured ±10%
SO_2	0.4	0.1905	0.11
H_2O	70	77.7778	46
CO_2	1.5	1.0714	0.64
N_2	75	75.0000	45
O_2	8	9.3023	5.5
NO	0.75	0.6250	0.37
Ar	0.4	0.3333	0.30
CH_4	0.75	0.4688	0.28
C_3H_6O	0.35	0.0972	0.058
H_2	1	2.2727	1.4
C_4H_{10}	0.35	0.0714	0.043
C_2H_2	0.5	0.5000	0.30
C_2H_5OH	0.005	0.0014	0.00083
DP oil ppe	0.01	0.0100	0.0060
Rotary oil	0.05	0.0500	0.030
Turbo oil	0.01	0.0100	0.0060

Table 6-4: Relative amount of species used to produce Figure 6-6 and the calibrated amounts using Table A-2.

It is likely the values for H_2O, N_2 and O_2 are not accurate in Table 6-4 due to their missing parent peak. Table 6-4 and Figure 6-6 shows that at least some SO_2 has reached the sample inlet.

6.4.2.2 Mass spectrometry results due to an applied electric field

Like the previous section regarding CO_2, the effect of the spark corona discharge will be explored by looking at the changes of each mass when the discharge is on. This will allow the signals from the vacuum chamber and background flame to be removed. Once these species are found linear combination with their respective fragmentation patterns will be used to compare the experimental values obtained with calculated ones.

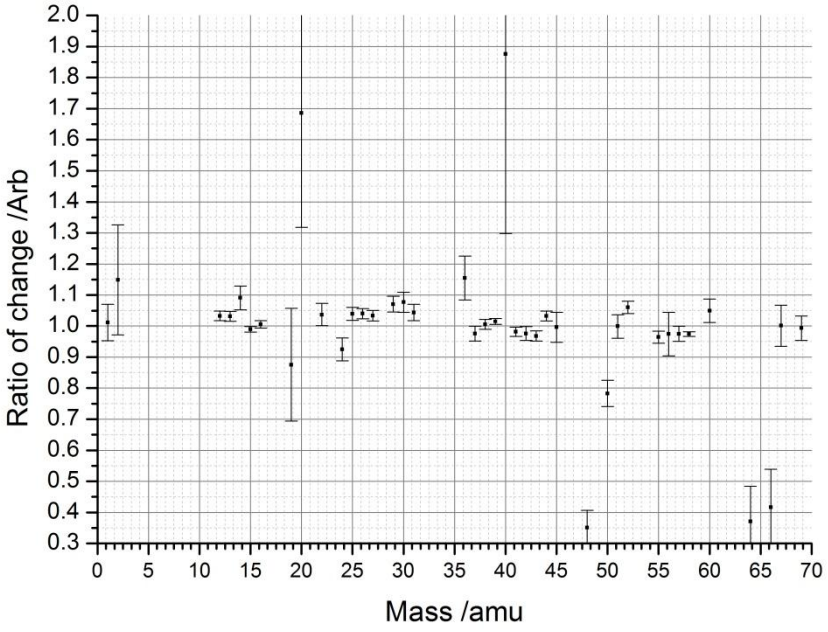

Figure 6-12: Mass spectrum of change taken from Figure 6-11 when Pt point electrode was at a position 1.1 mm from the brass electrode at 2.0 mm from the burner top. A spark corona discharge was formed when 1.13 kV was applied between the Pt point electrode and brass plane electrode.

In Figure 6-12 some masses show a large response when the discharge is applied while others show a very small but statistically significant change. As explained in Figure 6-8 showing the response of two masses against time, it can be seen that some masses show a change but could be due to experimental error. Table 6-5 was produced by looking at the masses raw response against time to insure they are real and grouping masses with the same ratio change together.

Voltage measured in kV	1.13±0.02	
Current measured in mA	4.9±0.04	
Mass in amu	**Ratio from baseline**	**Species**
48	0.35±0.06	SO_2
64	0.37±0.11	
66	0.42±0.12	
20	1.69±0.37	Ar
36	1.16±0.07	
40	1.88±0.58	
14	1.09±0.04	N_2
29	1.07±0.03	
12	1.03±0.02	CO_2
13	1.03±0.02	
22	1.04±0.02	
44	1.03±0.02	
41	0.98±0.01	C_3H_6O
42	0.98±0.02	
43	0.97±0.02	
58	0.97±0.01	
1	1.01±0.06	H_2
2	1.15±0.18	
30	1.08±0.03	NO
16	1.01±0.01	O_2*
31	1.04±0.03	O_2*
19	0.88±0.18	H_2O
50	0.78±0.04	SO_2*
24	0.92±0.04	SO_2*
15	0.99±0.01	C_3H_6O*
52	1.06±0.02	?

Table 6-5: Identification of masses from Figure 6-12 to correlate masses in amu to species. Red indicates a decrease of the species, green indicates an increase of the species while orange indicates the parent mass. Experimental conditions as in Figure 6-12. Assignment of starred and question marked masses are explained in the text.

8 different species have been identified in Table 6-5. They are CO_2, Ar, N_2, O_2, H_2O, NO, C_3H_6O and SO_2. However 1 mass showed a real change that could not be identified. This was mass 52 and shown to increase by small amounts. Although mass 24 is not a fragmentation of SO_2, it has been assign to it as doubly charged SO is. This can be explained as in this thesis the only species encountered that contains mass 24 as a fragment are NO and C_2H_2. From the table it can be seen NO is shown to increase and thus an unlikely candidate. C_2H_2 has been seen in the vacuum chamber however its primary peak of 26 does not decrease. Mass 15 has been assigned to C_3H_6O as although it is not a fragment in the Hiden library, it is in the Nist library as seen in Table A-1. Mass 50 has been identified as a fragment of SO_2 as although it did not change in the

same amount as its other fragments, the only other species it could be was C_4H_{10} or DP oil ppe. It is important to note that mass 19 was the only mass used to identify H_2O. The experimental values for this mass have been typically found to be nearly a magnitude higher. The effect of this is that the change calculated for H_2O is likely to be far higher than the real value. Although the real value can't be used the direction of the change should be reliable. Similarly mass 16 is the only mass used to identify O_2 in this table. While it is typically modelled more accurately than mass 19, it is the fragment of many other species including H_2O. The effect of this is the value calculated is likely to be inaccurate. Although the amount of O_2 can't be reliably calculated the direction of change can be deduced using masses 16 and 31. Mass 31 is not an expected fragment of O_2 however it has always been under estimated. The reason for this is its potential parent peak is 1 amu away and very large. Given both mass 16 and 31 increases it is likely O_2 does. With these limitations in mind and using the 8 species found, multipliers described in Table 6-6 and the fragmentation pattern from Table A-1, Figure 6-13 was produced.

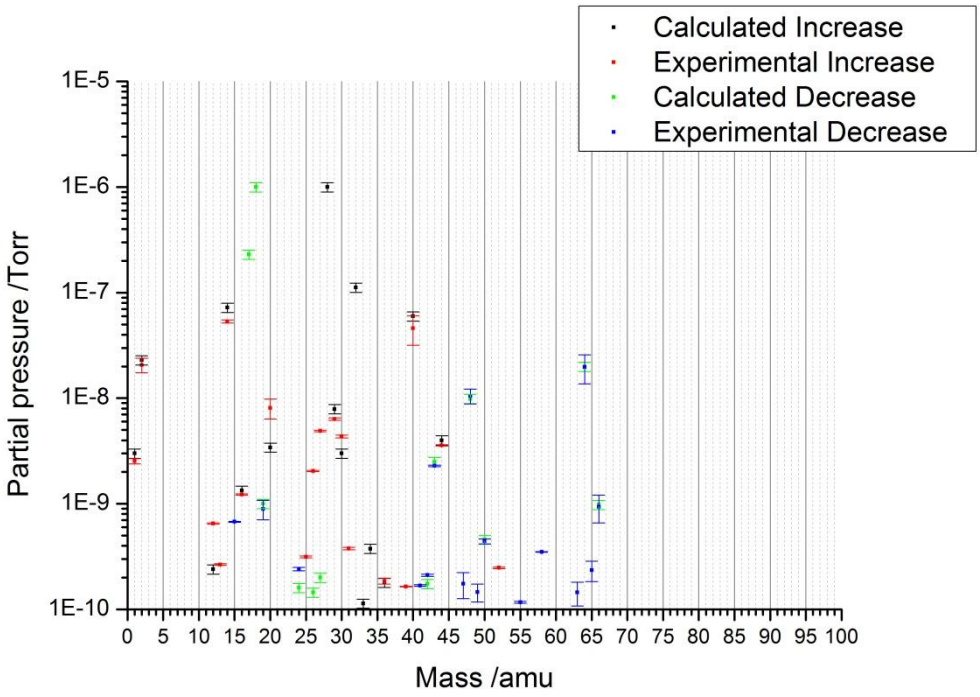

Figure 6-13: Graph showing mass spectrums of the absolute changes observed for the increase and decrease of masses 1, 2 , 12 – 16, 19 - 27, 29 - 31, 35 - 70, 95, 96 amu when a spark corona discharge was formed at a voltage of 1.13 kV. Calculated values were obtained using the fragmentation patterns in Table A-1 and the relative amounts from Table 6-6. Experimental conditions are from Figure 6-12.

For the experimental values above the detection limit of $1x10^{-9}$ Torr in Figure 6-13, the calculated values match reasonably well. Masses 12, 15, 20, 25 – 27, 31, 52 and 58 show a larger experimental change than calculated but it should be noted only masses 26 and 27 are above the set detection limit. The group of mass 25 – 27 are all fragments of C_2H_2 which has been observed in the vacuum chamber. Mass 12 is typically modelled well and relates to carbon. Given CO_2 is the only carbon containing species to increase it is unknown why the fit is not as good as other results. Masses 20 and 31 have both been explained previously in section 6.4.2.1 regarding the background flame mass spectrum. Masses 15 and 58 could be due to acetone not being modelled accurately as they are both fragments and show the same direction of change of the primary peak. Finally this leaves mass 52 which from Table 6-5 is shown to increase and still remains unidentified.

Species	Multiplier $x10^{-9}$ ±10%	Calibrated multiplier ±10%	Percentage of total gas measured ±10%
SO_2	-0.2	-0.0952	0.40
CO_2	0.04	0.0286	0.12
H_2O	-10	-11.1111	47
N_2	10	10.0000	42
O_2	1.14	1.3256	5.6
NO	0.03	0.0250	0.11
Ar	0.6	0.5000	2.1
H_2	0.3	0.6818	2.96
C_3H_6O	-0.03	-0.0083	0.035

Table 6-6: Relative amount of species used to produce Figure 6-13 and the calibrated amounts using Table A-2. Green represents an increase in concentration due to the discharge while red a decrease.

From Table 6-6 and Figure 6-13 it can be seen the amount of SO_2, H_2O and C_3H_6O decreased when a spark corona discharge was applied. Unfortunately as mentioned previously the amount H_2O is likely to be highly inaccurate. On the other hand the amount of CO_2, N_2, O_2, NO, Ar and H_2 was seen to increased. Of these species the actually amount of increase for N_2 and O_2 is also likely to be inaccurate.

6.4.3 Discussion

From Table 6-4 it can be seen some SO_2 was able to reach the sampling inlet. This is important as it can also be seen that there is some O_2 and a lot of H_2O in the flame. Both could react with SO_2 to form either SO_3 or H_2SO_4. SO_3 is a white solid and would

not be picked up by the sample inlet. In Figure 6-3 showing a photo of the experimental setup a white precipitate is clearly visible on the brass electrode. From Table 6-6 it can be seen when SO_2 is leaked in and a spark discharge is applied, SO_2, H_2O and C_3H_6O are seen to decrease. On the other hand CO_2, N_2, O_2, NO, Ar and H_2 were seen to increase. The amount of C_3H_6O is very small and the reason for it decreasing remains unknown, and as in previous discussions it will be ignored.

Previous explanations would suggest the decrease in SO_2 is due to transport effects caused by the electric field. However it is also possible that spark discharges causes the O_2 to react with the SO_2 to form SO_3 as explained in Reaction 6-4. Given that the product would not reach the sample inlet due to being solid, it can't be distinguished whether SO_2 has reacted or been moved away. It should be noted that Reaction 6-4 is exothermic so yield is highest at low temperatures. This is in contrast to the high temperature of 2400 K for the hydrogen flame when burnt in air.

When the spark discharge was applied CO_2 was observed to increase. From Table 6-4 regarding the background flame with SO_2 it can be seen there was trace amounts of CO_2. Assuming the CO_2 has come from the surrounding air, the increase in observed CO_2 can be explained by transport effects occurring.

H_2 was also observed to increase when the discharge was applied. Given that the flame was burnt in excess oxygen no H_2 is expected. The cause for the increase could be due to the discharge decomposing water as described in Reaction 5-9. However this seems unlikely as the same increase in H_2 was not seen in the results regarding CO_2. The observed H_2 seen in Table 6-4 regarding the background flame is likely from the vacuum chamber and why it increase when a discharge is applied remains unknown.

Similar to the results from CO_2, the spatial results from Figure 6-10 (a) and (b) suggests the decrease in SO_2 is independent of stabilization voltage which is not expected. However unlike CO_2, when accounting for the error a relationship between stabilization voltage and decrease in SO_2 can be formed.

6.5 Summary

In this chapter the effect of a spark discharge on SO_2 and CO_2 in a hydrogen flame was explored. Both were observed to decrease when the spark applied. It is possible that similar to chapter 5 transport effects could be used to explain the decrease of both. For CO_2 this is more likely to be the case than SO_2 which could have reacted to form SO_3. A relationship between spatial plots of stabilization voltage required for sustaining the spark discharge and decrease in CO_2 could not be made. For SO_2 accounting for error on the decrease in SO_2, a tentative relationship could be made.

7 Conclusions and suggestions for future work

7.1 Conclusion

This thesis reports the creation of a system that appeared to reduce the amount of CO_2 produced by a methane flame by significant amounts. The system involved used a point to plane electrode configuration placed just above the methane flame. A high electric field was applied between them with the point electrode being polarised positively, and the plane electrode grounded. When this was done the observed CO_2 and H_2O signals was seen to drop by a few 10s of percentage points while N_2 and sometimes O_2 increased by a few 10s of percentage points as well. H_2O and CO_2 was observed to always decrease in the ratio 2:1 while the ratio of increase for N_2 and O_2 varied depending on the experiment.

After careful analysis it was found the appeared reduction in CO_2 and H_2O was due to transport effects causing the molecules to not reach the sampling inlet. One of the possible process that caused this was the high electric field was ionizing O_2 molecules which would then be repelled by the positive point electrode. Given the mean free path at atmosphere this movement pushed both CO_2 and H_2O molecules away. As the point electrode was under the sampling inlet, the effect this had was the detector showed a decreased response for both molecules. The large displacement of CO_2 and H_2O also caused the surrounding air to be drawn in to take their place. This explains the increase in observed N_2 and sometimes O_2. Depending if the surrounding air had more or less O_2 than the flame, would determine if the O_2 signal was seen to increase or decrease.

Using the same electrode configuration and keeping the point electrode positively polarized, varying the voltage enabled a current against voltage trace to be obtained. This successfully produced three distinct corona discharges to be formed in the flame. They were the streamer, glow and spark corona discharges. With the power supply used a spark corona discharge could only be produced when the point electrode was placed significantly near the plane electrode. The formation of all three were capture using video, audio, current and voltage data at the 0.02 s time scale. It was observed that the streamer corona discharge produced the highest decrease in CO_2, however the reason for this was it required the highest applied voltage. As mentioned previously at

these high voltages it was determined that transport effects were the cause of observed CO_2 decrease.

SO_2 and CO_2 were also explored in a hydrogen flame. It was found that both decreased and could be explained in terms of transport effects. For CO_2 a relationship between the stabilization voltages required for the spark discharge and decrease in CO_2 could not be made. This was seen as the point electrode was moved to different positions in the flame that required different stabilization voltages. This relationship is expected if the decrease in CO_2 observed was due to transport effects.

To carry out the investigations above an automated experimental platform was successfully created. Gas flows, electrode positioning and the applied voltage and current could be controlled with no interaction. They could be controlled to change according to time or number of readings. Mass spectrums, actual applied voltages and currents along with video, audio data were all collected and synchronized. This meant large amounts of high quality repeatable data could be collected. It also allowed randomized factorial experiments to be conducted however these procedures were not needed. While this platform was used to investigate discharges in a methane flame, the overall idea can be applied to experimental procedures in general

7.2 Suggestions for future work

In this thesis it was found that the large decreases in CO_2 observed were due to transport effects rather than chemical or plasma reactions. The reactions that this project aimed to explore regarding dissociation of CO_2 into CO or C are physically possible and were even taking place in the mass spectrometer ionization section. Given how important these reactions are to the environment, future attempts are warranted.

The following are several suggestions regarding what changes might need to be made to get the reaction to take place. The first change that should be made is an attempt to contain the flame. Doing so improves the chance that the CO_2 molecule will react as it can't leave the reaction cell. Increasing the number of electrons would also help the chances that the molecule will react. This can be done by doping the flame with additives. One of the reasons why the transport effects took place is due to the high electric fields acting on either the dipole or ions. This caused them to move in one direction until they were no longer in the flame. A solution to this is to use a radio frequency generator instead of a static electric field. This would allow high electric fields but due to the rapid changes, the electrons and ions should remain contained.

The suggestions made so far all are from a plasma chemistry point of view. Another possible method of getting electrons to the CO_2 molecule is by the surface of a metal, which would be an electrochemical approach. In this work the faradaic current was never high enough that an electrochemical approach would give a signal. This was primarily due to the high resistivity of the flame. If a radio frequency generator could be used to contain the ions and electrons as well as generating more ionic species at the same time focusing them into an electrochemical cell, it may be possible to drive CO_2 reactions by electrochemistry.

In this work mass spectrometry was used to understand the processes occurring however had several limitations. The spectrometer used had only 1 amu resolution and the species being examined had many over lapping peaks. The consequence of this is unambiguous identification of the species became difficult. The spectrometer being un-calibrated also meant that all results had at least a ±10% random error. Another drawback that was faced was the sample inlet could not be easily moved which meant spatial data could not be taken.

With these difficulties in mind a more efficient method would be to use spectroscopic methods. In particular cavity ring down systems would solve the problems mentioned above. They would allow spatial data to be obtained and the identification of the signal is unambiguous while also providing concentration data. The flexibility of using optics synergies well with the automated platform created.

While the platform was sufficient in collecting data for this work, more improvements can be made. One could be to enable the platform to dynamically react to the data it was collecting. This feature would actually be simple to add as the program was written with this dynamic feature in mind. The reason it wasn't done was because it was the learning aspect that was not solved. The first step in tackling the problem is to devise a system to process the raw data. Only after this is done should learning algorithms be explored. Once this is done the program can be updated to allow experiments to be changed midway. This will allow experiments to be dynamic which should lead to more efficient experimental methods in obtaining higher quality data. The idea of experiments no longer being a set of procedures pre-determined could enable a new paradigm shift in experimental methods.

It is hoped that with further work the important environmental reactions attempted in this thesis will eventually be successful. Fossil fuels will be needed for the foreseeable future and these reactions could allow them to be used cleanly until alternatives are in place.

8 Reference

1. V. I. Pârvulescu, P. Grange, and B. Delmon, *Catal. Today*, 1998, **46**, 233–316.

2. G. V. G. Baranoski, J. Wan, J. G. Rokne, and I. Bell, *ACM Trans. Graph.*, 2005, **24**, 37–59.

3. T. Sakao, R. Kano, N. Narukage, J. Kotoku, T. Bando, E. E. DeLuca, L. L. Lundquist, S. Tsuneta, L. K. Harra, Y. Katsukawa, M. Kubo, H. Hara, K. Matsuzaki, M. Shimojo, J. A. Bookbinder, L. Golub, K. E. Korreck, Y. Su, K. Shibasaki, T. Shimizu, and I. Nakatani, *Sci.* , 2007, **318** , 1585–1588.

4. A. I. Grigor'ev and S. O. Shiryaeva, *Phys. Scr.*, 1996, **54**, 660.

5. L. B. Loeb and J. M. Meek, *J. Appl. Phys.*, 1940, **11**, 438–447.

6. J. M. Goodings, J. Guo, A. N. Hayhurst, and S. G. Taylor, *Int. J. Mass Spectrom.*, 2001, **206**, 137–151.

7. Y. Shimomura, *J. Nucl. Mater.*, 2007, **363–365**, 467–475.

8. L. S. Polak and Y. A. Lebedev, *Plasma Chemistry*, Cambridge International Science Publishing, 1998.

9. E. M. Liston, L. Martinu, and M. R. Wertheimer, *J. Adhes. Sci. Technol.*, 1993, **7**, 1091–1127.

10. B. M. Smirnov, in *Physics of Ionized Gases*, John Wiley & Sons, 2001, p. 3.

11. B. M. Smirnov, in *Fundamentals of Ionized Gases*, Wiley-VCH, 2012.

12. R. Papoular, in *Electrical Phenomena in Gases*, Elsevier Publishing Company Inc., 1965, pp. 86–91.

13. A. Fridman and L. A. Kennedy, in *Plasma Physics and Engineering*, CRC Press Taylor & Francis Ltd, 2011, pp. 161–243.

14. P. Debye and E. Hückel, *Phys. Zeitschrift*, 1923, **24**, 185–206.

15. F. F. Chen, in *Introduction to Plasma Physics and Controlled Fusion*, Plenum Press, 1984, pp. 1–17.

16. C. F. Gallo, *Ind. Appl. IEEE Trans.*, 1977, **IA-13**, 550–557.

17. R. Papoular, in *Electrical Phenomena in Gases*, Elsevier Publishing Company Inc., 1965, pp. 113–122.

18. S. C. Brown, in *Introduction to Electrical Discharges in Gases*, John Wiley & Sons, Inc, 1965, pp. 94–110.

19. A. von Engel, in *Handbuch der Physik Vol. (21)*, Springer Berlin Heidelberg, 1956, pp. 504–573.

20. L. Bárdos and H. Baránková, *Vacuum*, 2008, **83**, 522–527.

21. S. C. Brown, in *Introduction to Electrical Discharges in Gases*, John Wiley & Sons, Inc, 1965, pp. 189–199.

22. S. C. Brown, in *Introduction to Electrical Discharges in Gases*, John Wiley & Sons, Inc, 1966, pp. 130–149.

23. H. Raether, *Electron avalanches and breakdown in gases*, Butterworths-Heinemnan, 1964.

24. L. B. Loeb, in *Basic Processes of Gaseous Electronics*, University of California Press, 1955.

25. J. M. Meek and J. D. Craggs, *Electrical Breakdown of Gases*, Wiley, New York, 1978.

26. J. M. Meek, *Phys. Rev.*, 1940, **57**, 722–728.

27. A. Fridman, A. Chirokov, and A. Gutsol, *J. Phys. D. Appl. Phys.*, 2005, **38**, R1.

28. J.-S. Chang, P. A. Lawless, and T. Yamamoto, *IEEE Trans. Plasma Sci.*, 1991, **19**, 1152–1166.

29. G. W. Trichel, *Phys. Rev.*, 1938, **54**, 1078–1084.

30. R. Morrow, *Phys. Rev. A*, 1985, **32**, 1799–1809.

31. G. L. Weissler, *Phys. Rev.*, 1943, **63**, 96–107.

32. H. W. Bandel, *Phys. Rev.*, 1951, **84**, 92–99.

33. Y. Akishev, M. Grushin, I. Kochetov, V. Karal'nik, A. Napartovich, and N. Trushkin, *Plasma Sources Sci. Technol.*, 2005, **14**, S18.

34. A. Boulloud and J. Charrier, *J. Phys. D. Appl. Phys.*, 1981, **14**, 207.

35. N. L. Allen, M. Abdel-Salam, M. Boutlendj, I. Cotton, and B. H. Tan, *Sci. Meas. Technol. IET*, 2007, **1**, 103–112.

36. R. Morrow, *J. Phys. D. Appl. Phys.*, 1997, **30**, 3099.

37. H. S. Uhm, *Phys. Plasmas*, 1999, **6**, 4366–4374.

38. D. Bradley and M. L. Gupta, *Combust. Flame*, 1981, **40**, 47–63.

39. H. Ohisa, I. Kimura, and H. Horisawa, *Combust. Flame*, 1999, **116**, 653–661.

40. C. Liu, G. Xu, and T. Wang, *Fuel Process. Technol.*, 1999, **58**, 119–134.

41. M. Morvová, *J. Phys. D. Appl. Phys.*, 1998, **31**, 1865.

42. W. Xu, M.-W. Li, G.-H. Xu, and Y.-L. Tian, *Jpn. J. Appl. Phys.*, 2004, **43**, 8310–8311.

43. J. D. Skalny, J. Orszagh, N. J. Mason, J. A. Rees, Y. Aranda-Gonzalvo, and T. D. Whitmore, *J. Phys. D. Appl. Phys.*, 2008, **41**, 85202.

44. M. Dors and J. Mizeraczyk, *Czechoslov. J. Phys.*, 1996, **46**, 943–952.

45. J. S. Chang, K. Urashima, M. Arquilla, and T. Ito, *Combust. Sci. Technol.*, 1998, **133**, 31–47.

46. K. Hensel, N. Hayashi, C. Yamabe, and M. Morvová, *Jpn. J. Appl. Phys.*, 2002, **41**, 336–345.

47. K. Hensel and M. Morvová, *Contrib. to Plasma Phys.*, 1996, **36**, 51–61.

48. T. Okumura, S. Matsuda, Y. Satoh, Y. Sakai, and H. Tagashira, *J. Phys. D. Appl. Phys.*, 1994, **27**, 801.

49. R. M. Fristrom, in *Flame Structure and Processes*, Oxford University Press Inc, 1995, pp. 247–271.

50. J. Lawton and F. J. Weinberg, in *Electrical Aspects of Combustion*, Clarendon Press: Oxford, 1969, pp. 3–37.

51. J. A. Green and T. M. Sugden, *Symp. Combust.*, 1963, **9**, 607–621.

52. J. J. Thomson and G. P. Thomson, *Conduction of Electricity through gases*, Cambridge University Press, 1928.

53. H. A. Wilson, *Rev. Mod. Phys.*, 1931, **3**, 156–189.

54. H. F. Calcote, *Combust. Flame*, 1957, **1**, 385–403.

55. H. A. Wilson, *The electrical properties of flames and of incandescent solids*, University of London Press, 1912.

56. N. H. Ricker, *Phys. Rev.*, 1916, **8**, 626–632.

57. F. L. Tufts, *Phys. Rev. (Series I)*, 1906, **22**, 193–220.

58. G. J. Mullaney, P. H. Kydd, and N. R. Dibelius, *J. Appl. Phys.*, 1961, **32**, 668–671.

59. H. F. Calcote, *Symp. Combust.*, 1963, **9**, 622–637.

60. D. Bradley and S. M. A. Ibrahim, *J. Phys. D. Appl. Phys.*, 1974, **7**, 1377–1390.

61. D. Bradley and S. M. A. Ibrahim, *J. Phys. D. Appl. Phys.*, 1973, **6**, 465–478.

62. R. M. Clements and P. R. Smy, *J. Phys. D. Appl. Phys.*, 1974, **7**, 551–562.

63. H. F. Calcote and I. R. King, *Symp. Combust.*, 1955, **5**, 423–434.

64. B. E. L. Travers and H. Williams, *Symp. Combust.*, 1965, **10**, 657–672.

65. R. M. Clements and P. R. Smy, *J. Appl. Phys.*, 1969, **40**, 4553–4558.

66. R. M. Clements, A. H. Rizvi, and P. R. Smy, *Plasma Sci. IEEE Trans.*, 1994, **22**, 435–441.

67. C. S. MacLatchy, *Combust. Flame*, 1979, **36**, 171–178.

68. D. K. Bohme, J. M. Goodings, and C.-W. Ng, *Int. J. or Mass Spectrom. Ion Phys.*, 1977, **24**, 335–354.

69. J. Guo, J. M. Goodings, A. N. Hayhurst, and S. G. Taylor, *Combust. Flame*, 2003, **133**, 335–343.

70. S. D. T. Axford, J. M. Goodings, and A. N. Hayhurst, *Combust. Flame*, 1998, **114**, 294–302.

71. J. Lawton and F. J. Weinberg, *Proc. R. Soc. Lond. A. Math. Phys. Sci.*, 1964, **277**, 468–497.

72. S. L. Soo and G. M. Colver, *Symp. Combust.*, 1969, **12**, 3–7.

73. A. von Engel, *Electric Plasmas: Their Nature and uses*, Taylor & Francis Ltd, 1983.

74. D. Bradley, S. M. A. Ibrahim, and C. G. W. Sheppard, *Symp. Combust.*, 1973, **14**, 383–389.

75. J. M. Goodings, J. Guo, and J. G. Laframboise, *Electrochem. commun.*, 2002, **4**, 363–369.

76. E. Hadzifejzovic, J. A. S. Galiani, and D. J. Caruana, *Phys. Chem. Chem. Phys.*, 2006, **8**, 2797–2809.

77. D. J. Caruana and S. P. McCormack, *Electrochem. commun.*, 2001, **3**, 675–681.

78. D. J. Caruana and S. P. McCormack, *Electrochem. commun.*, 2000, **2**, 816–821.

79. D. J. Caruana and S. P. McCormack, *Electrochem. commun.*, 2002, **4**, 780–786.

80. W. T. Brande, *Philos. Trans. R. Soc. London* , 1814, **104** , 51–61.

81. W. Rossichin and W. Timkowski, *Nature*, 1935, **135**, 916.

82. A. Ata, J. S. Cowart, A. Vranos, and B. M. Cetegen, *Combust. Sci. Technol.*, 2005, **177**, 1291–1304.

83. J. Lawton, P. J. Mayo, and F. J. Weinberg, *Proc. R. Soc. Lond. A. Math. Phys. Sci.*, 1968, **303**, 275–298.

84. P. J. Mayo and F. J. Weinberg, *Proc. R. Soc. Lond. A. Math. Phys. Sci.*, 1970, **319**, 351–371.

85. J. J. Thomson, in *Report of the Eightieth Meeting of the British Association for the Advancement of Science.*, 1910, p. 501.

86. H. C. Jaggers and A. von Engel, *Combust. Flame*, 1971, **16**, 275–285.

87. J. C. Polanyi and W. H. Wong, *J. Chem. Phys.*, 1969, **51**, 1439–1450.

88. M. H. Mok and J. C. Polanyi, *J. Chem. Phys.*, 1969, **51**, 1451–1469.

89. A. Y. Starikovskii, *Proc. Combust. Inst.*, 2005, **30**, 2405–2417.

90. N. J. Brown, R. M. Fristrom, and R. F. Sawyer, *Combust. Flame*, 1974, **23**, 269–275.

91. R. M. Fristrom, *Symp. Combust.*, 1963, **9**, 560–575.

92. X. Rao, S. Hammack, T. Lee, C. Carter, and I. B. Matveev, *IEEE Trans. Plasma Sci.*, 2010, **38**, 3265–3271.

93. A. Gutsol, A. Rabinovich, and A. Fridman, *J. Phys. D. Appl. Phys.*, 2011, **44**, 274001.

94. Y. C. Hong and H. S. Uhm, *Phys. Plasmas*, 2006, **13**, 113501.

95. D. C. C. Chen, J. Lawton, and F. J. Weinberg, *Symp. Combust.*, 1965, **10**, 743–754.

96. I. Fells, J. C. Gawen, and J. H. Harker, *Combust. Flame*, 1967, **11**, 309–319.

97. H. A. Wilson and E. Gold, *Proc. Phys. Soc. London*, 1906, **20**, 128–151.

98. A. B. Bryan, *Phys. Rev.*, 1924, **23**, 189–194.

99. C. W. Heaps., *Phys. Rev.*, 1920, **16**, 238–246.

100. Y. Kim, V. W. Ferreri, L. A. Rosocha, G. K. Anderson, S. Abbate, and K.-T. Kim, *IEEE Trans. Plasma Sci.*, 2006, **34**, 2532–2536.

101. W. Kim, M. G. Mungal, and M. A. Cappelli, *Appl. Phys. Lett.*, 2008, **92**, 51503.

102. E. Hadzifejzovic, J. Stankovic, S. Firth, P. F. McMillan, and D. J. Caruana, *Phys. Chem. Chem. Phys.*, 2007, **9**, 5335–5339.

103. R. M. Fristrom, *Flame Structure and Processes*, Oxford University Press Inc, 1995.

104. J. Warnatz, U. Maas, and R. W. Dibble, in *Combustion: Physical and Chemical Fundamentals, Modeling and Simulation, Experiments, Pollutant Formation*, Springer, 2006, p. 99.

105. S. R. Turns, *An Introduction to Combustion Concepts and Applications*, McGrawHill, 2000.

106. I. Glassman and R. A. Yetter, in *Combustion*, eds. I. Glassman and R. A. Yetter, Academic Press, London, 4th edn., 2008, pp. 703–712.

107. I. Glassman and R. A. Yetter, in *Combustion*, eds. I. Glassman and R. A. Yetter, Academic Press, London, 4th edn., 2008, pp. 147–254.

108. J. M. Goodings, D. K. Bohme, and C.-W. Ng, *Combust. Flame*, 1979, **36**, 27–43.

109. ATSC Standard, 2012.

110. A. von Engel and J. R. Cozens, *Proc. Phys. Soc.*, 1963, **82**, 85.

111. J. Lawton and F. J. Weinberg, in *Electrical Aspects of Combustion*, Clarendon Press: Oxford, 1969, pp. 215–241.

112. R. J. Lings, in *EPRI AC Transmission Line Reference Book: 200 KV and Above, Third Edition*, Electric Power Research Institute, 2005, pp. 8–1 – 8–36.

113. A. Fridman, in *Plasma Chemistry*, Cambridge University Press, 2008, pp. 157–258.

114. D. Li, D. Yakushiji, S. Kanazawa, T. Ohkubo, and Y. Nomoto, *J. Electrostat.*, 2002, **55**, 311–319.

115. J. S. Clements, A. Mizuno, W. C. Finney, and R. H. Davis, *Ind. Appl. IEEE Trans.*, 1989, **25**, 62–69.

116. J. Li, W. Sun, B. Pashaie, and S. K. Dhali, *Plasma Sci. IEEE Trans.*, 1995, **23**, 672–678.

117. M. A. Tas, R. van Hardeveld, and E. M. van Veldhuizen, *Plasma Chem. Plasma Process.*, 1997, **17**, 371–391.

118. A. Jaworek, A. Krupa, and T. Czech, *Contrib. to Plasma Phys.*, 1996, **36**, 619–629.

119. K. Yan, S. Kanazawa, T. Ohkubo, and Y. Nomoto, *Plasma Chem. Plasma Process.*, 1999, **19**, 421–443.

120. R. P. Dahiya, S. K. Mishra, and A. Veefkind, *Plasma Sci. IEEE Trans.*, 1993, **21**, 346–348.

121. E. H. W. M. Smulders, B. E. J. M. van Heesch, and S. S. V. B. van Paasen, *Plasma Sci. IEEE Trans.*, 1998, **26**, 1476–1484.

122. A. Fridman, in *Plasma Chemistry*, Cambridge University Press, 2008, pp. 259–354.

123. L. S. Polak and Y. A. Lebedev, in *Plasma Chemistry*, Cambridge International Science Publishing, 1998, pp. 89–160.

124. I. Maezono and J. S. Chang, in *Conference Record of the 1988 IEEE Industry Applications Society Annual Meeting*, IEEE, 1988, vol. 2, pp. 1636–1640.

125. C.-L. Yang and T. Yamamoto, in *Conference Record of 1998 IEEE Industry Applications Conference. Thirty-Third IAS Annual Meeting (Cat. No.98CH36242)*, IEEE, 1998, vol. 3, pp. 1767–1772.

126. S. Masuda and H. Nakao, *Ind. Appl. IEEE Trans.*, 1990, **26**, 374–383.

127. T. Yamamoto, M. Okubo, T. Nagaoka, and K. Hayakawa, *IEEE Trans. Ind. Appl.*, 2002, **38**, 1168–1173.

128. S. Masuda, S. Hosokawa, X. Tu, and Z. Wang, *J. Electrostat.*, 1995, **34**, 415–438.

129. J.-S. Chang, P. C. Looy, K. Nagai, T. Yoshioka, S. Aoki, and A. Maezawa, *Ind. Appl. IEEE Trans.*, 1996, **32**, 131–137.

130. D. Monroe, *Phys. Rev. Focus*, 2007, **19**, 19.

131. G. K. Vemulapalli and S. G. Kukolich, *J. Chem. Educ.*, 1996, **73**, 887.

132. J. Berkowitz, J. P. Greene, H. Cho, and B. Ruscic, *J. Chem. Phys.*, 1987, **86**, 674–676.

133. L. B. Loeb, in *Electrical Coronas Their Basic Physical Mechanisms*, University of California Press, California, 1965, pp. 15–74.

134. A. Fridman, in *Plasma Chemistry*, Cambridge University Press, 2008, pp. 355–416.

135. J. F. Shultz and O. R. Wulf, *J. Am. Chem. Soc.*, 1940, **62**, 2980–2987.

136. G. S. Forbes and L. J. Heidt, *J. Am. Chem. Soc.*, 1934, **56**, 1671–1675.

137. F. Mauss, P. Norbert, B. Rogg, and F. A. Williams, in *Reduced Kinetic Mechanisms for Applications in Combustion Systems*, eds. P. Norbert and B. Rogg, Springer Berlin Heidelberg, New York, 1993, pp. 29–43.

138. P. Norbert, in *Reduced Kinetic Mechanisms for Applications in Combustion Systems*, eds. P. Norbert and B. Rogg, Springer Berlin Heidelberg, New York, 1993, pp. 3–14.

139. S. D. T. Axford and A. N. Hayhurst, *J. Chem. Soc.{,} Faraday Trans.*, 1995, **91**, 827–833.

140. I. Glassman and R. A. Yetter, in *Combustion*, eds. I. Glassman and R. A. Yetter, Academic Press, London, 4th edn., 2008, pp. 1–36.

141. J. Lawton and F. J. Weinberg, in *Electrical Aspects of Combustion*, Clarendon Press: Oxford, 1969, pp. 106–155.

142. S. E. Stein, in *NIST Chemistry WebBook, NIST Standard Reference Database Number 69*.

A. Appendix

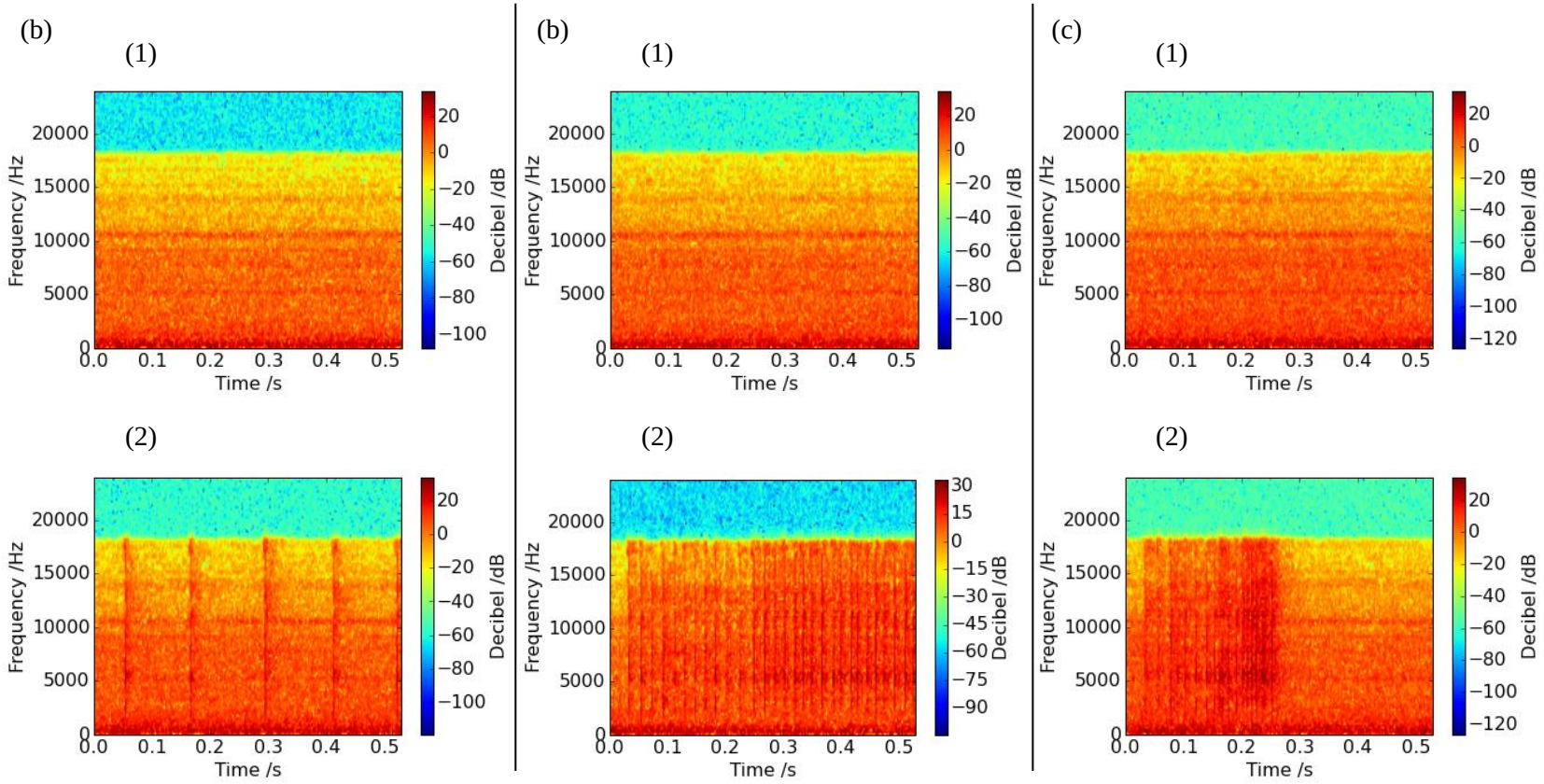

Figure A-1: Spectrographs over a time of 0.5 s showing frequencies from 0 – 24k Hz obtained when a Pt point was placed 0.9 mm from a brass plate electrode. (b), (c) and (d) are points taken from Figure 4-5 where (1) is the background (2) the applied voltage.

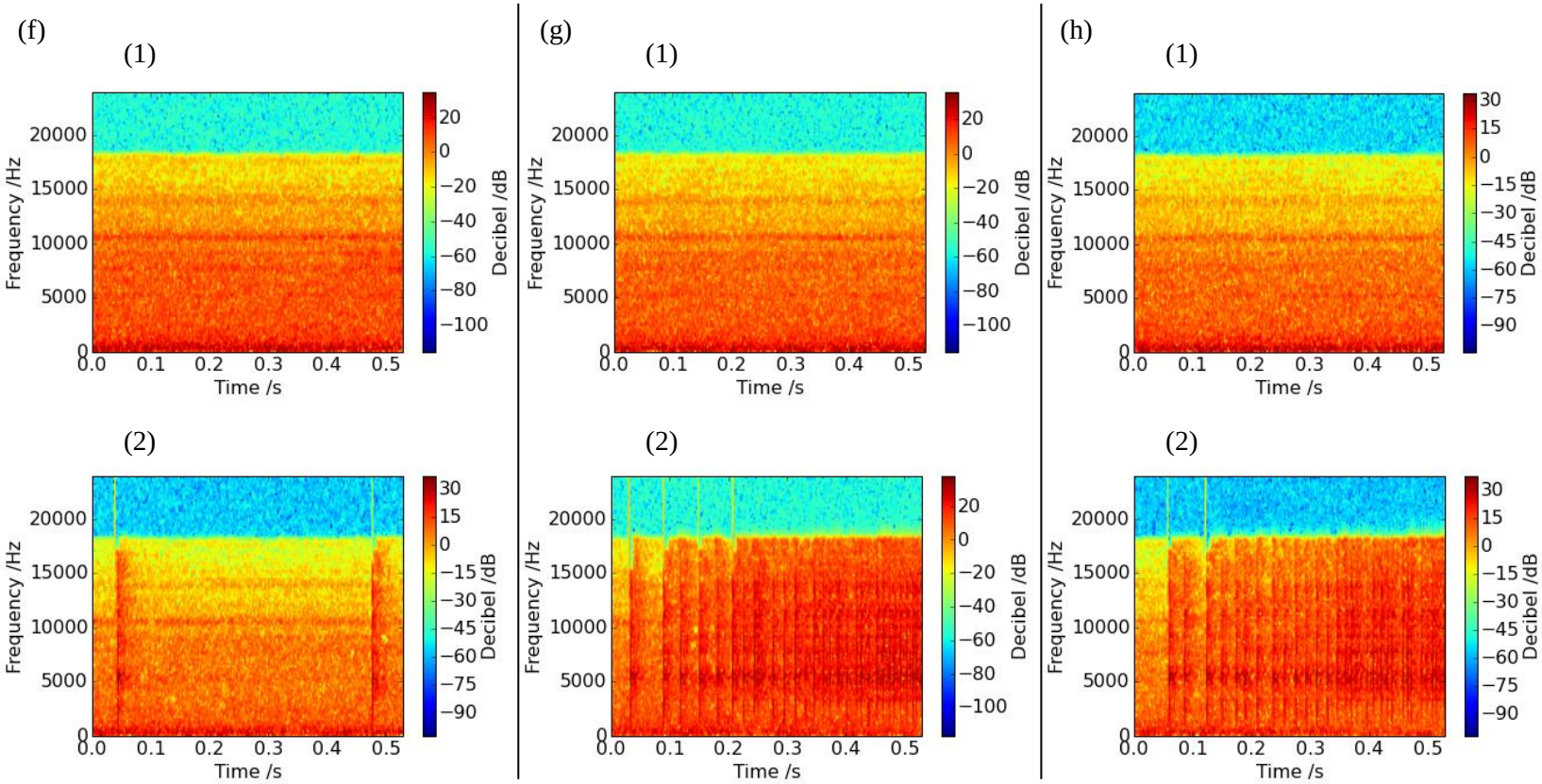

Figure A-2: Spectrographs over a time of 0.5 s showing frequencies from 0 – 24k Hz obtained when a Pt point was placed 1.9 mm from a brass plate electrode. (f), (g) and (h) are points taken from Figure 4-5 where (1) is the background (2) the applied voltage.

Mass in amu	Fragmentation value		Species
	Nist	Hiden	
2		0.7	
16	90	1.1	
17	2122	23	
18	9999	100	H_2O
19	50	0.1	
20	30	0.3	
12	871	6	
13		0.1	
16	961	8.5	
22	190	1.2	
28	981	11.4	
29	10	0.1	
44	9999	100	CO_2
45	120	1.3	
46	40	0.4	
16	2180	11.4	
32	9999	100	O_2
33		0.1	
34		0.4	
14	1379	7.2	
28	9999	100	N_2
29	74	0.8	
1	210	10	
2	9999	100	H_2
20	1462	10.7	
36	30	0.3	
38	5	0.1	
40	9999	100	Ar
14	7.5	751	
15	2.4	240	
16	1.5	150	
30	100	9999	NO
31	0.4	40	
32	0.2	20	

Mass in amu	Fragmentation value		Species
	Nist	Hiden	
13	89		
14	455		
15	1201		
16	85		
25	129		
26	496	5.8	
27	707	8	
28	121		
29	362	4.3	
31	45		
36	70		
37	251	2.1	
38	281	2.3	
39	463	3.8	
40	128		
41	278	2.1	
42	961	7	
43	9999	100	C_3H_6O
44	246		
58		27.1	
2		3	
12	380	2.4	
13	1069	7.7	
14	2042	15.6	
15	8879	85.8	
16	9999	100	CH_4
17	164	1.2	
12	70	2.5	
13	320	5.6	
14	10	0.2	
24	500	5.6	
25	1912	20.1	
26	9999	100	C_2H_2
27	220	2.8	
28	10	0.2	

Mass in amu	Fragmentation value		Species
	Nist	Hiden	
16	520	5.2	
24		0.8	
32	1041	10.4	
33	10		
34	40	0.4	
48	4934	49.3	
49	40	0.4	
50	230	2.3	
64	9999	100	SO_2
65	90		
66	490	4.9	
12	10		
13	20		
14	80		
15	601	5.3	
16	10		
24	10		
25	20		
26	581	6.2	
27	3873	37.1	
28	3213	32.6	
29	4334	44.2	
30	100		
37	70		
38	190		
39	1361	12.5	
40	190		
41	2853	27.8	
42	1211	12.5	
43	9999	100	C_4H_{10}
44	330		
45	10		
49	20		
50	110		
58		12.3	

Mass in amu	Fragmentation value		Species
	Nist	Hiden	
11	20		
12	139		
13	145		
14	664		
16	70		
17	55		
18	279	5.5	
19		2.3	
23	61		
24	246		
25	985		
26	2241	8.3	
27	345	23.9	
28	2985	6.9	
29	812	23.4	
30	9999	6	C_2H_6O
31		100	
32	31		
40	137		
41	474		
42	1144	2.9	
43	71	7.6	
44	5149		
45	2163	34.4	
46		16.5	
12	470	4.5	
14		0.6	
16	170	0.9	CO
28	9999	100	
29	120	1.1	
30		0.2	

Mass in amu	Fragmentation value		Species
	Nist	Hiden	
14	270		
15	951		
19	991	6.6	
26	250		
27	1682	15.7	
28	90		
29	1251	10.1	
31	681	5.6	
37	120		
38	200		
39	661	5.7	
41	821	6.6	
42	440	4	
43	1912	16.6	
44	420		
45	9999	100	C_3H_7OH
46	180		
59	380	3.4	
60	50		

Mass in amu	Fragmentation value from Hiden	Species
39	73	
43	59	
76	83	
78	100	DP oil dc 705
91	32	
16	16	
20	28	
31	9	
47	8	
69	100	DP oil fomblin
97	8	
38	7	
50	100	DP oil ppe
62	27	
63	29	
64	21	
77	89	
39	19	
41	91	
43	100	MP oil
55	64	
57	73	
71	20	
41	32.5	
42	6	
43	73.3	
55	72.7	
56	22.4	
57	100	Rotary oil
58	4.7	
41	76	
42	100	Turbo oil
55	73	
57	88	
69	49	
71	52	

Table A-1: Fragmentations patterns of species observed with parent peak indicated in orange values from Nist[142] values from Hiden.

Species	Relative sensitivity to N_2 from Hiden
H_2O	0.90
CO_2	1.40
N_2	1.00
O_2	0.86
NO	1.20
Ar	1.20
CH_4	1.60
C_3H_6O	3.60
H_2	0.44
C_4H_{10}	4.90
C_2H_2	1.00
C_2H_6O	3.60
C_3H_7OH	1.00
CO	1.05
SO_2	2.10
DP oil dc 705	1.00
DP oil Fomblin	1.00
DP oil ppe	1.00
MP oil	1.00
Rotary pump oil	1.00
Turbo pump oil	1.00

Table A-2: Typical relative sensitivity of observed species with respect to N_2 obtained from Hiden.

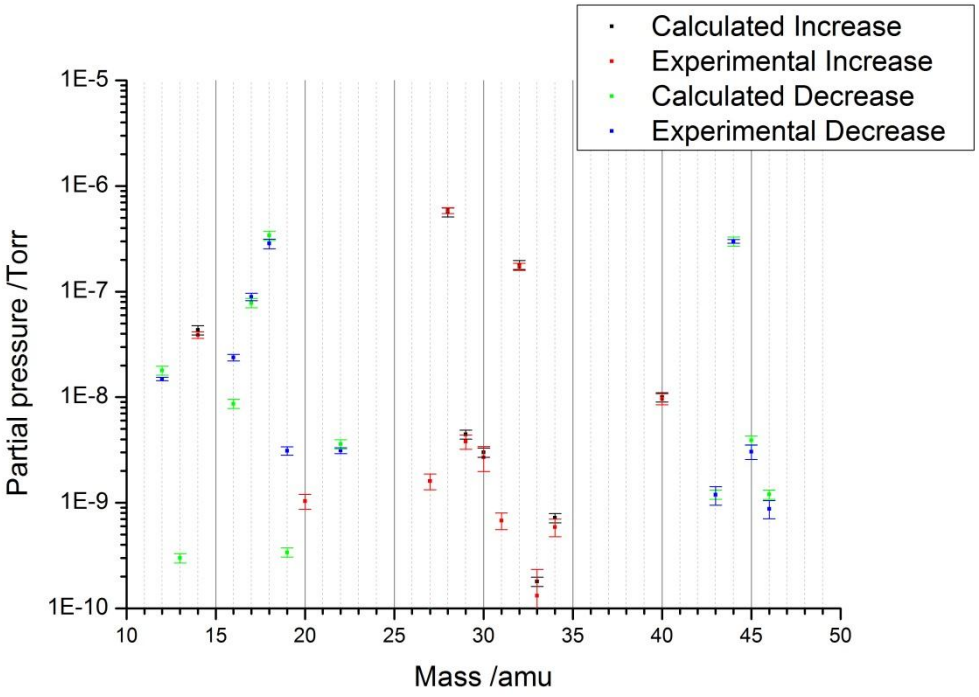

Figure A-3: Graph showing mass spectrums of the absolute changes observed for the increase and decrease of masses 10 – 50 amu when a voltage of 2.0 kV was applied. Calculated values were obtained using the fragmentation patterns in Table A-1 and the relative amounts from Table 5-3. Experimental conditions are from Figure 5-4.

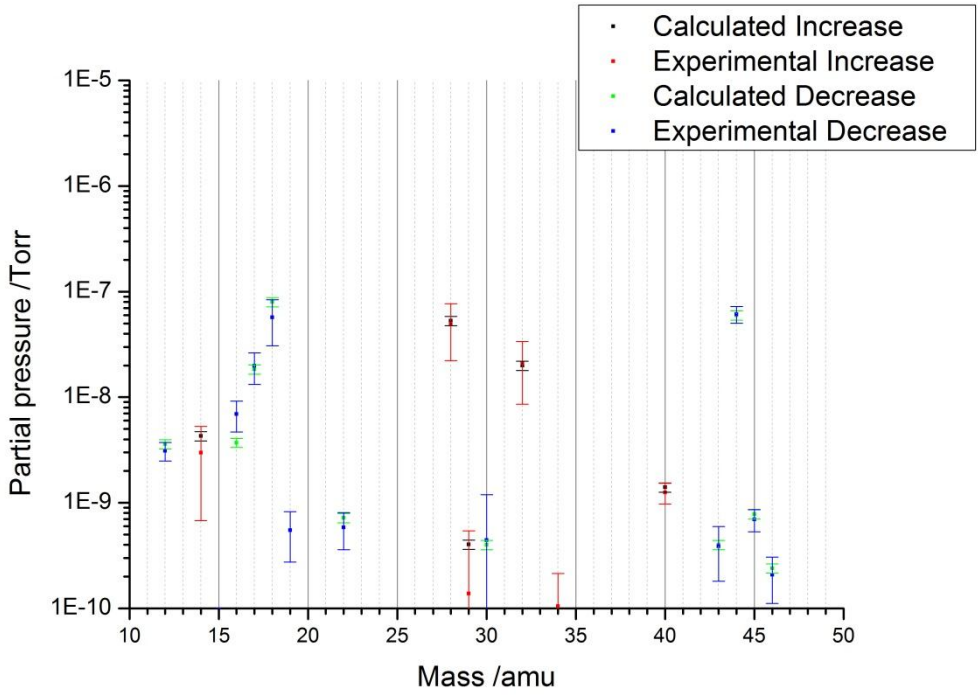

Figure A-4: Graph showing mass spectrums of the absolute changes observed for the increase and decrease of masses 10 – 50 amu when a voltage of 1.5 kV was applied. Calculated values were obtained using the fragmentation patterns in Table A-1 and the relative amounts from Table 5-3. Experimental conditions are from Figure 5-4.

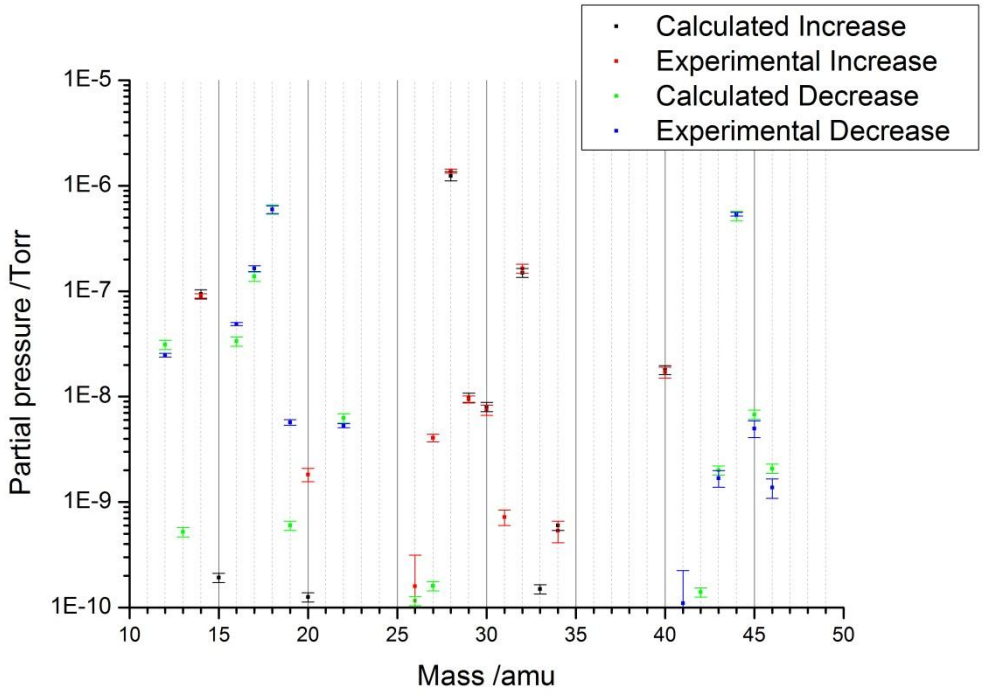

Figure A-5: Graph showing mass spectrums of the absolute changes observed for the increase and decrease of masses 10 – 50 amu when a voltage of 2.5 kV was applied. Calculated values were obtained using the fragmentation patterns in Table A-1 and the relative amounts from Table 5-7. Experimental conditions are from Figure 5-7 but using flow rates of 290/360 ml min^{-1} for N_2 and O_2 respectively.

Gas (20 °C)	Molecular flow	Laminar flow
Air	1.00	1.000
Oxygen	0.95	0.91
Carbon dioxide	0.81	1.26
Water vapour	1.26	1.73

Table A-3: Conversion factors used to calculated conductance of a vacuum system for different gases.

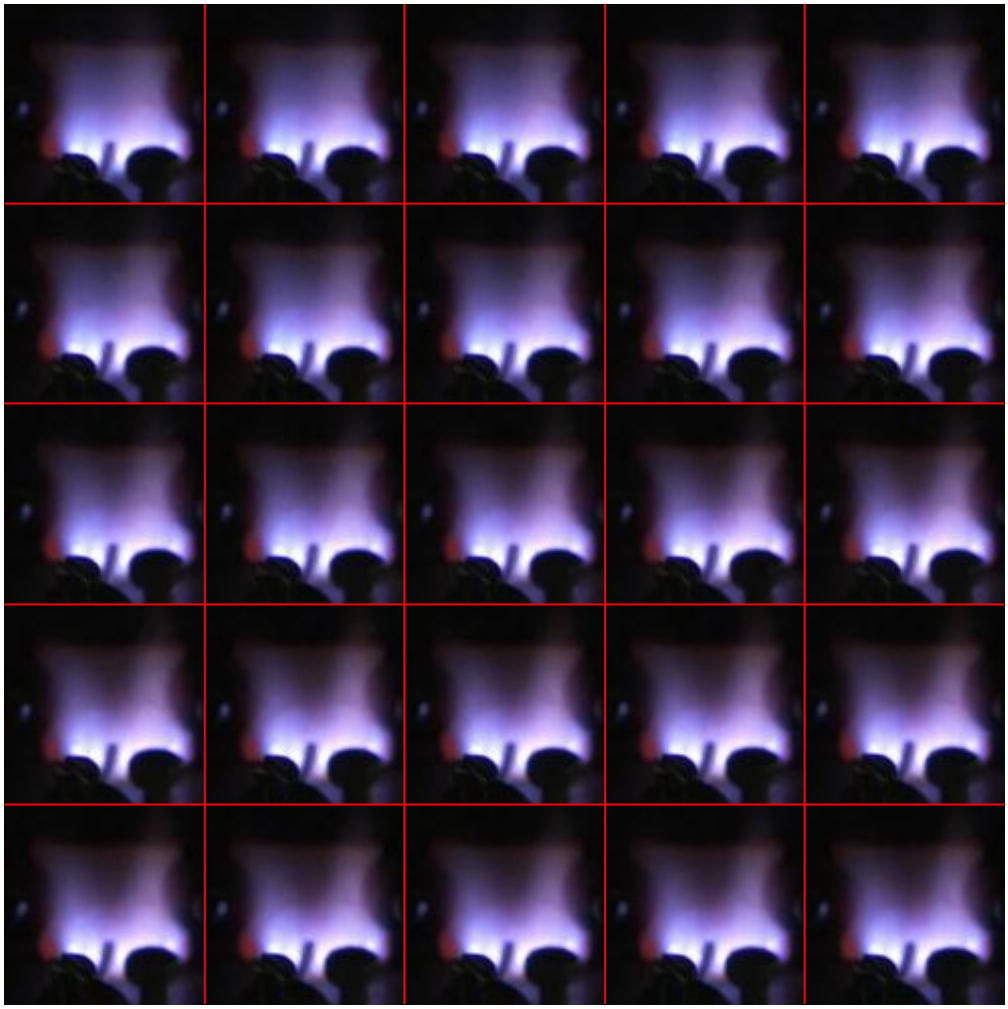

Figure A-6: Video stills taken when a 2 kV electric field was applied to a methane flame. Frames are in order from left to right, top to bottom. Frame 1 starting at the top left and frame 25 at the bottom right. Stills were taken at a sample rate of 50 Hz. The field was created by a Pt point placed 1.9 mm away from a Pt plate material and 2.4 mm above the burner top. Gas ratios for the methane flame were 1.0/2.0/2.3 and 1.0/2.8/1.5 for $CH_4/O_2/N_2$ as described in section 2.